University of Alberta

Magnetic Guiding of Laser Plasmas in Pulsed Laser Deposition

by

Hong Sang

A thesis submitted to the Faculty of Graduate Studies and Research in partial fulfillment of the requirements for the degree of *Master of Science*

Department of Electrical and Computer Engineering

Edmonton, Alberta

Spring 2006

Library and Archives Canada

Published Heritage Branch

395 Wellington Street
Ottawa ON K1A 0N4
Canada

Bibliothèque et Archives Canada

Direction du Patrimoine de l'édition

395, rue Wellington
Ottawa ON K1A 0N4
Canada

Your file Votre référence
ISBN: 0-494-13880-7
Our file Notre référence
ISBN: 0-494-13880-7

NOTICE:
The author has granted a non-exclusive license allowing Library and Archives Canada to reproduce, publish, archive, preserve, conserve, communicate to the public by telecommunication or on the Internet, loan, distribute and sell theses worldwide, for commercial or non-commercial purposes, in microform, paper, electronic and/or any other formats.

The author retains copyright ownership and moral rights in this thesis. Neither the thesis nor substantial extracts from it may be printed or otherwise reproduced without the author's permission.

AVIS:
L'auteur a accordé une licence non exclusive permettant à la Bibliothèque et Archives Canada de reproduire, publier, archiver, sauvegarder, conserver, transmettre au public par télécommunication ou par l'Internet, prêter, distribuer et vendre des thèses partout dans le monde, à des fins commerciales ou autres, sur support microforme, papier, électronique et/ou autres formats.

L'auteur conserve la propriété du droit d'auteur et des droits moraux qui protège cette thèse. Ni la thèse ni des extraits substantiels de celle-ci ne doivent être imprimés ou autrement reproduits sans son autorisation.

In compliance with the Canadian Privacy Act some supporting forms may have been removed from this thesis.

While these forms may be included in the document page count, their removal does not represent any loss of content from the thesis.

Conformément à la loi canadienne sur la protection de la vie privée, quelques formulaires secondaires ont été enlevés de cette thèse.

Bien que ces formulaires aient inclus dans la pagination, il n'y aura aucun contenu manquant.

Canada

University of Alberta

Library Release Form

Name of Author: *Hong Sang*

Title of Thesis: *Magnetic Guiding of Laser Plasmas in Pulsed Laser Deposition*

Degree: *Master of Science*

Year this Degree Granted: *2006*

Permission is hereby granted to the University of Alberta Library to reproduce single copies of this thesis and to lend or sell such copies for private, scholarly or scientific research purposes only.

The author reserves all other publication and other rights in association with the copyright in the thesis, and except as herein before provided, neither the thesis nor any substantial portion thereof may be printed or otherwise reproduced in any material form whatsoever without the author's prior written permission.

_____

Signature

Jan 31 2006

University of Alberta

Faculty of Graduate Studies and Research

The undersigned certify that they have read, and recommend to the Faculty of Graduate Studies and Research for acceptance, a thesis entitled **Magnetic Guiding of Laser Plasmas in Pulsed Laser Deposition** submitted by **Hong Sang** in partial fulfillment of the requirements for the degree of **Master of Science**.

Dr. Ying Y. Tsui

Dr. Robert Rankin

Dr. Robert Fedosejevs

Dr. Ian Mann

Jan 31, 2006

Date

Abstract

Pulsed laser deposition (PLD) is a versatile technique for the deposition of a variety of thin films. A major problem of PLD is the generation of microsized debris particles during laser ablation process and these debris particles contaminate the thin film. In this thesis, a novel technique for debris particle reduction is studied. A 50cm-long straight magnetic field up to 2 kilogauss is used to capture and guide carbon plasmas produced by 248nm (50mJ, 20ns) and 266nm (5mJ, 10ns) laser pulses along the field to the substrate to be coated, while the debris particles are not guided and are allowed to expand freely. In addition, the debris particle velocities are much lower than the ion velocities. In principle, this allows a mechanical shutter to be used to further reduce the number of debris particles reaching the substrate to be coated. By using ion probes and Quartz Crystal Microbalance (QCM), the transport efficiency of the plasma and its dependence on the guiding magnetic field are studied. A Monte-Carlo simulation code based on single-particle theory and a 3D ADI magnetohydrodynamic (MHD) code based on an earlier version are used to simulate the expansion of laser-generated plasma in a magnetic field. Our experiments and simulation results indicate it is feasible to use a straight magnetic field to transport a carbon plasma with efficiencies >40% for the parameters studied in this thesis.

Acknowledgements

I would like to express my gratitude to my supervisors Dr. Ying Y. Tsui, Dr. Robert Rankin, and Dr. Ian Mann. I have benefited significantly from their help and patience during my M.Sc. program. The numerical simulation code used in this work is mainly based on the original magnetosphere simulation code by Dr. Robert Rankin and the revised version by Serguei Roupassov. Without the help from our group technicians Blair Harwood, Rick Conrad and technicians in the machine shop, this work could be not accomplished. I also want to thank my classmates Yang-Wen Sun, Cristina Serbanescu, and Rahim Janmohamed, and Chris Germain for their friendship. Their support and help are essential for me to complete the program. Finally, I sincerely appreciate the support from my parents and girlfriend in China during my study here.

Table of Contents

Abstract i

Acknowledgements ii

Table of Contents iii

Table of Figures v

1 Introduction 1

1.1 Pulsed Laser Deposition 1

1.2 Motivation of magnetic guiding 5

2 Experimental Work 14

2.1 Langmuir Probe and QCM 14

2.1.1 Langmuir Probe Theory 14

2.1.2 QCM Theory 17

2.2 Experimental setup 19

2.3 Magnetic Field, Laser Characteristics and QCM Calibration 24

2.3.1 Magnetic Field Measurements 24

2.3.2 Laser Characteristic Measurement 28

2.3.3 QCM Calibration 31

2.3.4 Synchronization of Laser and Magnetic Field 33

2.4 Transport Efficiency Measurement 35

2.4.1 Langmuir Probe Measurement 35
2.4.2 QCM Measurement Results 52
2.5 Discussion of Experimental Results 54
3 Numerical Simulation 62
3.1 Overview of Plasma Modeling 62
3.2 Single-particle Simulation 64
3.2.1 Single-particle Simulation Algorithm 64
3.2.2 Single-Particle Monte-Carlo Simulation Results and Discussion 74
3.3 Magnetohydrodynamics (MHD) Simulation 76
3.3.1 MHD Theories and ADI Algorithm 76
3.3.2 MHD Simulation Results and Discussions 77
4 Conclusion 84
Appendix I – Solenoid power supply circuit 86
Appendix II – Magnetic field calculation 87
Appendix III – LabVIEW coding diagram for data collecting 97
Appendix IV – Estimation of total charge flux transported in the solenoid 101
Appendix V - The single-particle Monte-Carlo simulation code in MATLAB 103
Reference 110

Table of Figures

Figure 1-1 Typical pulsed laser deposition 5

Figure 1-2 Comparison between conventional (left) and magnetically guided PLD (right) (a) copper deposition, 3000 times debris reduction observed (b) DLC, 20 times debris reduction observed [19] 8

Figure 1-3 Motion of a single charged particle in a uniform magnetic field 10

Figure 1-4 Electrical field E induced by the charge separation due to the curvature drift and the $E \times B$ drift as a result, in a curved magnetic field 10

Figure 1-5 Results of previous single-fluid MHD simulation results for (a) straight-line and (b) curved magnetic field guiding [21] 12

Figure 2-1 Vacuum system 22

Figure 2-2 MGPLD experiment setup 23

Figure 2-3 The Langmuir probe array 23

Figure 2-4 Langmuir probe signal collecting circuit 24

Figure 2-5 Diagram of a solenoid 25

Figure 2-6 Distribution of longitudinal component B_z of magnetic field in the solenoid 26

Figure 2-7 Calculated longitudinal component B_z of magnetic field in the middle of the solenoid at different input voltages 26

Figure 2-8 Hall probe signal with 200V voltage pulses applied to the solenoid at a repetition rate of 10 Hz. Measured at the entrance of the solenoid. 27

Figure 2-9 Magnetic field generated by the solenoid at different input voltages at a repetition rate of 10 Hz. Measured by a Hall probe at the entrance of the solenoid 27

Figure 2-10 Focal spot measurement of 4? Nd:YAG laser at (a) horizontal direction x and (b) vertical direction y. A knife edge mounted on a micron-motion stage is used. 29

Figure 2-11 Focal spot measurement of Lumonics KrF laser at (a) horizontal direction x and (b) vertical direction y. A knife edge mounted on a micron-motion stage is used. 30

Figure 2-12 Stability of QCM frequency reading 31

Figure 2-13 SEM pictures of the calibration sample surface (side view of cleaved edge) 33

Figure 2-14 Time delay between (a) Nd:YAG laser trigger and laser emission detected by a photo diode (b) KrF laser trigger and laser emission (c) solenoid trigger and magnetic field detected by a Hall probe 34

Figure 2-15 Langmuir probe signals of carbon plasma generated by the KrF laser at different bias voltages 37

Figure 2-16 Probe signals of carbon plasma generated by the KrF laser at different bias voltages V when no magnetic field is applied 38

Figure 2-17 Probe signals of carbon plasma generated by the KrF laser at different bias voltages V when a 0.15 T uniform magnetic field is applied 38

Figure 2-18 Signals detected by the central Langmuir probe at the solenoid exit when different magnetic fields are applied, in the case of Nd:YAG (266 nm) laser ablation of a graphite target 41

Figure 2-19 Velocity distribution and Maxwellian fitting when different magnetic fields are applied (solid line: calculated from the central probe signals at the solenoid exit, dash line: Maxwellian fitting), in the case of Nd:YAG (266 nm) laser ablation of a graphite target 42

Figure 2-20 Peak voltage of the fast peak detected by the central probe when different magnetic fields are applied 43

Figure 2-21 Mean velocity of the fast peak detected by the central probe when different magnetic fields are applied 43

Figure 2-22 Charge flux detected by the central probe at the solenoid exit when different magnetic fields are applied, in the case of Nd:YAG laser ablation of a graphite target 44

Figure 2-23 Estimated total charge flux transported in the solenoid and transported fraction at the solenoid exit when different magnetic fields are applied, in the case of Nd:YAG laser ablation of a graphite target. Charge flux collected at the entrance of solenoid (3.5 cm from target) is taken as 100% 44

Figure 2-24 Signals detected by the central Langmuir probe at different distances along the solenoid, in the case of Nd:YAG laser ablation of a graphite target, with a magnetic field B=0.25T 45

Figure 2-25 Charge flux detected by the central probe at different distances in the case of Nd:YAG (266 nm) laser ablation of a graphite target, with a magnetic field B=0.25T. Charge flux collected at the entrance of solenoid (3.5 cm from target) is taken as 100% 46

Figure 2-26 Estimated total charge flux transported in the solenoid and transported fraction at different distances in the case of Nd:YAG (266 nm) laser ablation of a graphite target, with a magnetic field B=0.25T..... 46

Figure 2-27 Signals detected by the central Langmuir probe when different magnetic fields are applied, in the case of KrF (248 nm) laser ablation of a graphite target 48

Figure 2-28 Velocity distribution and Maxwellian fitting when different magnetic fields are applied (solid line: calculated from probe signals, dash line: Maxwellian fitting), in the case of KrF (248 nm) laser ablation of a graphite target..... 49

Figure 2-29 Charge flux detected by the central probe at the solenoid exit when different magnetic fields are applied, in the case of KrF (248 nm) laser ablation of a graphite target..... 50

Figure 2-30 Estimated total charge flux transported in the solenoid and transported fraction at the exit of solenoid when different magnetic fields are applied, in the case of KrF (248 nm) laser ablation of a graphite target..... 50

Figure 2-31 Charge flux by the central probe at different distances in the case of KrF (248 nm) laser ablation of a graphite target, with a magnetic field B=0.25T. Charge flux collected at the solenoid entrance (3.5 cm from target) is taken as 100% 51

Figure 2-32 Estimated total charge flux transported in the solenoid and transported fraction at different distances in the case of KrF (248 nm) laser ablation of a graphite target, with a magnetic field B=0.25T. Charge flux detected at the solenoid entrance (3.5 cm from target) is taken as 100%..... 51

Figure 2-33 Deposition rate measured by QCM at the exit of solenoid when different magnetic fields are applied, in the case of KrF (248 nm, 10 Hz) laser ablation of carbon..... 53

Figure 2-34 Comparison of measured total charge flux and the theoretical results using the ~$B^{4/3}$ law, in the case of KrF (248 nm) laser ablation of carbon..... 56

Figure 2-35 Comparison of measured total charge flux and the theoretical results using the ~$B^{4/3}$ law, in the case of Nd:YAG (266 nm) laser ablation of carbon... 56

Figure 2-36 Comparison of DLC deposition rate by KrF laser, measured by QCM and calculated results from Langmuir probe signals, assuming ions are singly charged 61

Figure 3-1 Geometry of the laser-produced plasma in the single-particle simulation..... 67

Figure 3-2 Monte-Carlo algorithm used to generated a $\cos^n(?)$ density distribution..... 68

Figure 3-3 Angular distributions of 20,000 ions generated by a Monte-Carlo code 68

Figure 3-4 Maxwellian distribution of longitudinal velocity of 20,000 ions generated by a Monte-Carlo code. With a peak at 4×10^6 cm/s and a width of 2×10^6 cm/s 69

Figure 3-5 Simulated trajectories of 20 random individual C^+ ions satisfying $cos^4(?)$ distribution at different B values 70

Figure 3-6 Distribution of transported C^+ ions at the exit of solenoid at different B values. 1,000 initial C^+ ions satisfying (a) an initial $\cos^4(?)$ and (b) $\cos^8(?)$ distribution are used. 71

Figure 3-7 Transported fraction of plasma containing 20,000 C^+ ions at the exit of the solenoid (55 cm away from target) with different initial density distributions 72

Figure 3-8 Captured fraction of 20,000 initial C^+ ions at the entrance of solenoid (3.5 cm away from target) with different initial density distributions 72

Figure 3-9 Captured fraction of 20,000 initial C^+ ions at the entrance of solenoid (3.5 cm away from target) with different initial density distributions, when a non-uniform B distribution is considered at the solenoid entrance 73

Figure 3-10 Transported fraction of plasma containing 20,000 C^+ ions at the exit of the solenoid (55 cm away from target) with different initial mean velocities, $\cos^4(?)$ initial density distributions are used 73

Figure 3-11 Simulated density (normalized) profile of laser plasma with magnetic field B=0, with a diffusion coefficient $D = 10^{-3}\ cm^2 \cdot s^{-1}$ 81

Figure 3-12 Simulated density (normalized) profile of laser plasma with magnetic field B=0, with a diffusion coefficient $D = 10^{-4}\ cm^2 \cdot s^{-1}$ 83

1 Introduction

1.1 Pulsed Laser Deposition

Since the first laser was constructed in 1960, laser techniques have been playing important roles in modern science. The increasing knowledge of laser-matter interaction has brought lasers into a variety of applications in material science, the electronics industry, metallurgy, sensor technology, laser surgery etc. In 1965, the first Pulsed Laser Deposition (PLD) was demonstrated by Smith and Turner. However, the potential of PLD had not been recognized until the success of high-temperature superconductor film deposition by Dijkkamp and Venkatesan et al. in 1987 [1].

Traditional thin film deposition techniques are mainly Chemical Vapor Deposition (CVD) and Physical Vapor Deposition (PVD). The difference between the terms "chemical" and "physical" is determined by the binding energy level involved in the deposition process. The energy sources involved in evaporation or sputtering of target materials in CVD or PVD are usually heat, electron beams and ion beams. To facilitate the formation of thin film on the substrate surface, usually the substrate is heated to a high temperature.

Compared to the plumes generated in traditional PVD or CVD techniques, laser-generated plasma in PLD is usually more energetic when a high enough laser intensity is used. The kinetic motion of the fast-expanding plume is highly directional, and a considerable fraction of the ablated material is actually ionized. Therefore, the growth of crystalline film is possible at a relatively low substrate temperature (<100 °C) in PLD. The deposition could be preformed either in vacuum or with ambient gas. Moreover, the

energy source of PLD, i.e. the laser system, is located outside of the deposition chamber, so the operation is more convenient. It could also be cost-efficient, because a single laser source could serve several systems in the same lab. These advantages of PLD are important since a relatively simple and cost-efficient setup is usually desired in industrial applications. On the other hand, in PLD the stoichiometric transfer of material from target to substrate allows the deposition of many kinds of materials, including metal, semiconductor, oxide, nitride, polymer etc. The "pulsed" nature of this technique also gives precise thickness control and makes the deposition of multi-layer or complex compounds possible. Currently, PLD is practically the only technique suitable for depositing thin films of high-temperature superconductor and some other heat-sensitive materials. However, the theoretical and practical optimization of PLD processes is still a research topic.

Diamond-like carbon (DLC) deposition by the PLD technique has attracted a lot of attention in recent years. Due to the high mechanical strength, low friction, chemical inertness and optical transparency, DLC films have found a variety of applications such as protective coatings and anti-reflective coatings for IR windows. In most cases, the structure of deposited carbon films is a combination of C-C, sp^2, and sp^3 bonds. The sp^3 bonds are believed to be responsible for the desirable properties of DLC films mentioned earlier. The ratio of sp^3/sp^2 bonds is determined by deposition conditions. Studies have shown the energetic carbon ion flux in laser-generated plasma can facilitate the deposition of carbon films with high sp^3/sp^2 ratios [2]-[6], which makes PLD a better technique to deposit DLC films compared to other PVD and CVD techniques.

The PLD technique is conceptionally simple. The basic process is shown in Figure 1-1. A laser beam with a high intensity is focused on the target surface to generate the plasma plume, which expands and then is deposited on the substrate usually a few cm away from the target. The deposition system is placed in a vacuum chamber with or without ambient gas. Usually a rotating target is used to avoid the formation of deep craters on the target surface. Reactive ambient gas could be added to the chamber during the deposition. For example, O_2 can be used as the ambient gas during ZnO deposition to compensate the O element lost during the deposition process [7].

Properties of the laser beam are essential factors in laser-material interactions. The energy and intensity will directly determine how much material is ablated and the dynamics of the plasma plume. The absorption of target material depends on the laser wavelength used. Energies of the order of tens of mJ per pulse are usually used. The intensity used in PLD may range from 10^8 to 10^{10} W/cm^2 for ns laser pulses, while the distance from ablation target to substrate varies from several cm to tens of cm. UV lasers such as 3? , 4? Nd:YAG lasers (with wavelengths of 355nm and 266nm respectively) and excimer lasers such as XeCl, KrF, and ArF (with wavelengths 308nm, 248nm and 193nm respectively) are widely used because of the high absorptance of many materials at UV wavelengths.

It is generally recognized that the plasma ejected by pulsed laser ablation will not propagate isotropically but with a forward angular distribution satisfying $cos^n(?)$, where ? is the polar angle with respect to normal [34][57][58]. The parameter n (usually n = 4~8) is determined mainly by spot size and fluence of the laser beam. A more forward peaked plume as the spot size increases is predicted by the adiabatic model [57][66]. For carbon

plasmas generated in a DLC deposition, previous studies [48][49] found the major ion components in the plasma produced by a 20 ns KrF laser are C^+ and C^{2+}, which are concentrated within ±20 degrees to the normal direction. The velocity distributions of different ion species are determined by the laser-plasma interaction and expansion process. However, some literature [59] suggested different *?* distributions or even velocities for different ion or ion cluster species. In some cases [52]- [56], it may not even be centered at *?*=0. This is believed to be related to interactions between the early-generated plume and the incident beam, when the pulse duration of the ablation beam is long enough.

As for the velocity distribution of laser-produced plasmas, the widely accepted model is that the plasma plume satisfies a "shifted" Maxwell distribution, which is the combination of the standard Maxwell distribution and a drift velocity [41][64]. Assuming a point source (ablation beam spot size is much smaller than the target to substrate distance) and the normal of the target surface is along the *z*-axis, the distribution could be represented by

$$f(v_x, v_y, v_z) = \left(\frac{m}{2\pi kT}\right)^{3/2} \exp\{-(m/2k_BT)[v_x^2 + v_y^2 + (v_z - u)^2]\} \qquad (1\text{-}1)$$

where v_x, v_y, v_z are the velocity components in three directions and u is the drift velocity.

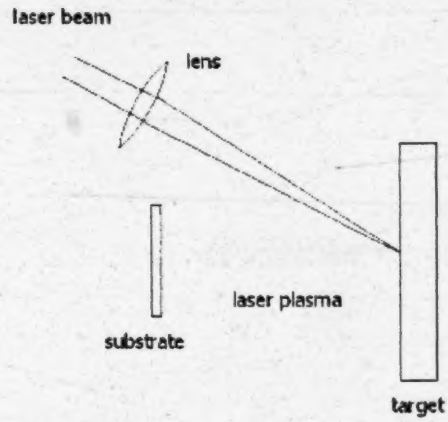

Figure 1-1 Typical pulsed laser deposition

1.2 Motivation of magnetic guiding

Although the PLD technique has many advantages, it also has some disadvantages, including deposition of debris particles and limited film uniformity. The presence of debris particles may degrade the deposited films in high-performance applications. The original state of debris particles could be vapor, liquid or solid. The sources of them can often be distinguished from their sizes and shapes. Debris particles formed from vapor typically have sizes of the order of nanometers, while those from liquid or solid states are typically micrometer or sub-micrometer in size. Debris particles in the solid state are usually irregular in shape, while those from droplets are usually spherical. Several mechanisms, which lead to the formation of debris particles, have been proposed [34]-[36]. These mechanisms include: (i) explosive ejection of target material due to sub-surface superheating; (ii) ejection of droplets or particulates due to recoil pressure induced by laser ablation; (iii) re-condensation of ablated material in the gas phase; and

(iv) hydrodynamics instabilities. The irregular-shaped particulates are believed to come from the protruding surface of the target. The ejection of droplets is usually caused by recoil pressure of a thermal shock and superheating of subsurface layers, while the nanometer-sized particulates are mainly the results of condensation due to super-saturation.

By tuning the deposition parameters, such as laser fluence, wavelength, target-substrate distance, ambient gas and avoiding a rough target surface etc., the generation of debris particles and their propagation can be somewhat reduced. However, changing these parameters may also compromise the deposition rate and thin film properties. Without changing the ablation laser beam and the target, a few techniques have been developed to reduce debris particles efficiently, such as mechanical filtering, dual-beam ablation, use of off-axis geometries and magnetic deflection.

Based on the fact that ions in the plasma have a velocity a order of magnitude higher than that of debris particles, a mechanical velocity filter has been shown to prevent slower particles from reaching the deposition substrate [61]. The dual-beam ablation technique is also reported as a very effective way to reduce debris density on the deposited film. A complete elimination of particulates by using 2-beam ablation is claimed by Gyö rgy et al. [35]. In their work, an ArF laser beam (193 nm) is used as the main beam to ablate the target, while a second IR beam (1064 nm) parallel to the target surface from a Nd:YAG laser is used to vaporize the remaining debris particles in the laser-generated plasma plume.

Magnetic confinement has been widely used in controlled fusion schemes for decades. However, interest in magnetic confinement and guiding in thin film deposition

started only recently. As one of the major thin film deposition techniques, vacuum arc deposition uses arc discharge as the plasma source instead of laser ablation. In arc deposition, the ejection of micrometer-sized debris particles is also a major drawback, which can degrade the film quality. As an improvement of conventional arc deposition techniques, a curved cylindrical magnetic duct was reported to be used as a debris filter to reduce droplets and particulates in vacuum arc deposition [8]-[13]. Similar to that, the application of magnetic deflection in pulsed laser deposition has also been proposed recently [14]-[18].

Our group has been working on Magnetically Guided Pulsed Laser Deposition (MGPLD). In our previous MGPLD experiments [19][20], a 1 kG magnetic field generated by a 50 cm-long (5 cm diameter) curved solenoid with 75 cm radius of curvature was used to guide plasma plumes produced by 248 nm KrF laser ablation. As shown Figure 1-2, effective reduction of debris density was observed for both copper and diamond-like carbon (DLC) deposition. Experiments also showed that this debris reduction technique is more effective for copper than for carbon. This difference is believed to be caused by the different natures of materials. It is believed that copper debris are mostly in liquid form and therefore will easily adhere to the solenoid wall, so those debris droplets that hit the wall cannot reach the substrate to be coated, while carbon debris particles are probably in solid form and therefore can bounce around the inside of the solenoid, so some of them can still reach the substrate to be coated even after hitting the wall.

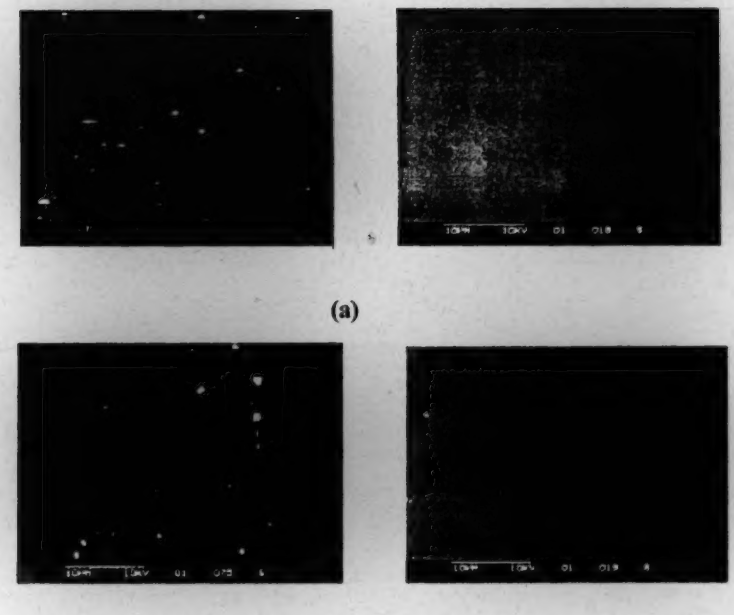

Figure 1-2 Comparison between conventional (left) and magnetically guided PLD (right) (a) copper deposition, 3000 times debris reduction observed (b) DLC, 20 times debris reduction observed [19]

Although the debris reduction efficiency is high when the curved magnetic field is used, the transport efficiency in the curved geometry is only around 10% at a guiding field of around 0.2 T. It was also observed that the plasma plume is offset towards the outer wall of the curved solenoid at the exit end. A higher guiding magnetic field is expected to improve transport efficiency by reducing the plasma offset. Some theoretical explanations have been proposed for the offset of plasma in the curved magnetic field [19]- [22]. As explained later, curvature drift and $E \times B$ drift are believed to play major roles in producing the offset. For a straight geometry, the transport efficiency can be much higher because there will be no plasma offset due to drifts.

To understand the mechanisms behind the MGPLD technique, some related plasma theories will be reviewed. The main theories used to describe the behaviors of plasma include single particle theory, magnetohydrodynamics (MHD) and kinetic theory.

Single particle theory is the simplest one of all these theories. In short, the plasma is treated as a simple combination of individual particles. Therefore the overall behaviors of plasma can be predicted by studying individual particles. In the presence of a uniform magnetic field, a charged particle will gyrate around the field line and move along the magnetic field, as shown in Figure 1-3. The particle velocity can be decomposed into a parallel component $v_{//}$ and a transverse component $v_{\perp}$ with respect to the magnetic field B. Then the radius of gyration (Lamor radius) is

$$r_R = \frac{mv_{\perp}}{qB} \tag{1-2}$$

For example, for a typical laser-produced carbon plasma, the Lamor radius of a singly charged carbon ion with $v_{\perp} = 10^6$ cm/s (corresponding to 6.25 eV) is 1.25 cm in a 1 kG uniform magnetic field. Assuming electrons have the same temperature as ions, the Lamor radius of an electron will be only 0.08 mm.

At the same time, the charged particles will move along the magnetic field at the velocity $v_{//}$. According to this theory, as long as a single particle entering into the solenoid has a small enough $v_{\perp}$ to make r_R smaller than the solenoid radius, it should be able to go through the solenoid (assuming the particle will be lost if it hits the solenoid wall). Magnetic field is also widely used to confine plasmas in many other applications, such as controlled fusion and magnetic mirrors, etc.

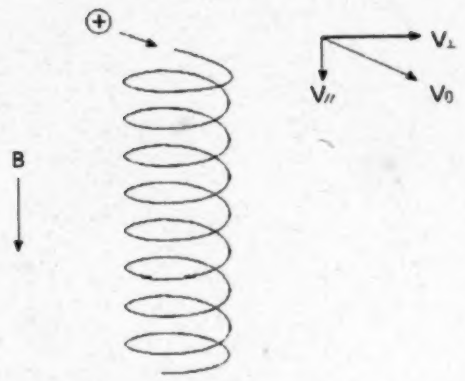

Figure 1-3 Motion of a single charged particle in a uniform magnetic field

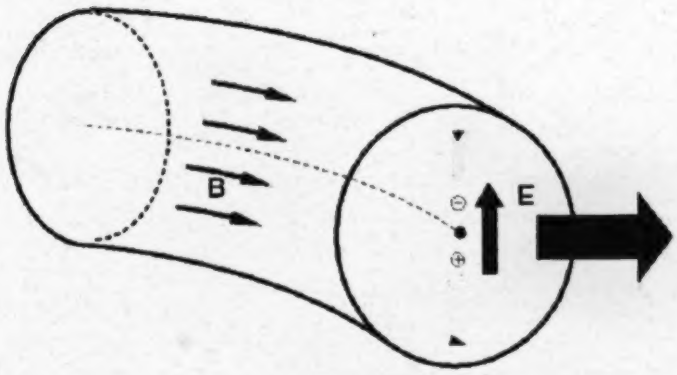

Figure 1-4 Electrical field *E* induced by the charge separation due to the curvature drift and the *E*×*B* drift as a result, in a curved magnetic field

In a curved magnetic field configuration, it is believed that the loss of plasma is related to drift phenomena. When there is a gradient or curvature in a magnetic field, a drift of the gyration center will occur due to the different values of r_R at different locations [30]. For a curved magnetic field with radius R_c, the curvature drift velocity v_R is given by

$$v_R = \frac{m v_{//}^2}{qB^2} \frac{\bar{R}_C \times \bar{B}}{R_C^2} \tag{1-3}$$

Because the drift direction of ions and electrons are opposite, the induced electric field E due to charge separation will induce further $E \times B$ drift of the guiding center. The $E \times B$ drift velocity is given by

$$v_E = \frac{\bar{E} \times \bar{B}}{B^2} \tag{1-4}$$

The directions of the curvature drift and the $E \times B$ drift are demonstrated in Figure 1-4.

The single particle theory is not sufficient for the study of a plasma with higher density since it does not take the interactions between particles into account. However, it gives us a good indication of the likely loss mechanisms for plasmas in a curved magnetic field. As a more accurate macroscopic theory, magnetohydrodynamics treats the plasma as a fluid. When a Maxwell-Boltzmann distribution is assumed, the behavior of plasma can be described by a fluid with a single flow velocity. A set of single-fluid MHD equations can be derived from equations of motion of electrons and ions and Maxwell's equations.

A previous MHD simulation by S. Roupassov [21] showed the difference in plasma transport efficiency due to the difference in drift behaviors in the straight geometry and

the curved geometry. As shown in Figure 1-5, the overall drift effect could result in loss of plasma due to the plasma drifting to the solenoid wall in a curved magnetic field.

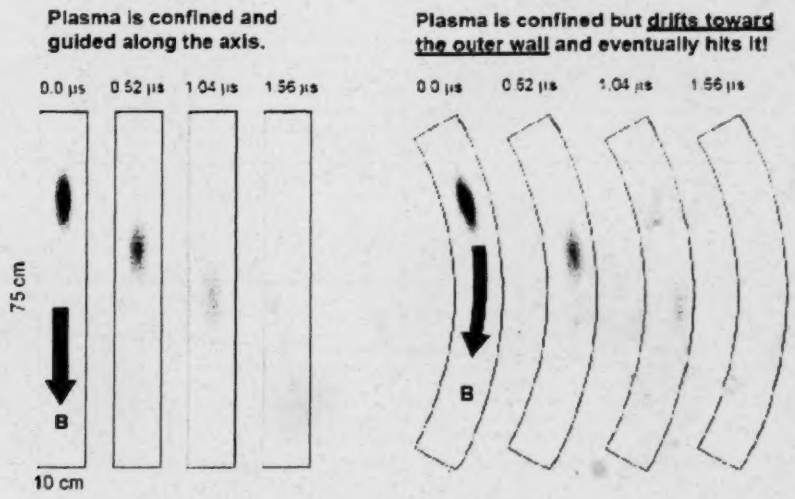

(a) (b)

Figure 1-5 Results of previous single-fluid MHD simulation results for (a) straight-line and (b) curved magnetic field guiding [21]

Although the debris reduction efficiency is high when a curved magnetic field is used, the transport efficiency of plasma is low (around 10% in the above case). A higher guiding magnetic field is expected to improve transport efficiency by reducing the plasma drift. Since the loss of plasma is related to curvature drift, it is expected that the transport efficiency for a MGPLD using a straight field geometry would be enhanced. Since the velocity distributions of debris particles generated in laser ablation are directly related their sizes and maximum debris velocity was reported to be smaller than the plasma plume velocity by at least an order of magnitude [61]. A mechanical debris filter system

with reasonable debris reduction efficiency based on rotating vanes could be designed. In this thesis the capturing and guiding of a carbon laser plasma in a straight magnetic field are studied.

A simple scaling law for laser plasma confinement is provided by some previous studies, which reported that a magnetic field could be used to slow down a laser-produced plasma. The work by Harilal et al. [43][47] shows how a laser-produced aluminum plume can be slowed down significantly by a 0.64 T transverse magnetic field. The theoretical calculation by Bhadra [42] indicates the plume will be stopped within a distance of $R \sim B^{2/3}$. Also, the extent of the diamagnetic effect could be indicated by the β parameter, which is the ratio of the thermal pressure $P_t = nk_B T$ to the magnetic pressure $P_B = B^2/8p$. When $\beta << 1$ (for example, for a low density plasma), the shielding effect of plasma in the magnetic field could be ignored in most cases.

2 Experimental Work

As discussed earlier, charged particles in a laser-produced plasma will gyrate around and move along the magnetic field line. The transverse expansion of plasmas will be suppressed by the magnetic field due to Lamor gyration. In this manner, a magnetic field could be used to confine and guide a laser-produced plasma. The main experimental tools in this work are Langmuir probes and Quartz Crystal Microbalance (QCM). A Langmuir probe array is used to measure the charge flux in a laser-produced carbon plasma, which includes ions, electrons and charged clusters, but not the neutrals. Meanwhile QCM is used as a complementary tool to study the overall mass flux, including both charged particles and neutrals. For pulsed laser deposition (PLD) applications, the main factor to evaluate the usefulness of our magnetic guiding technique is the efficiency, i.e. how much plasma could be transported to the substrate to be coated. Therefore, the focus of experiments and discussions in this section is mainly on the guiding efficiency of laser-produced plasmas when straight-line magnetic fields with different strengths are used to guide the plasma.

2.1 Langmuir Probe and QCM

2.1.1 Langmuir Probe Theory

Commonly used plasma diagnostic techniques include ion probes (Langmuir probe and Faraday probe), time-of-flight mass spectroscopy (TOFMS), and optical spectroscopy. TOFMS and spectral measurements are very useful when the details of

plasma composition are required, because these techniques can distinguish different particle species in the plasma flux. However, TOFMS requires an acceleration mechanism like an electric field to separate different species, which makes the setup more complicated. The advantage of ion probes is that they are relatively simple, robust, inexpensive, and tolerant to background pressure, and they can be put directly into the plasma flow. Ion probe techniques are widely used for the characterization of laser plasmas. One disadvantage is that they do not distinguish different ion species and cannot measure neutral particles as the other techniques may do.

As one of the oldest plasma diagnostic techniques, Langmuir probes can be very simple. Usually a Langmuir probe is a cylindrical conductor biased to a positive potential to measure electrons or negative potential to measure ions. The density and temperature of the plasma can be determined from the currents measured at various biasing voltages. However, secondary emission from the detector surface due to ion bombardment may cause inaccuracy. For the laser-produced plasmas studied in this work, the ion kinetic energies are much less than keV and secondary electron emissions are expected to be small, so Langmuir probes should be adequate to give relatively accurate measurements.

The Langmuir probe theory for laser plasmas was discussed by Koopman [27] and Felts [28]. When a negative bias voltage is applied on the Langmuir probe, electrons in the plasma will be repelled. Similarly, when a positive bias voltage is applied, ions will be repelled. By varying the bias voltage, charged particles with certain energies can be rejected from the probe. When the negative voltage is large enough, a saturation region is reached, which means almost all electrons are repelled from the probe surface. For the

laser plasmas studied here, a bias of –40 V is observed to be enough to repel most of the electrons.

For a plasma containing only singly-ionized ions, the current I collected by a transverse cylindrical Langmuir probe in a flowing plasma (the normal of the flat surface of the probe is in the direction of plasma flow) with velocity U is given by [27][29][30]:

$$I = AneU[1 + 2e(V - V_0)/MU^2]^{1/2} \qquad (2\text{-}1)$$

where A is the active area projected normal to the plasma flow, V is the bias potential applied on the probe and V_0 is the plasma potential. The above formula is a reasonable approximation in the case of relatively "cold" plasma, where the kinetic energy is much higher than the thermal energy. As a reasonable simplification, for fast moving plasma typically

$$MU^2 >> 2e(V - V_0) \qquad (2\text{-}2)$$

. For a plasma containing different ion species, the Langmuir probe signal should be

$$I = Ae(\sum n_i Z_i)U \qquad (2\text{-}3)$$

According to the above equation, the current collected by the probe can be calculated if the drift velocity U and the density of ion species n_i in the plasma are known. However, the sheath effect should be also considered. When the Langmuir probe bias is sufficiently negative compared to the plasma potential, the electron current is negligible since most of electrons are repelled except for the high-energy tail in the Maxwellian distribution. The Bohm sheath criterion indicates the velocity of ions that can enter the sheath should satisfy

$$U_0 > (KT_e/M)^{1/2} \qquad (2\text{-}4)$$

If the position where $U_0 = (KT_e / M)^{1/2}$ is set as the boundary of the sheath, the potential at the sheath edge will be

$$\Phi_s = -\frac{1}{2} KT_e / e \tag{2-5}$$

where Φ_s is the potential relative to the plasma. Therefore the electron density n_s at the edge of sheath will be

$$n_s = n_0 e^{e\Phi_s / KT_e} = n_0 e^{-1/2} = 0.61 n_0 \tag{2-6}$$

Assuming charge neutrality, the saturation ion current should be

$$I \approx \frac{1}{2} n_0 eA (KT_e / M)^{1/2} \tag{2-7}$$

Here the factor 0.61 is replaced by 1/2 as a simplification, which is usually acceptable.

2.1.2 QCM Theory

Quartz Crystal Microbalance (QCM) can be used as a thickness monitor in thin film depositions. The measurement of deposited mass is based on the change in the resonant frequency of a quartz crystal. The shift in resonant frequency $(f_q - f_c)$ due to a small mass uniformly deposited over a crystal surface is linearly proportional to the deposited mass. Here f_q and f_c are the frequencies of the quartz crystal before and after the extra mass is deposited. If ρ_q, t_q and ρ_f, t_f are the density and thickness of the quartz crystal and deposited film respectively, the frequency shift is given by

$$\frac{f_q - f_c}{f_q} = \frac{\rho_f t_f}{\rho_q t_q} \tag{2-8}$$

Although the above equation gives a linear dependence of the frequency shift on the deposited mass, this simple theory is based on the assumption that there is no stored

energy in the deposited mass, i.e. the frequency shift is not affected by other physical properties of the film. According to a more accurate approach treating the quartz-film combination as a composite acoustic resonator [37], the resonance frequency f_q of the lowest mode shear wave in a quartz crystal plate of thickness t_q should be given by

$$2t_q = v_q / f_q \tag{2-9}$$

where v_q is the shear wave velocity of quartz crystal. Usually the quartz crystal used in QCM is AT-cut to minimize the influence of temperature and v_q =3.34×10^5 cm/s. The relation between film thickness and resonance frequency could be found by solving the wave equation

$$\frac{\partial^2 u_j}{\partial x^2} = \frac{\rho_j}{\mu_j}\frac{\partial^2 u_j}{\partial t^2} \tag{2-10}$$

Using proper boundary conditions at the boundary between the quartz and the thin film, the solution for a quartz crystal of thickness t_q with a thin film of thickness t_f is [37]

$$\rho_f t_f = \rho_q t_q \left(\frac{1}{2\pi Z f_c}\right)\tan^{-1}\left\{Z\tan\left[\pi\frac{(f_q - f_c)}{f_q}\right]\right\} \tag{2-11}$$

$$Z = \frac{Z_q}{Z_f} = \frac{\sqrt{\rho_q \mu_q}}{\sqrt{\rho_f \mu_f}} = \frac{\rho_q v_q}{\rho_f v_f} \tag{2-12}$$

where Z_q and Z_f are the acoustic impedance of quartz and thin film respectively. Define the mass ratio and frequency change ratio as

$$M = \frac{\rho_f t_f}{\rho_q t_q} \tag{2-13}$$

with

$$F = \frac{f_q - f_c}{f_q} \tag{2-14}$$

then the solution becomes

$$M = \frac{\tan^{-1}(Z \tan \pi F)}{\pi Z(1-F)} \tag{2-15}$$

Therefore, the thickness of deposited thin film t_f can be calculated from the measured reduced frequency shift F.

2.2 Experimental setup

All of the experiments in this thesis were performed in vacuum. As shown in Figure 2-1, a mechanical pump is used for pumping the chamber to an initial vacuum of around 100 mTorr. It is also used as the backing pump for a diffusion pump. The diffusion pump can pump down the aluminum chamber to a pressure as low as 10^{-6} Torr. To reduce oil vapor entering the chamber, a liquid nitrogen cold trap is used. The pressure in the chamber is monitored by an Edwards S-NW25 active magnetron gauge. The typical pressure in the chamber during experiments is in the range of $1\sim5\times10^{-5}$ Torr.

To reduce the number of debris particles that can reach the substrate, a long target-substrate distance is desired. However, the length of the guiding magnetic field shouldn't be too long to sacrifice the amount of plasma transported through the solenoid. Based on these two considerations, a 50 cm long straight solenoid is used in our experiments. Its diameter is 5.0 cm, respectively. An AC power supply provides voltage pulses up to 10 Hz to the solenoid. Related measurement results will be given later in this chapter.

One application of our MGPLD technique is the deposition of diamond-like-carbon (DLC) thin films. Therefore, a 99.99% purity machine-polished graphite plate is used as the ablation target in our DLC deposition experiments. However, the surface of the graphite is relatively rough even after it is polished mechanically. Rough surfaces are believed to enhance debris particles emission during the deposition process [34][35]. It also makes it impossible to directly observe the ablation craters with a microscope. A 2-dimensional motion stage is used to move the target in both x and y directions.

Ultraviolet (UV) laser beams are used here, because the absorption of most materials is higher in UV wavelengths. A Lumonics TE-860 excimer laser using KrF working gas (248 nm) and a 4? Ultra UL421111 Nd:YAG laser (266 nm) are used to generate ns laser pulses to ablate the target. Other than the difference in wavelengths, these two lasers also have a significant difference in energy per pulse and focused spot size. Therefore, the plasmas generated by them are quite different, so different guiding behaviors might be observed. A fused silica positive lens with a diameter D =2 inch and a focal length f = 20cm is used to focus the laser beam. The lens to target distance could be adjusted manually to get the best focus during experiments. The optimum distance from the lens to the target was obtained from the Langmuir probe, assuming the largest signal corresponds to the smallest focal spot. Laser energy per pulse was measured by a calorimeter and monitored by a photo diode. The photo diode signal is also used as the trigger signal for the oscilloscopes. Focal spot sizes are measured by the knife-edge technique to be discussed later in this chapter.

Langmuir probes are used to detect the laser-produced plasma. The probes are made of copper cylinders with a diameter of 6 mm and a length of 12 mm. The probe array has

5 identical probes arranged in a manner as shown in Figure 2-3. The probe array is attached to a plastic rod, which could be used to move the probe array in to different locations in the solenoid without breaking the vacuum. A bias box was connected to the Langmuir probes and its circuit diagram is shown in Figure 2-4. The bias voltage used ranges from −50 to 50 V. And 50 Ω terminators are attached to the input BNCs of the oscilloscopes. All the 5 probes in the array were tested to have the same sensitivity under same condition.

Tektronics TDS-210 or TDS-220 oscilloscopes are used to measure the probe signals. The oscilloscopes are connected to the RS232 ports of a computer. A LabVIEW program is written to transfer data from the oscilloscope into ASCII files in a computer for later data analysis (see Appendix III).

Because the signal detected by probes at a large distance is very small when the magnetic field is turned off, another Langmuir probe at a much closer distance to the target is added outside the solenoid, as shown in Figure 2-2.

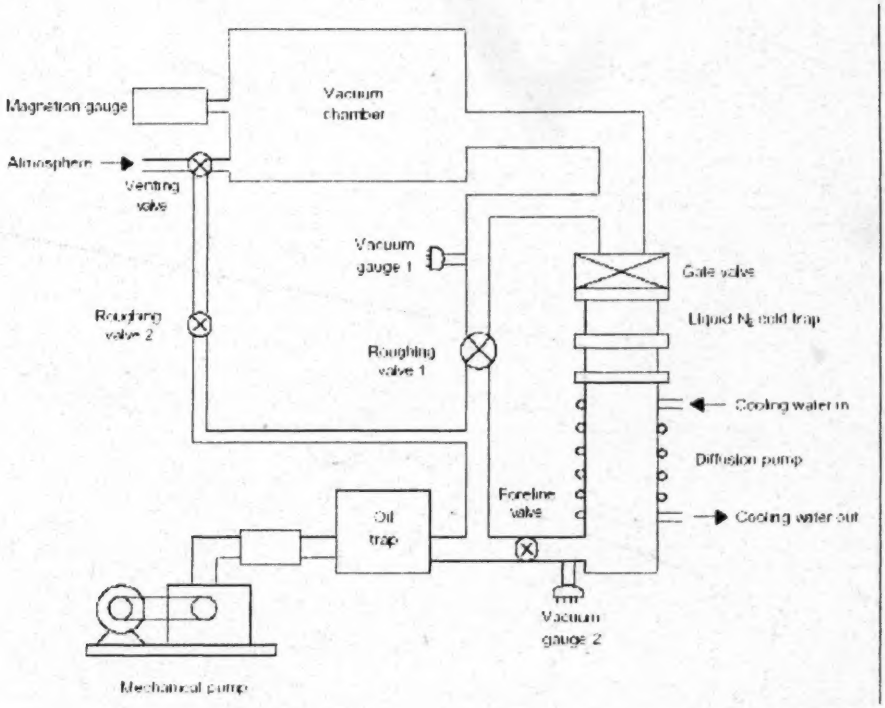

Figure 2-1 Vacuum system

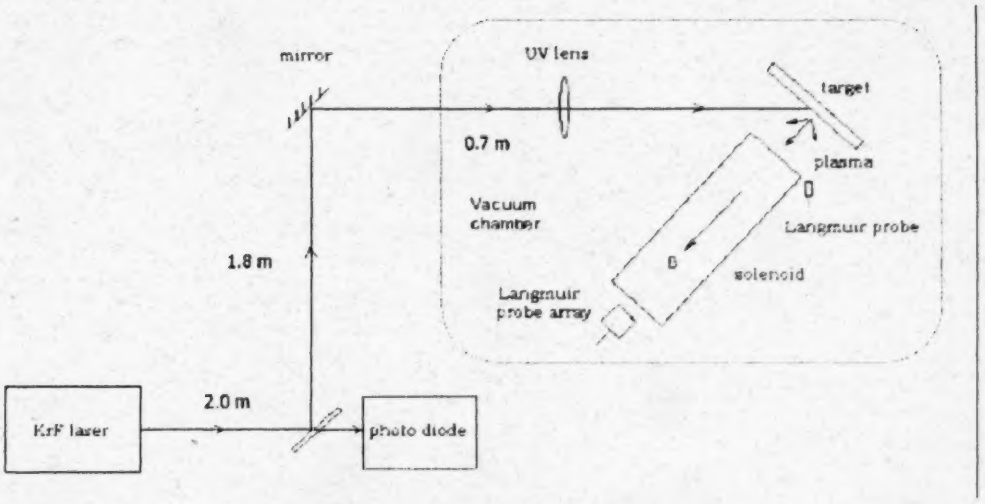

Figure 2-2 MGPLD experiment setup

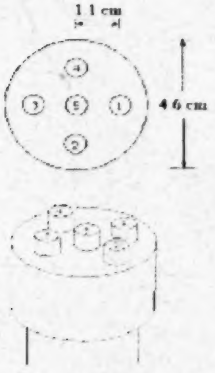

Figure 2-3 The Langmuir probe array

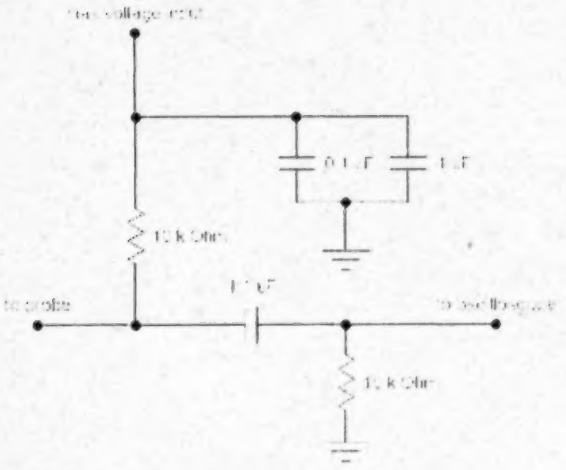

Figure 2-4 Langmuir probe signal collecting circuit

2.3 Magnetic Field, Laser Characteristics and QCM Calibration

2.3.1 Magnetic Field Measurements

According to the Biot-Savart Law, the magnetic field induced by a current element is given by

$$d\bar{B} = \frac{\mu_0 I d\bar{L} \times \bar{r}}{4\pi r^3} \tag{2-16}$$

where $d\bar{L}$ is the length of wire carrying current I and $\bar{r}$ is the unit vector indicating the direction and distance from the current element to the field point. Therefore, the field due to a current loop can be calculated by the integrating $d\bar{B}$ around the whole loop

$$\bar{B} = \frac{\mu_0 I}{4\pi} \oint \frac{d\bar{L} \times \bar{r}}{r^3} \tag{2-17}$$

A MATLAB program based on the above equations is used to calculate the magnetic field distribution in the solenoid. The source code is listed in Appendix II. The solenoid used in our experiments is 50 cm long and its diameter is 5.0 cm. If the geometry of a solenoid is as shown in Figure 2-5, the calculated distribution of longitudinal component of magnetic field B_z along the plasma propagation direction is shown in Figure 2-6. The distribution is relatively uniform inside the solenoid. Figure 2-7 shows the calculated dependence of the generated magnetic field B on the solenoid input voltage.

The pulsed power supply circuit for the solenoid is shown in Appendix I. Voltage pulses up to 10Hz are used to drive the solenoid. Magnitude of the generated magnetic field is measured using a Hall probe. The Hall probe has a sensitivity of 1.22 KGauss/V (0.122 T/V). An example of measured Hall probe signal is shown in Figure 2-8. As expected, the measured magnetic field increases almost linearly as the voltage of the power supply is increased (see Figure 2-9).

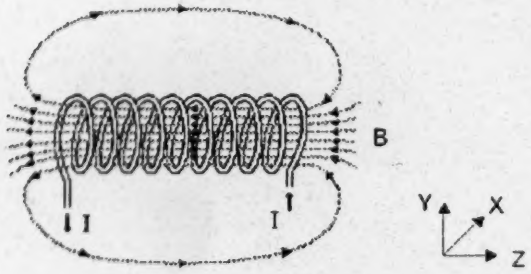

Figure 2-5 Diagram of a solenoid

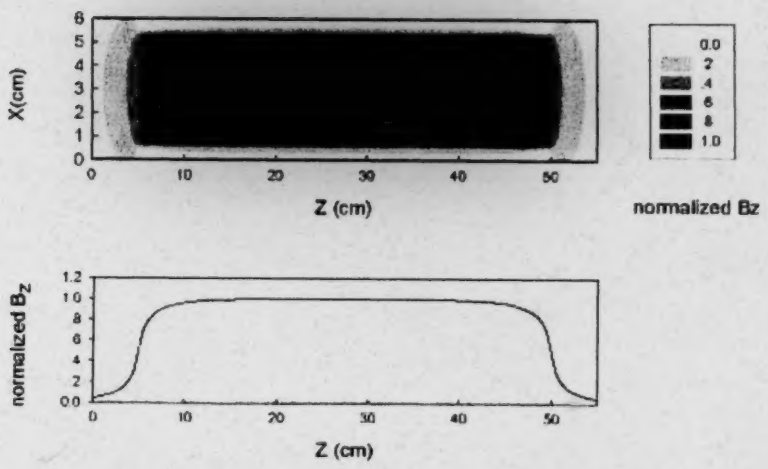

Figure 2-6 Distribution of longitudinal component B_z of magnetic field in the solenoid

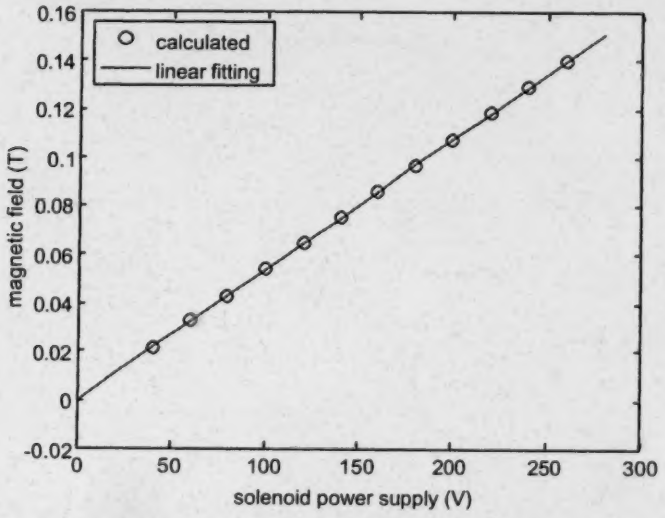

Figure 2-7 Calculated longitudinal component B_z of magnetic field in the middle of the solenoid at different input voltages

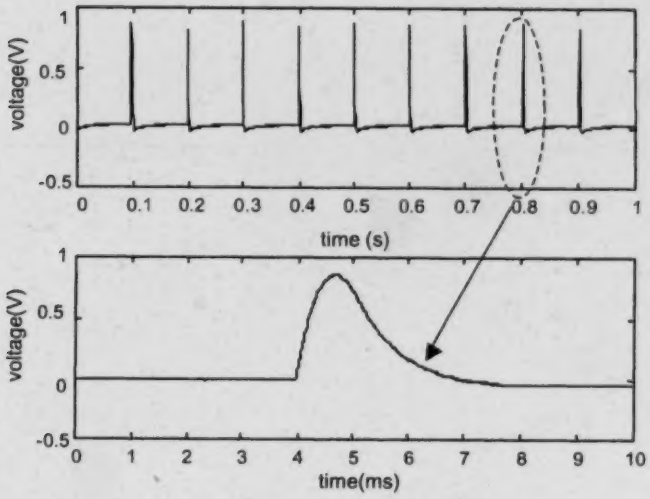

Figure 2-8 Hall probe signal with 200V voltage pulses applied to the solenoid at a repetition rate of 10 Hz. Measured at the entrance of the solenoid.

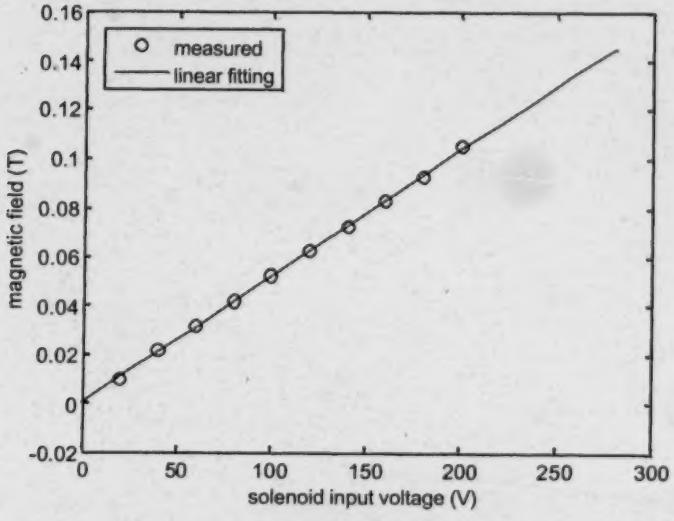

Figure 2-9 Magnetic field generated by the solenoid at different input voltages at a repetition rate of 10 Hz. Measured by a Hall probe at the entrance of the solenoid

2.3.2 Laser Characteristic Measurement

Calibrated calorimeters are used to measure the laser pulse energy at the beginning of every experiment or after every laser refill of the KrF laser. During the experiment, a photo diode is setup to monitor the pulse energy variation (see Figure 2-2).

To estimate the intensities of the focused laser beams, the focal spot is measured by using the knife-edge technique. A knife-edge with a roughness of around 5μm is mounted on a 2-axis Oriel Linear Stage, which can move the knife-edge with a precision of 1 μm in both horizontal and vertical directions. In this measurement, the beam energy is attenuated to a proper level before being focused by the same f = 20cm lens used in the PLD experiments. The transmission of the laser energy past the knife-edge is measured by a photo diode (with a diffuser) behind the knife-edge. Measurement results for the 4? Nd:YAG 266nm laser and the Lumonics KrF 248nm laser are shown in Figure 2-10 and Figure 2-11 respectively. The intensity profile is calculated from the slope of the measured photo diode signals versus knife-edge positions. The shapes of beams generated by the 4ω Nd:YAG laser and the KrF laser are observed to be elliptical and rectangular respectively. The FWHMs (Full Width Half Maximum) are estimated to be 0.5mm and 0.75mm in horizontal and vertical direction respectively for the focused Nd:YAG laser spot, and 2mm and 1.5mm respectively for the focused KrF laser spot. The effective focal spot areas are estimated to be 1.15 mm^2 for the elliptical 4? Nd:YAG spot and 3.0 mm^2 respectively for the rectangular KrF spot. Thus the intensities are estimated to be 0.45×10^8 W?cm^{-2} and 0.83×10^8 W?cm^{-2} for the 4ω Nd:YAG laser (5 mJ, 10 ns per pulse) and the KrF laser (50 mJ, 20 ns per pulse) respectively.

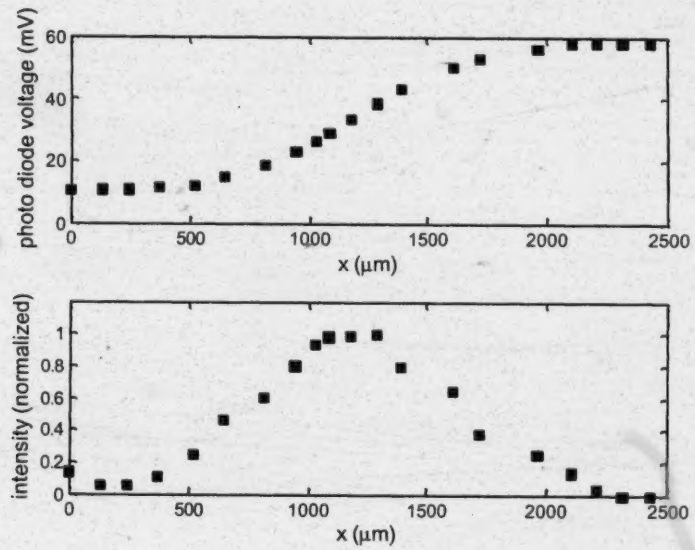

(a)

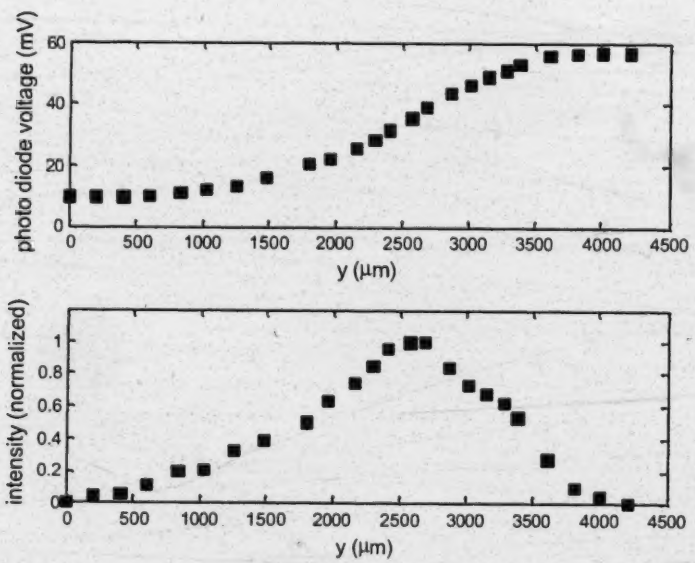

(b)

Figure 2-10 Focal spot measurement of 4? Nd:YAG laser at (a) horizontal direction x and (b) vertical direction y. A knife edge mounted on a micron-motion stage is used.

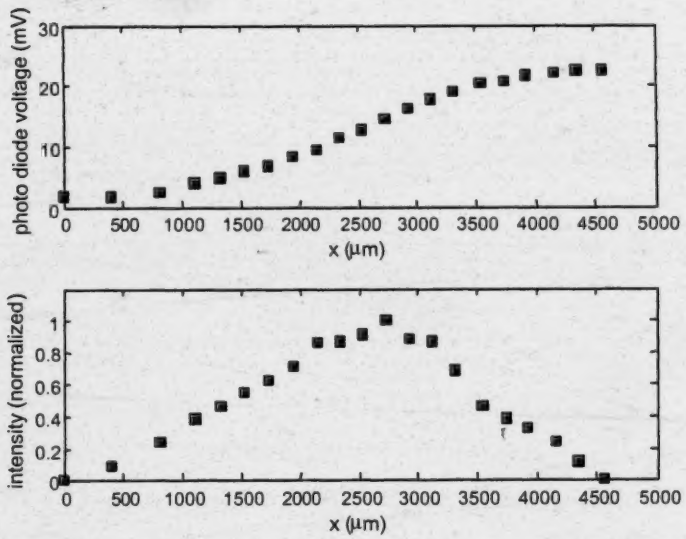

(a)

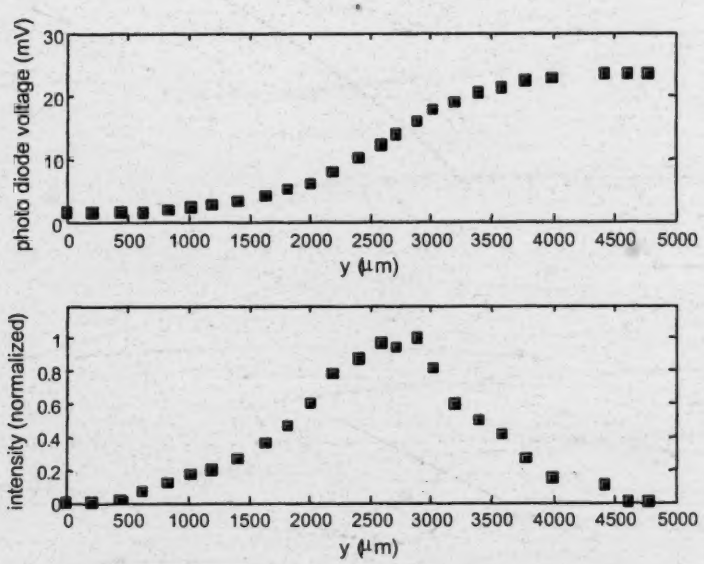

(b)

Figure 2-11 Focal spot measurement of Lumonics KrF laser at (a) horizontal direction x and (b) vertical direction y. A knife edge mounted on a micron-motion stage is used.

2.3.3 QCM Calibration

A MAXTEK TM-400 quartz crystal monitor (QCM) is used to measure the thickness of deposited films. In our experiment, 6 MHz crystals made by Phelps Electronics Inc. are used. The crystals are coated with gold electrodes. The QCM detector head is water cooled to minimize the influence of thermal instability. The QCM detector was placed in the vacuum chamber during "pumping down" to test the stability of frequency reading. The variation of frequency reading within 80 minutes is shown in Figure 2-12. During this period, the pressure in the chamber drops from 1000 mTorr to around 1 mTorr. The variation of QCM frequency is due to the pressure change and stabilization of QCM detector circuit. During the pump down period, a gradual increase in QCM frequency is observed. This is probably due to the detachment of moisture and other molecules originally attached to the detector crystal surface when the chamber pressure is going down.

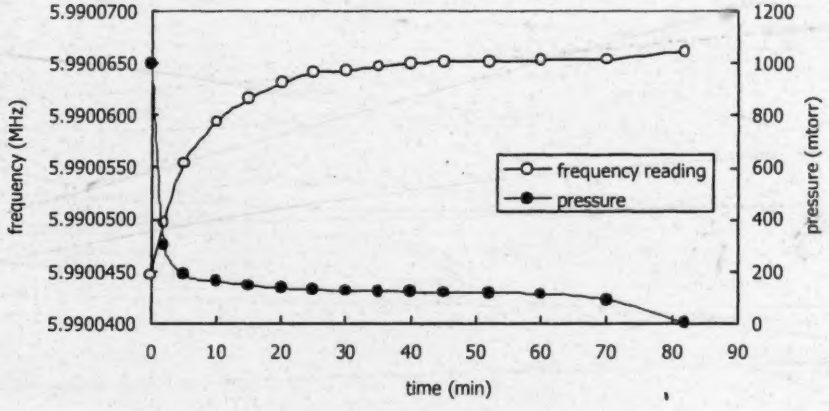

Figure 2-12 Stability of QCM frequency reading

As described previously, material density and acoustic impedance are required to convert the resonance frequency reading to the real thickness. In the case of diamond-like carbon thin film, these two parameters are determined by the composition of the film. The deposited film is a combination of graphite-like structure and diamond-like structure. The densities of graphite and diamond are 2.25 $g?cm^{-3}$ and 3.52 $g?cm^{-3}$, respectively, and the acoustic impedances are 2.71 $g?cm^{-2}?s^{-1}$ and 40.14 $g?cm^{-2}?s^{-1}$, respectively, for graphite and diamond. Since the exact ratio of graphite to diamond was unknown without other further measurements, it is impossible to get the thickness reading from the QCM by feeding in precise parameters directly. Therefore, a calibration measurement is required to give the thickness reading.

The QCM detector crystal and a few silicon wafers are placed at a distance of 3.5 cm from the carbon target. The calibration deposition is conducted at approximately 50 mJ per pulse at 10 Hz for 40 minutes by using the KrF 248 nm laser. The thickness of deposited DLC film is obtained from scanning electron microscope (SEM) pictures. By using the parameters of diamond, a film thickness reading of 100 nm on the calibration sample was obtained. As shown in Figure 2-13, the side view of the cleaved calibration sample indicates an actual film thickness of around 214 nm. Therefore, a calibration factor of 2.14 was subsequently used in the MGPLD experiments.

Figure 2-13 SEM pictures of the calibration sample surface (side view of cleaved edge)

2.3.4 Synchronization of Laser and Magnetic Field

A 4? Nd:YAG laser at 266 nm and a KrF laser at 248 nm are used to study the transport efficiency of laser-generated carbon plasma in the magnetic field. In order to synchronize the magnetic field pulses and the laser plasma pulses, the delay time between solenoid power trigger and magnetic field and the delay time between laser trigger and laser output need to be measured for both lasers. The magnetic field pulse was measured by using a Hall effect probe and the laser pulse was measured by using a silicon photodiode. The measured results are shown in Figure 2-14. The 4? Nd:YAG laser triggering delay, the Lumonics KrF laser trigger delay, and solenoid trigger delay are observed to be 0.2 ms, 12ms and 0.7 ms respectively. Therefore, a delay unit is required to generate the solenoid trigger 0.5 ms ahead of the laser trigger in the Nd:YAG case and 11.3 ms behind the laser trigger in the KrF case.

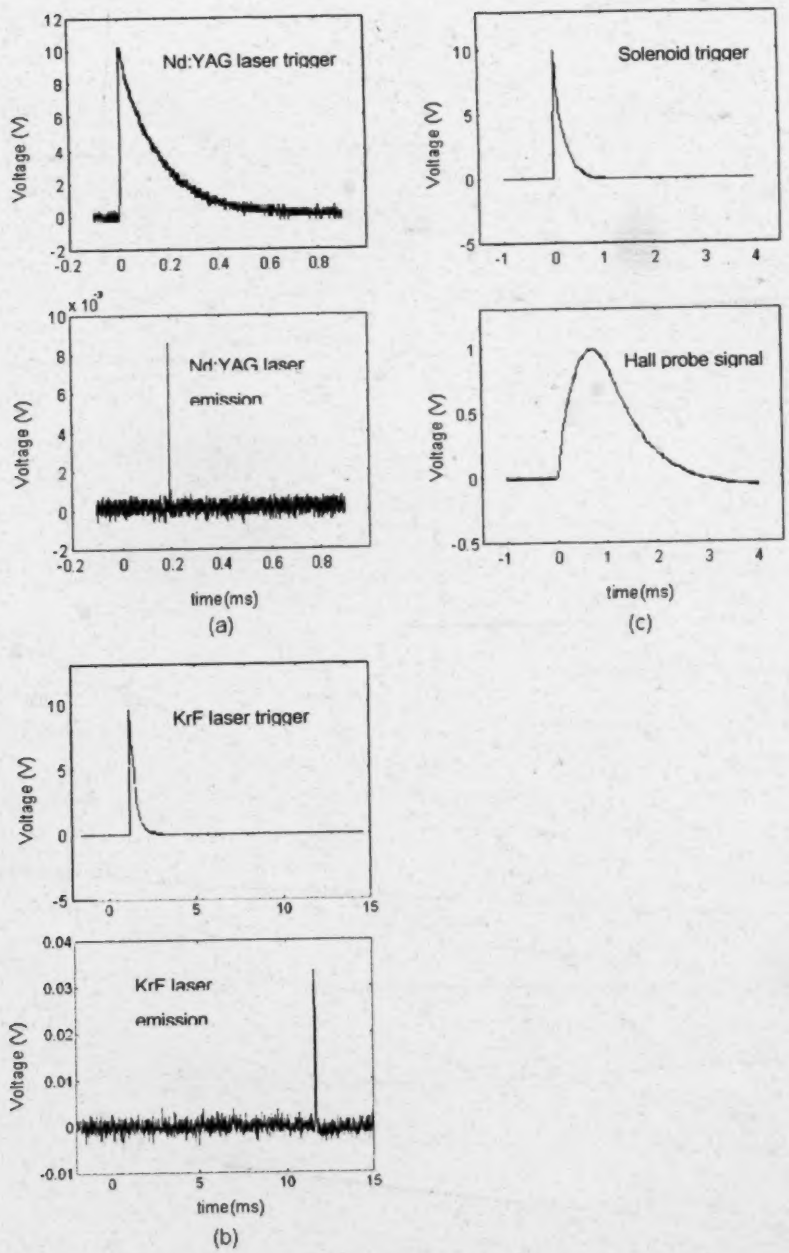

Figure 2-14 Time delay between (a) Nd:YAG laser trigger and laser emission detected by a photo diode (b) KrF laser trigger and laser emission (c) solenoid trigger and magnetic field detected by a Hall probe

2.4 Transport Efficiency Measurement

2.4.1 Langmuir Probe Measurement

The Langmuir probes used are cylindrical copper blocks with a diameter of 6 mm. A DC bias voltage is applied on the probes. The charge flux collected by each probe can be calculated from the voltage pulse measured by oscilloscopes using Equation (2-18).

$$charge\ flux = \int_0^\infty \frac{V(t)}{50\Omega} dt \qquad (2\text{-}18)$$

The total charge (integration of current over time) collected by the Langmuir probe array can be used to estimate the amount of the plasma transported through the magnetic solenoid. The width of the signals can be used to find the plasma temperature if a Maxwellian distribution is assumed.

The Langmuir probes detect charged particles in a laser-produced plasma. A negatively biased probe will repel electrons while a positively biased one will repel ions. As an increasing negative voltage is applied, more and more electrons will be repelled. When the negative potential is large enough, almost all electrons will be stopped before they can reach the probe surface.

To study the influence of bias voltage on Langmuir probe signals, probe signals were measured when bias voltages from –40 V to 40 V were applied to the probes. KrF laser pulses with 20 ns pulse width and 50 mJ pulse energy were used. A silicon wafer with a very smooth surface was used to reduce shot to shot variation due to focal conditions. Probe signals when –40 V, -15 V, 0 V, 15 V and 40 V bias voltages applied are shown in Figure 2-15. When a large enough negative bias voltage is applied, only positive charge flux is observed. It is also observed that the positive charge flux did not change

significantly as the negative bias voltage was set beyond –10 V. It clearly indicates a bias voltage as low as –10 V should be enough to keep most electrons in the plasma flux from reaching the probe surface. A negative and a positive peak are observed when the applied bias voltage is around 0 V. The amplitudes of the two peaks are also observed to be small. The observed signal at zero biased voltage is due to space charge effect. Since electrons move much faster than ions, they reach the probe surface earlier. The resulting charge distribution will generate an electric field to repel electrons and accelerate ions until a stable charge flux is established. The peak values of charge flux at different bias voltages are plotted in Figure 2-16 and Figure 2-17. The positive charge flux starts to saturate at a couple of volts below 0V as the bias voltage decreases. Therefore, a negative bias voltage of -35 V is used in most of our experiments.

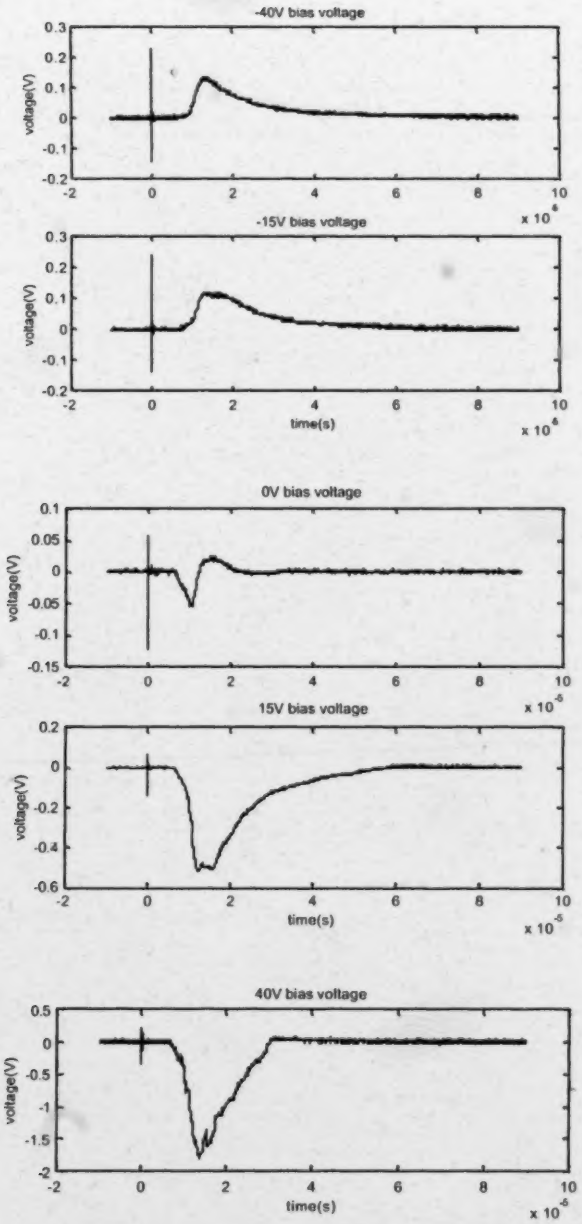

Figure 2-15 Langmuir probe signals of carbon plasma generated by the KrF laser at different bias voltages

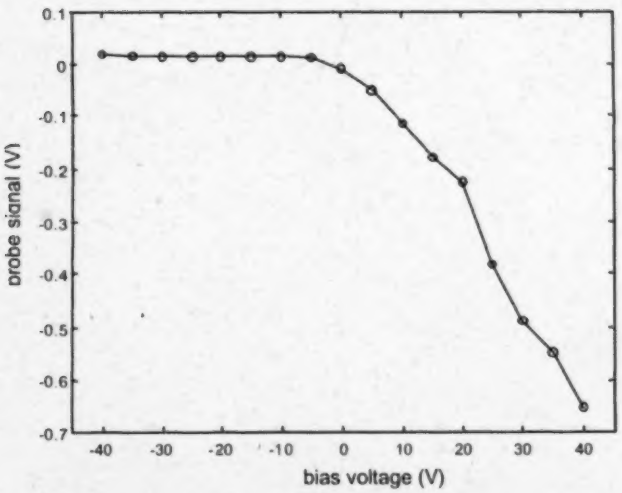

Figure 2-16 Probe signals of carbon plasma generated by the KrF laser at different bias voltages V when no magnetic field is applied

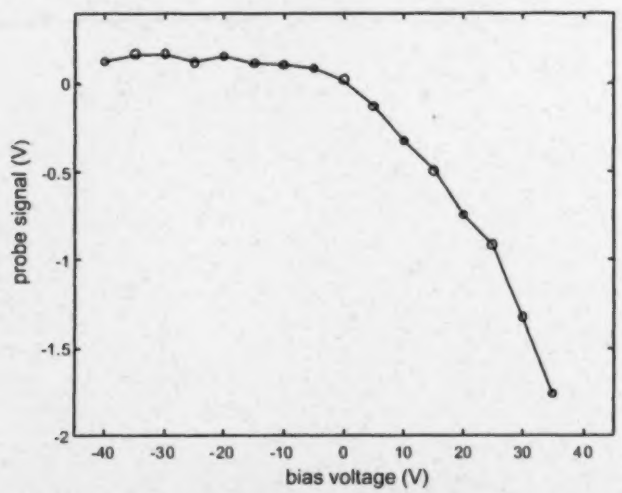

Figure 2-17 Probe signals of carbon plasma generated by the KrF laser at different bias voltages V when a 0.15 T uniform magnetic field is applied

Langmuir probe measurements in the case of graphite target ablation by a 266 nm 4? Nd:YAG laser with 10 ns pulse width and 5 mJ pulse energy are shown in Figure 2-18. The energy intensity is estimated to be 0.45×10^{8} W?cm^{-2}. The target-substrate distance is 49.5 cm and the Langmuir probes are biased at –35 V. Probe signals are output to oscilloscopes through 50 O terminators. The overall charge flux in a single pulse is calculated by integrating the Langmuir probe signals over time, with all peaks included. The average values and error bars from 5 measurements are calculated. As demonstrated in Appendix IV, the total charge flux transported in the solenoid can be estimated from signals of the Langmuir probes at different locations in the probe array, if the density distribution is assumed to be a Gaussian profile approximately. As shown in Figure 2-22 and Figure 2-23, the estimated total charge flux in the solenoid shows a similar trend as the measured charge flux detected by the central probe.

As shown in Figure 2-18 and Figure 2-19, two peaks are observed in the ion flux detected by the probes. The two peaks with different mean velocities are believed to present two different species of ions or ion clusters. The faster peak accounts for less than 2% of the total detected charge flux when B is small (0.03 T), while the faster peak accounts for 5~10% of total charge flux at B = 0.25 T. The peak voltages of the fast peaks at different magnetic fields are plotted in Figure 2-20.

The velocity of ions can be calculated from the Langmuir probe signals using $v=d/t$, where d is the distance from target to probe and t is the arrival time. By calculating the charge flux per unit velocity, the velocity distribution $f(v)$ can be plotted, as shown in Figure 2-19. As described by Equation (1-1) in an earlier chapter, the velocity distribution of a laser plasma is believed to be a shifted Maxwellian distribution. The

fitting results for both peaks are plotted in Figure 2-19 as well. It is found that the velocity distributions agree with the shifted Maxwellian distribution quite well. If the plasma is assumed to consist only singly charged ions, the fitting parameters (width of the Gaussian profiles) imply as a plasma temperature range of 10~20±20% eV.

In order to determine the transport efficiency of charge flux, the dependence of collected charge flux on distance is also studied. A transport efficiency of charge flux as high as 35% is observed, as shown in Figure 2-24, Figure 2-25 and Figure 2-26. The error bars in each figure represent standard deviations of 5 single shots. Charge fluxes detected by a single probe (at the center of the probe array) signals and by the whole probe array area are shown in Figure 2-25 and Figure 2-26 respectively. It is observed that the two curves have similar dependence on B despite of a small discrepancy.

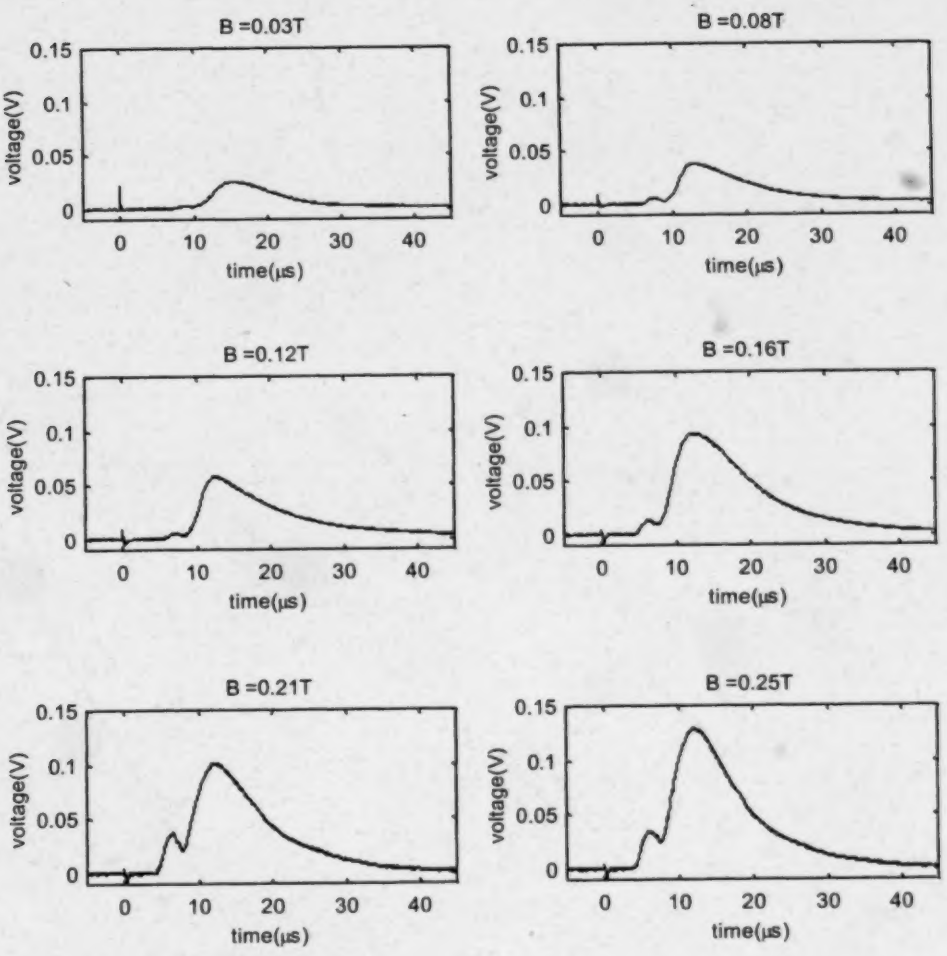

Figure 2-18 Signals detected by the central Langmuir probe at the solenoid exit when different magnetic fields are applied, in the case of Nd:YAG (266 nm) laser ablation of a graphite target

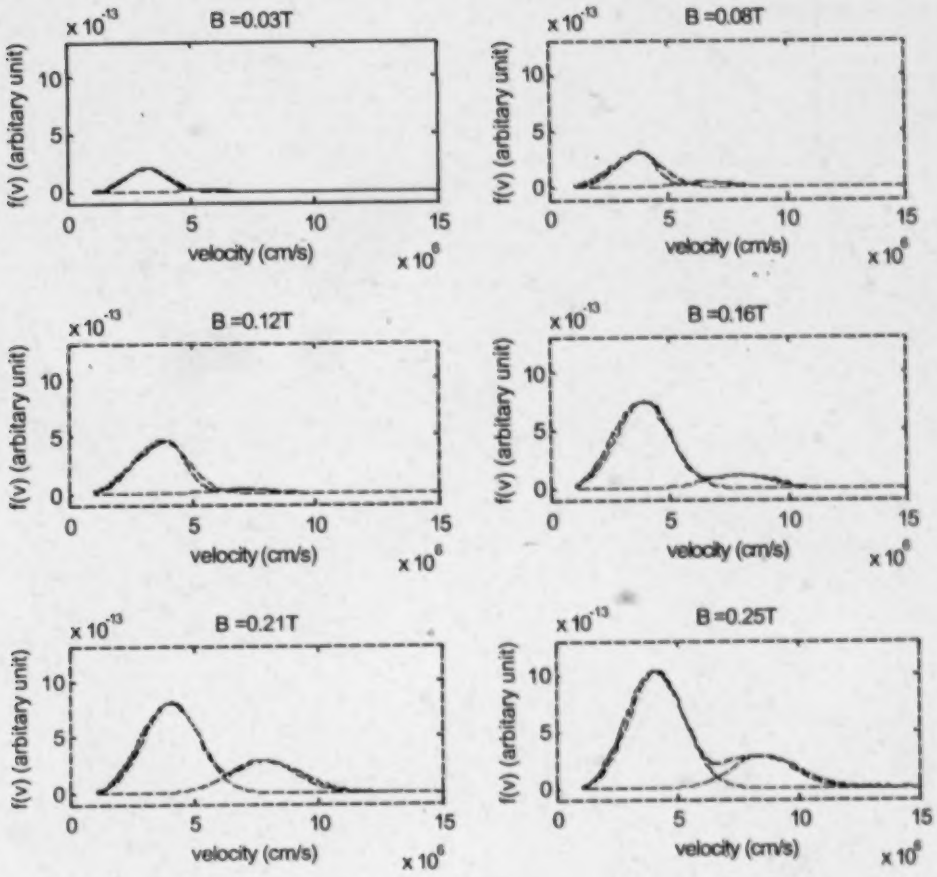

Figure 2-19 Velocity distribution and Maxwellian fitting when different magnetic fields are applied (solid line: calculated from the central probe signals at the solenoid exit, dash line: Maxwellian fitting), in the case of Nd:YAG (266 nm) laser ablation of a graphite target

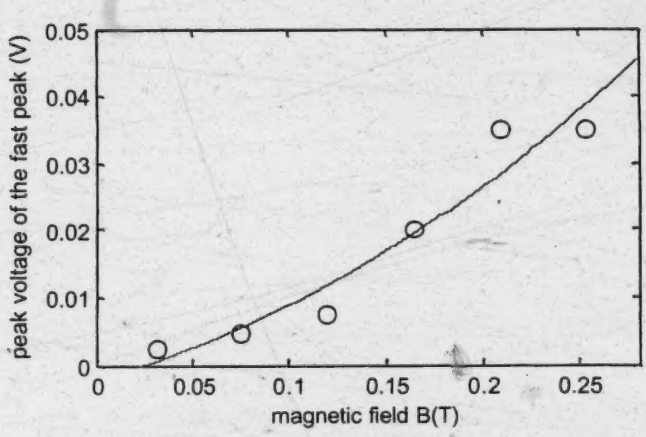

Figure 2-20 Peak voltage of the fast peak detected by the central probe when different magnetic fields are applied

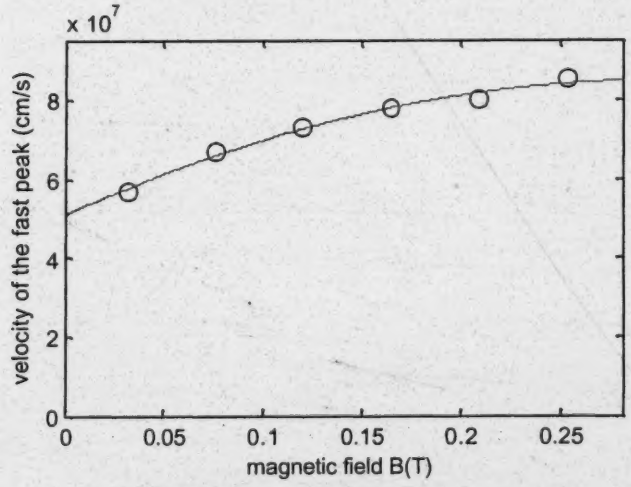

Figure 2-21 Mean velocity of the fast peak detected by the central probe when different magnetic fields are applied

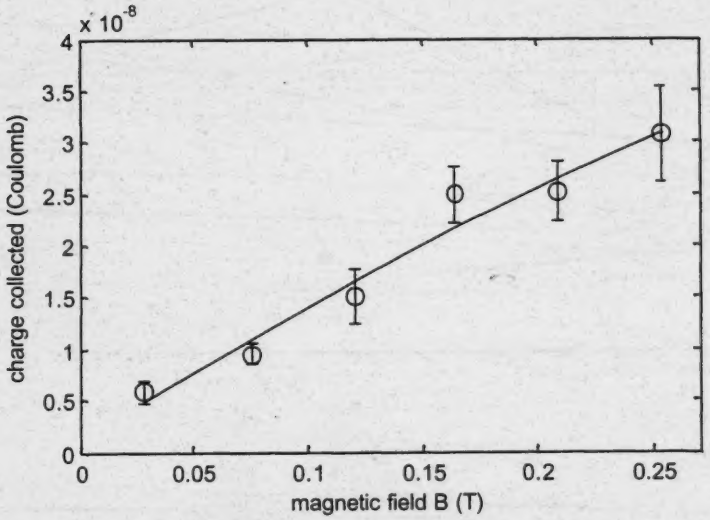

Figure 2-22 Charge flux detected by the central probe at the solenoid exit when different magnetic fields are applied, in the case of Nd:YAG laser ablation of a graphite target

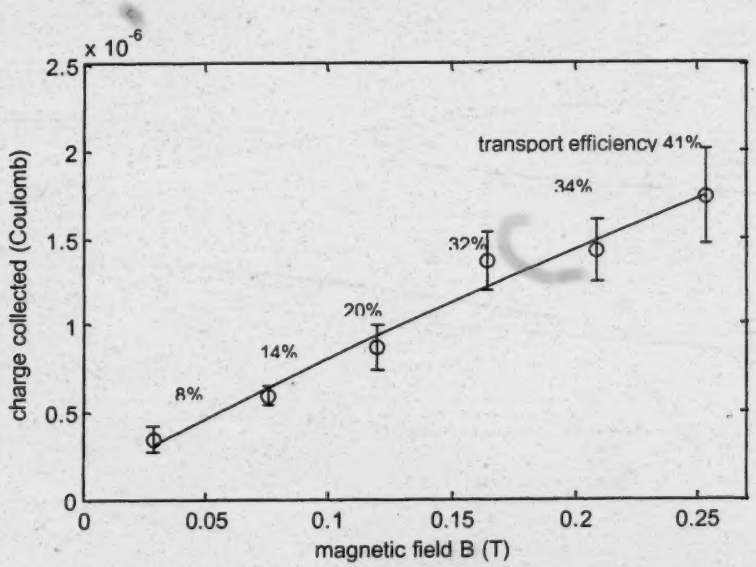

Figure 2-23 Estimated total charge flux transported in the solenoid and transported fraction at the solenoid exit when different magnetic fields are applied, in the case of Nd:YAG laser ablation of a graphite target. Charge flux collected at the entrance of solenoid (3.5 cm from target) is taken as 100%

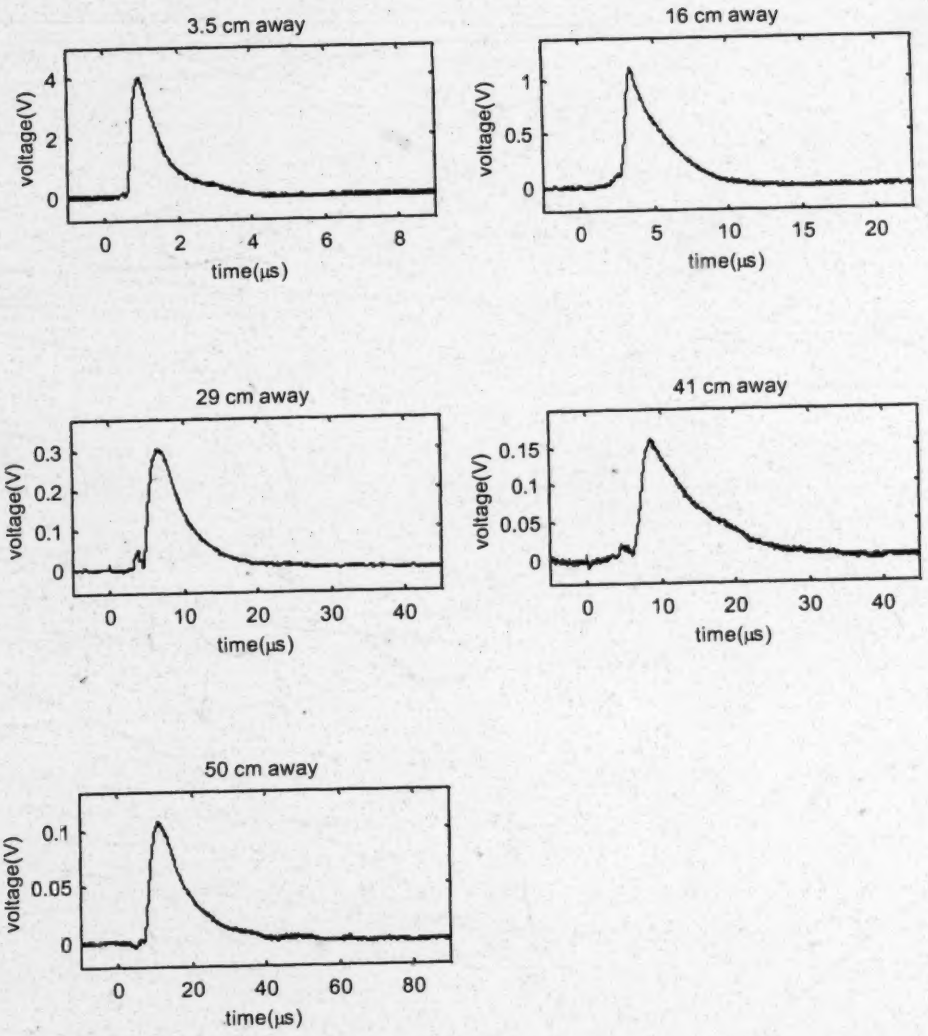

Figure 2-24 Signals detected by the central Langmuir probe at different distances along the solenoid, in the case of Nd:YAG laser ablation of a graphite target, with a magnetic field B=0.25T

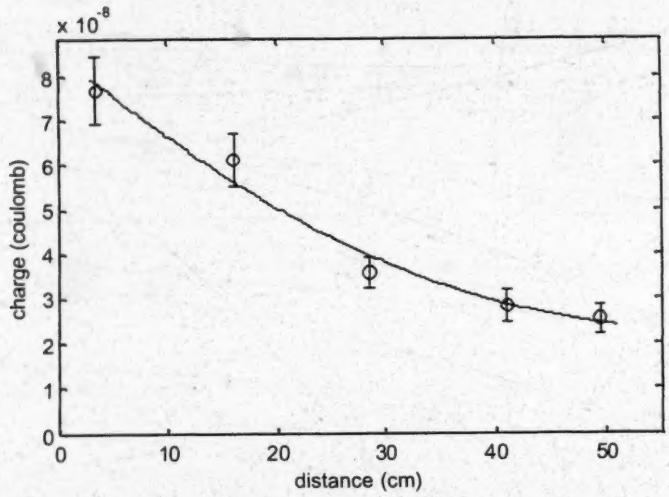

Figure 2-25 Charge flux detected by the central probe at different distances in the case of Nd:YAG (266 nm) laser ablation of a graphite target, with a magnetic field B=0.25T. Charge flux collected at the entrance of solenoid (3.5 cm from target) is taken as 100%

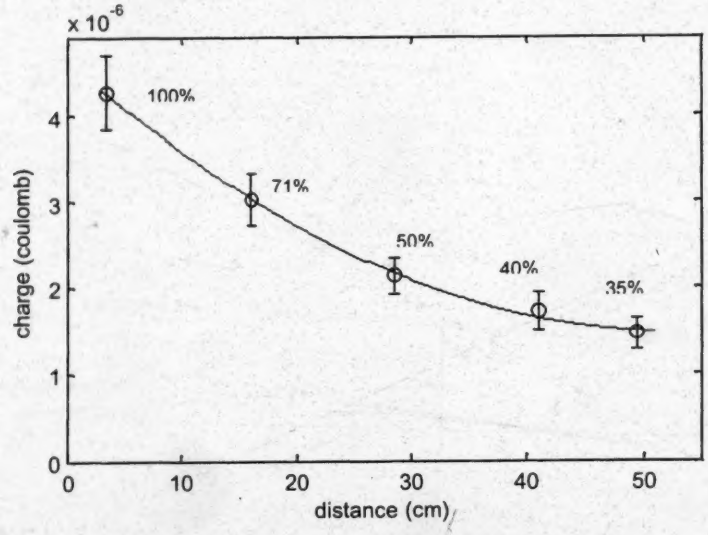

Figure 2-26 Estimated total charge flux transported in the solenoid and transported fraction at different distances in the case of Nd:YAG (266 nm) laser ablation of a graphite target, with a magnetic field B=0.25T

Similarly, carbon plasmas produced by a 248 nm KrF laser pulse with 20 ns pulse width and 50 mJ pulse energy are also studied. The focused beam has a spot size of around 3.0 mm^2, giving a power intensity of 0.83×10^8 W?cm^{-2}.

The Langmuir probe signals averaged from 5 shots are shown in Figure 2-27. The magnetic field varies from 0 to around 0.25T. The bias voltage applied to the probes is –35V, which will repel most electrons away from the probes. In Figure 2-27 to Figure 2-32, the experiment results obtained in the KrF laser ablation case are processed and visualized in a similar manner as that used in the 4ω Nd:YAG laser case. As shown in Figure 2-29 and Figure 2-30, an increase in charge flux is observed as the guiding magnetic field increases. Different from the results in the 4ω Nd:YAG laser ablation case, a saturation in detected charge flux is observed in the high *B* region (see Figure 2-29 and Figure 2-30). As shown in Figure 2-27 and Figure 2-28, fast peaks in the KrF case are not as visible as those in the 4ω Nd:YAG case when *B* is high. The Maxwellian fitting results shown in Figure 2-28 imply a plasma temperature range of 10~15±20% eV. A maximum transport efficiency of charge flux around 40% is observed (see Figure 2-31 and Figure 2-32).

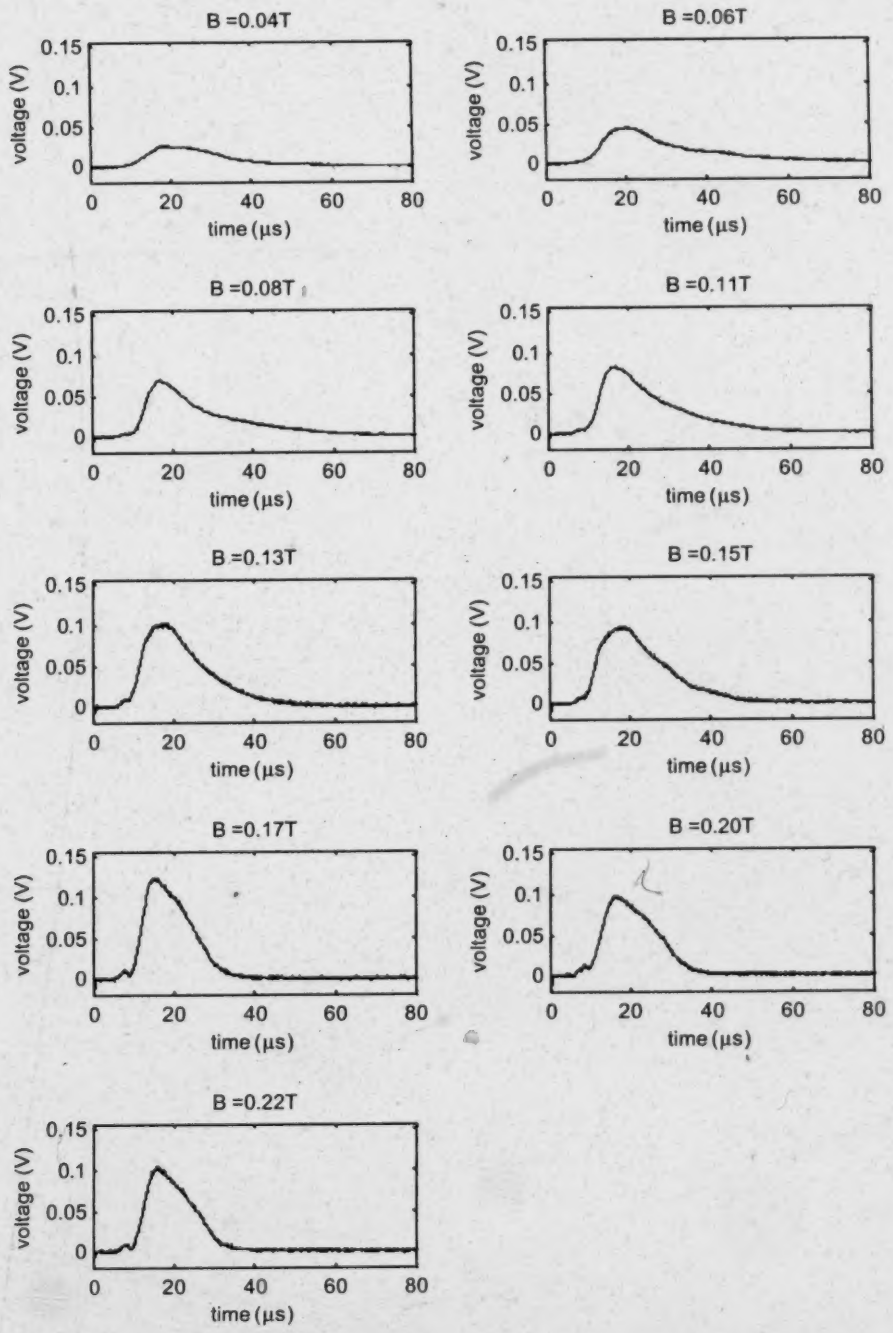

Figure 2-27 Signals detected by the central Langmuir probe when different magnetic fields are applied, in the case of KrF (248 nm) laser ablation of a graphite target

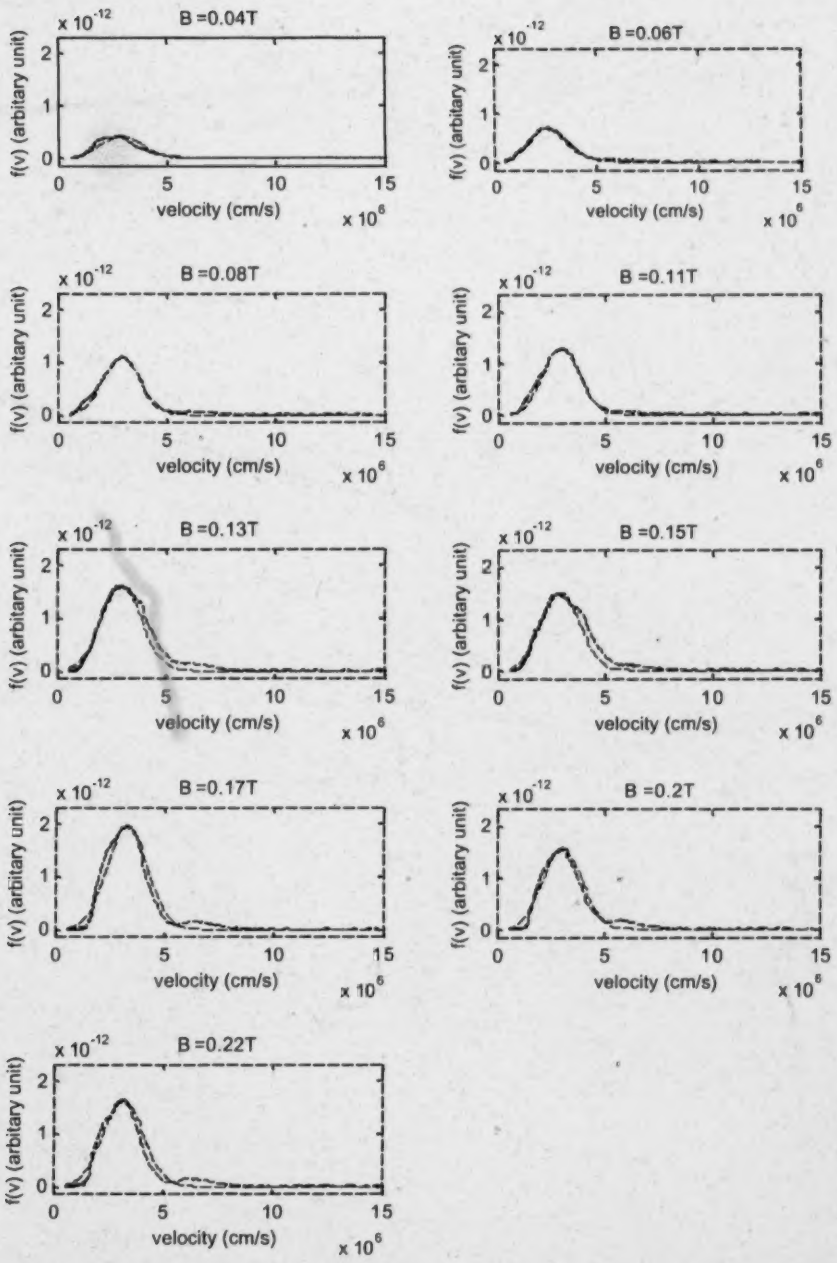

Figure 2-28 Velocity distribution and Maxwellian fitting when different magnetic fields are applied (solid line: calculated from probe signals, dash line : Maxwellian fitting), in the case of KrF (248 nm) laser ablation of a graphite target

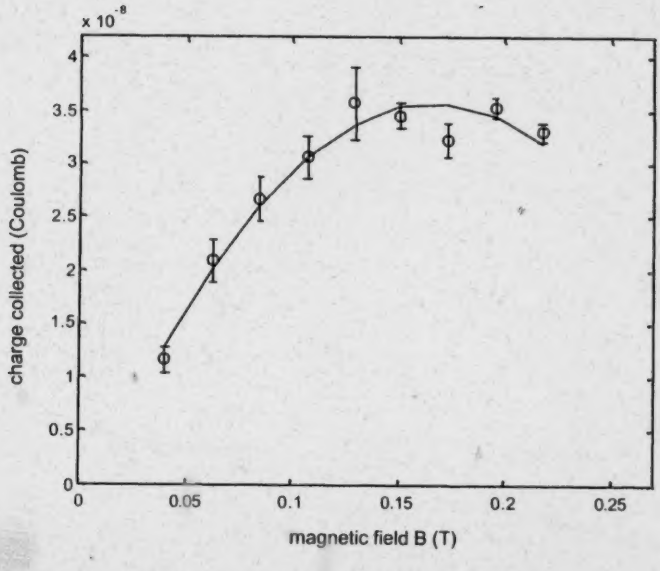

Figure 2-29 Charge flux detected by the central probe at the solenoid exit when different magnetic fields are applied, in the case of KrF (248 nm) laser ablation of a graphite target

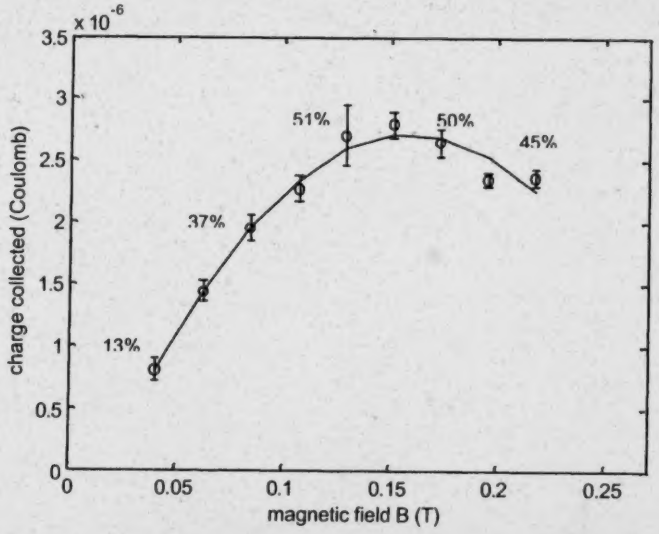

Figure 2-30 Estimated total charge flux transported in the solenoid and transported fraction at the exit of solenoid when different magnetic fields are applied, in the case of KrF (248 nm) laser ablation of a graphite target

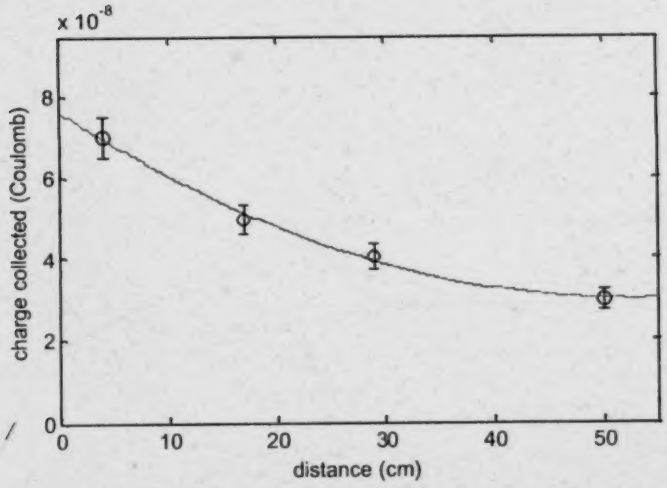

Figure 2-31 Charge flux by the central probe at different distances in the case of KrF (248 nm) laser ablation of a graphite target, with a magnetic field B=0.25T. Charge flux collected at the solenoid entrance (3.5 cm from target) is taken as 100%

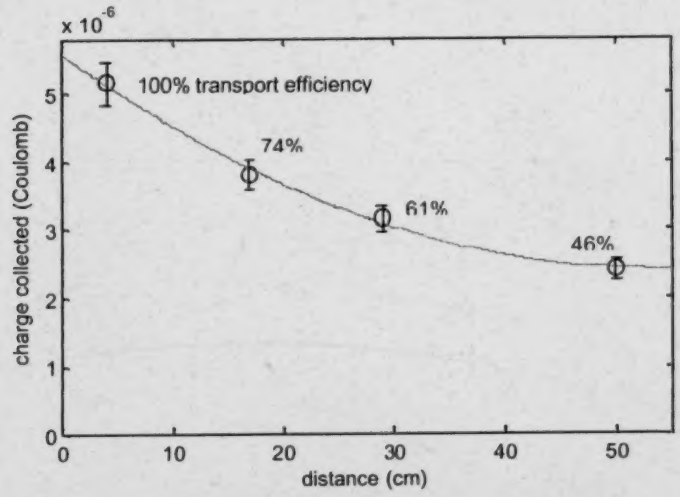

Figure 2-32 Estimated total charge flux transported in the solenoid and transported fraction at different distances in the case of KrF (248 nm) laser ablation of a graphite target, with a magnetic field B=0.25T. Charge flux detected at the solenoid entrance (3.5 cm from target) is taken as 100%

2.4.2 QCM Measurement Results

The transport efficiency of charge flux in the solenoid was investigated by Langmuir probe measurements. To estimate the transport efficiency of mass flux including the neutral species, a QCM detector is placed at the exit of the solenoid to measure the mass deposition rate. Each of the data points is obtained from the time needed to give a thickness reading of 2 Å. The results are listed in Table 2-1 and plotted in Figure 2-33. As discussed before, the thickness reading of QCM is sensitive to the parameter input. While the calibration is made at the much shorter distance, the composition of deposited films could be different at different distances, leading to some errors in the final results. It is also observed that some part of the calibration sample film surface curls up and peels off due to stress. Since the QCM readings are obtained during a relatively long period, any error caused by frequency variation is not very significant. Overall, the QCM reading is expected to be accurate to about a factor of 2.

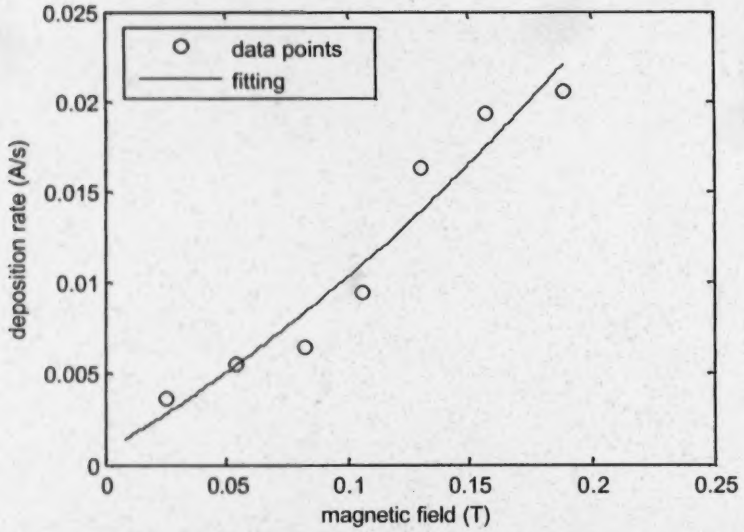

Figure 2-33 Deposition rate measured by QCM at the exit of solenoid when different magnetic fields are applied, in the case of KrF (248 nm, 10 Hz) laser ablation of carbon

Magnetic field (T)	Deposition rate (Å/s)
0.1886	0.0205
0.1571	0.0194
0.1296	0.0163
0.1061	0.0094
0.0825	0.0064
0.0542	0.0055
0.0251	0.0036

Table 2-1 Deposition rate measured by QCM at the exit of solenoid when different magnetic fields are applied, in the case of KrF (248 nm, 10 Hz) laser ablation of carbon

2.5 Discussion of Experimental Results

The experiment results presented above indicate the difference in guiding efficiency when laser beams with different intensities and pulse energies are applied to ablate the target material. For 266 nm wavelength ablation using a Nd:YAG laser with an intensity of 0.45×10^{8} W?cm $^{-2}$ and a pulse energy of 5 mJ, the charge flux increases almost linearly with the magnetic field increases. However, in the case of ablation by a KrF 248 nm laser with a power intensity in the order of 0.83×10^{8} W?cm^{-2} and a pulse energy of 50 mJ, a linear increase of charge flux is observed in low guiding magnetic fields and a saturation of charge flux is observed in relatively in high guiding magnetic fields. However, the measured intensities seem to be too low compared to what was reported in other papers under similar conditions [19][20]. This discrepancy is probably caused by errors in our measurement results.

The results presented earlier have indicated that the magnetic confinement and guiding mechanisms work reasonably well. However, it is also important to notice that the increase in transport efficiency of charge flux in the low B region is significant, but less so at higher B. Charge flux detected by ion probes may even stop increasing at higher B as in the case of KrF 248 nm laser ablation. Similar saturation tendencies are also observed in a magnetic field assisted deposition experiment by Zhitomirsky [12][13], in which a vacuum-arc produced plasma is guided by a magnetic duct to the deposition substrate. However, no explanation or theoretical calculation is given.

A very early study by Bhadra [42] claims that a laser plasma plume propagating across a magnetic field B can be stopped at a distance $R\sim B^{2/3}$. It is believed that this scaling law is due to the balance of the magnetic pressure $P_M\sim B^2$ and the thermal pressure

$P_T=nKT$. Meanwhile, if V represents the plume volume during the laser plasma expansion and $V\sim R^3$, where R is the radius of the expanded plume, P_TV should be kept as a constant. Therefore, a $R\sim B^{2/3}$ dependence can be expected. Similar $R\sim B^{2/3}$ laws are also observed by Harilal et al[43]. Other important phenomena observed by them include an increase in density at early stage, plume lifetime and temperature with the presence of a transverse magnetic field (0.64 T), compared to the case without it. A velocity enhancement is also observed for ion species at shorter distances.

The $R\sim B^{2/3}$ law mentioned above could be compared with our experimental data. In our case, the collected charge flux should obey a $\sim B^{4/3}$ law, if it is proportional to the cross-section area of the plasma density profile. Here it is assumed the magnetic field does not influence the longitudinal propagation of plasma. As shown in Figure 2-34 and Figure 2-35, the $\sim B^{4/3}$ curves fit very well with our data until the saturation effect becomes important. The reason for the saturation or even decrease of charge flux in the KrF laser ablation case is not well understood. Some possible explanations are proposed

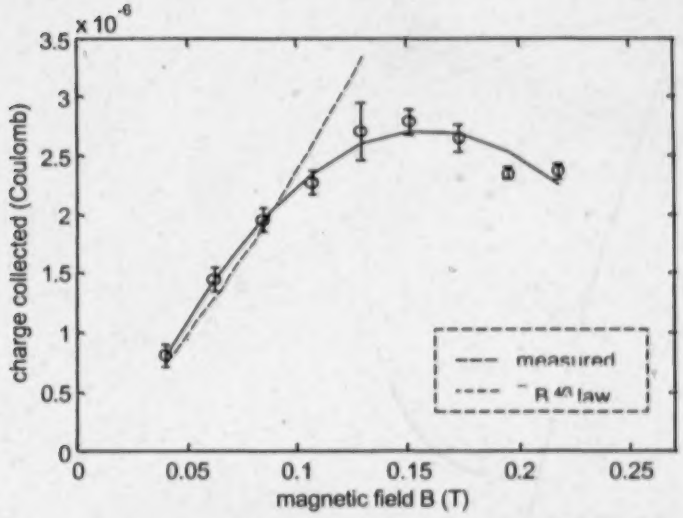

Figure 2-34 Comparison of measured total charge flux and the theoretical results using the ~$B^{4/3}$ law, in the case of KrF (248 nm) laser ablation of carbon

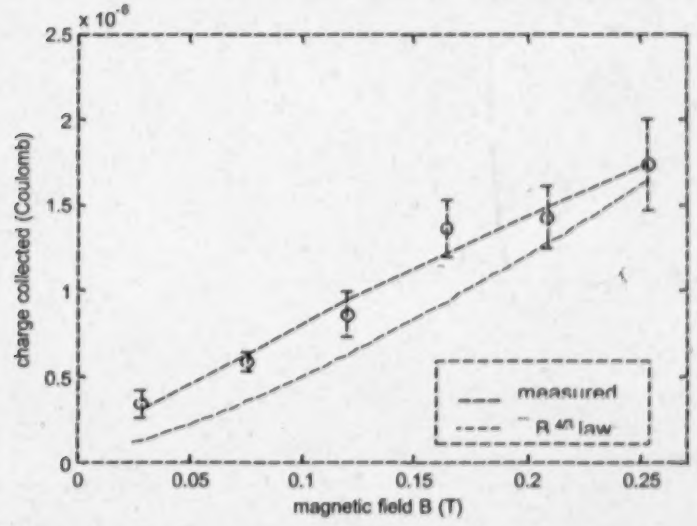

Figure 2-35 Comparison of measured total charge flux and the theoretical results using the ~$B^{4/3}$ law, in the case of Nd:YAG (266 nm) laser ablation of carbon

As introduced before, the magnetic confinement and guiding mechanism might be explained by Lamor gyration. The gyration radius can be described as

$$r_R = \frac{mv_\perp}{qB} \tag{2-19}$$

To get an effective confinement in a solenoid, it is necessary that the Lamor radius r_R of a single ion should be smaller than radius of the solenoid. This effect alone should lead to a nearly 100% transport efficiency by increasing B. However, self-generated fields due to the diamagnetic current in the plasma could have an inverse effect on the magnetic field generated by the solenoid. This is caused by the diamagnetic current. The effect of plasma on the magnetic field is usually measured by the parameter β, which is defined as the ratio of particle pressure and magnetic pressure as shown in Equation (2-20). The inverse interaction of plasma on magnetic field could be described by the pressure balance Equation (2-21).

$$\beta = \frac{p}{B^2/2\mu_0} = \frac{\sum nkT}{B^2/2\mu_0} = \frac{particle\ pressure}{magnetic\ pressure} \tag{2-20}$$

$$\nabla\left(p + \frac{B^2}{2\mu_0}\right) = \frac{1}{\mu_0}(B\cdot\nabla)B \tag{2-21}$$

For plasma in a uniform magnetic field, the sum of particle pressure and magnetic pressure should be a constant. The external magnetic field may not be able to fully diffuse into plasma regions with high densities (high β). For low β plasmas ($\beta = 10^{-3}\sim10^{-6}$), the shielding effect of the magnetic field is usually negligible. However, the diamagnetic effect usually is not negligible when the plasma density is high. In our case, β value is estimated to be in the order of 0.001, if a typical number density of 10^{13} cm^{-3} and a magnetic field B = 0.1 T are assumed. Therefore, the shielding effect should be small.

Nevertheless, some studies by other researchers [43] using fast photography and optical emission spectroscopy indicate the "shielding effect" is not negligible due to the enhanced density on the sharp boundary between plasma and field. It was observed in experiments that the plume propagation across field lines would not be completely stopped. A theoretical discussion by Koopman [44] also suggests the shielding of magnetic field mainly depends on the properties of the outer layer of the plume. This effect may play a more significant role in KrF laser ablation due to a higher energy, compared to the 4? Nd:YAG laser ablation case.

Another possible explanation is that the collisions between particles in the laser-produced plasma are enhanced by the presence of the magnetic field. The enhancement of interactions between particles could give a higher rate of recombinations of ions. The reflection on Lamor gyration inspired an explanation for this enhancement. A possible explanation is that when B increases, the gyration radius r_R gets smaller. The total time of flight along the solenoid is not affected by the guiding magnetic field. Therefore, those ions will have higher probability to "collide" with other particles, because they stay longer in the denser region of the plasma plume now. Here "collision" is generally referred to any interaction between charged particles, including recombination (charge exchange) or merely a change in trajectory (due to the electromagnetic force between charged particles). Since cross-sections for those processes are usually proportional to particle density, more occurrences of collisions could be well expected when B is higher.

The recombination processes can directly affect the charge flux collected at the solenoid exit. Rai et al. [45] indicated emissions due to radiative recombination processes in an aluminum plasma generated by a 532 nm Nd:YAG laser were significantly

enhanced by the presence of a 0.5 T magnetic field. The dominant recombination process in laser-produced plasmas at low temperature is believed to be radiative recombination as described by Equation (2-22), because the cross-section of this process is much higher than that of three-body recombination.

$$C^{i+} + e^- \rightarrow C^{(i-1)+} + h\gamma \qquad (2\text{-}22)$$

A typical three-body recombination process could be described by Equation (2-23). In our case, a carbon ion C^{i+} recombines with an electron e^- and the energy released goes to another electron involved in this process.

$$C^{i+} + e^- + e^- \rightarrow C^{(i-1)+} + e^- \qquad (2\text{-}23)$$

$$\frac{dN_i}{dt} = -\alpha_{ci} N_i \qquad (2\text{-}24)$$

The dynamics of three-body recombination process could be calculated by rate equation (2-24), where N_i is the ion density with charge i. A theoretical calculation [46] indicates that the cross section α_{ci} of three-body recombination process in a laser-produced carbon plasma could be calculated by

$$\alpha_{ci} = \frac{1.9 \times 10^{-27}}{T^{4.5}} i^3 n_e \qquad (2\text{-}25)$$

where i is the charge state of carbon ion, T is plasma temperature in eV and n_e is electron density in CGS units. By using a typical number density 10^{13} cm^{-3} and a 10 eV temperature, the three-body recombination coefficient α_{ci} could be roughly estimated to be in the order of $10^{-18} \cdot i^3$ s^{-1}. Therefore, three-body recombination processes in our case should be negligible for an ion which travels from the entrance to the exit of the solenoid even for high i states.

Nevertheless, it is interesting to notice that studies by Harilal et al. [43] indicated that three-body recombination is a dominant process compared to radiative recombination process in an aluminum plasma produced by a 1.06 μm Nd:YAG laser (8 ns, 4×10^9 $W\cdot cm^{-2}$), with the presence of a 0.64 T transverse magnetic field. Although their parameters are quite different from ours, it is still a good example of how interactions between particles in a plasma could be enhanced by a magnetic field.

It should also be noted that a saturation or even reduction in transported charge flux at higher *B* does not necessarily mean a corresponding change in transported mass flux. Once an ion is captured initially by the *B* field, it probably will continue its motion and reach the exit of the solenoid even though its charge state may be changed by recombination.

There is evidence that a large amount of neutral has arrived the exit of the solenoid when the Langmuir probe measurements (for charge flux) are compared to the QCM measurements. The deposition rate from an ion probe signals are calculated by assuming the average charge number of ions in the plasma is 1. Previous studies [34][48][49] indicated the major components in a carbon plasma produced by a 20 ns KrF laser are C^+ and C^{2+} under similar conditions. Therefore, the charge flux detected by the probes is believed to mainly consist of C^+ and C^{2+} ions. However, some other studies [38][39][47][51] indicates the formation of ion clusters is also possible during the expansion of carbon plasmas produced by UV lasers, although the experiment conditions could be different from ours.

The comparison of deposition rates is shown in Figure 2-36. The discrepancy of these two curves indicates a considerable fraction of carbon materials reaching the exit of the solenoid may be neutrals.

Another possible explanation for the discrepancy is that there is a considerable fraction of the ions are ionic clusters (C_n^+). The presence of ionic clusters was observed [50] in the carbon vapor plume generated by laser irradiation at intensities around 10^8 W?cm^{-2}. The saturation effect as seen in Figure 2-36 for the KrF laser case could be due to the order of magnitude pulse energy used which leads to a more dense plasma, which in turn could result in a higher recombination and cluster formation rates when comparing the less dense plasma as in the 4? Nd:YAG laser case.

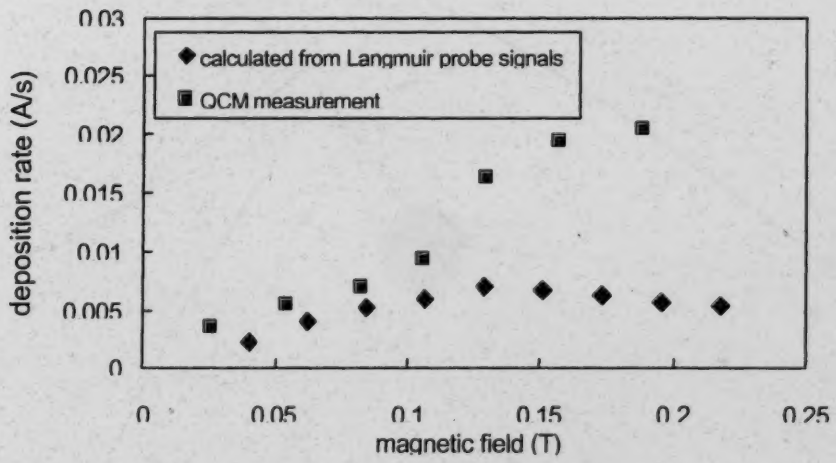

Figure 2-36 Comparison of DLC deposition rate by KrF laser, measured by QCM and calculated results from Langmuir probe signals, assuming ions are singly charged

3 Numerical Simulation

Two different approaches are used to numerically study laser plasmas guided by a straight-line magnetic field. A simple single-particle simulation gives a qualitative prediction of the dependence of plasma transport efficiency on the guiding magnetic field. However, it does not include interactions between particles in the plasma and cannot be used to compare to experimental results quantitatively. Following a previous research work on this topic, a more complicated code based on magnetohydrodynamic (MHD) theories has been developed. The original MHD code in FORTRAN 77 in Cartesian coordinates was written by Dr. Robert Rankin to study the interactions between the solar wind and the magnetosphere. A revised version in cylindrical coordinates was developed by Serguei Roupassov to simulate laser plasma in a curved magnetic field. Based on the original version and using the cylindrical version as a reference, a revised Cartesian program is used to simulate laser plasma in a straight-line magnetic field. The algorithms of the MHD code will be briefly discussed in this chapter. More details can be found in Finnan [32], Rankin [22]-[26] and Roupassov's work [21].

3.1 Overview of Plasma Modeling

As mentioned in the introduction section, a simplistic way to study plasma in a magnetic field is to simulate a number of single particles. Numerically the trajectories of individual particles can be simulated one at a time. The initial state should obey a certain velocity and density distribution. The approach is simple and does not consume a lot of computing power. The simplicity comes at a price of ignoring the interactions between particles. Although the single particle simulation cannot simulate collective behaviors of

particles in a laser plasma, it may still help one to get some general ideas in some cases of magnetic field guiding [21].

A more accurate but complicated modeling approach is to trace multiple particle trajectories simultaneously with the interactions between particles considered, so the collective behaviors of plasma can be simulated. This is called Particle –in-Cell (PIC) simulation. Modern PIC simulation codes can trace up to 10^9 or more particles. But the PIC simulation is at expense of an enormous computing power, and usually an efficient parallel computing code is required.

As another powerful numerical approach, the magnetohydrodynamical (MHD) model treats plasma as a charged fluid. A set of MHD equation could be obtained by combining fluid equations and Maxwell's equations. Mathematically, a set of partial differential equations (PDE) needs to be solved by finite difference algorithms. The initial state can be established from experimental data (density, temperature and velocity), theories (distributions) and assumptions (charge state of ions). The efficiency and success of a finite difference code usually relies heavily on the algorithms employed. For a problem as complicated as laser plasma guided by a magnetic field, an explicit algorithm is usually not adequate to get a stable solution. So implicit algorithms are usually the only feasible approach. In large-scale 3D simulations, 3D calculations can be simplified to a sequence of separate 1D calculations. Therefore, the Alternating Direction Implicit (ADI) finite difference algorithm is chosen in our case. Theoretical details and algorithms of MHD simulation are discussed in a later part of this thesis.

3.2 Single-particle Simulation

A Monte-Carlo single-particle code is developed by me to study the guiding behavior. Transported fractions of laser plasma along the straight-line magnetic field are calculated at different B values. Although the interactions between particles in the plasma are not considered in this simulation, this simulation still gives a good estimation of the maximum possible guiding efficiency that could be obtained at a certain magnetic field strength. By including the electric field induced by charge separation in a "flux-tube" model, an improved single-particle simulation was used to study plasma in a curved magnetic filter by Boercker et al. [65]. This approach takes advantage of the computational efficiency of single-particle simulation without compromising all features of the plasma "fluid". Without this important inclusion, important phenomena like drifting of guiding center could not be simulated and understood in the curved magnetic field case. Nevertheless, this is not a concern in the case of straight-line magnetic field, so a "pure" single-particle simulation code is used.

3.2.1 Single-particle Simulation Algorithm

The purpose of this simulation is to study the transport efficiency of a laser-generated carbon plasma in a uniform magnetic field, i.e. what is the transported fraction of the initial plasma. One of our major concerns is what is the dependence of the transported fraction on the strength of the guiding magnetic field B.

A Monto-Carlo simulation code is developed to calculate the trajectories of individual particles in a laser-produced carbon plasma in a guiding magnetic field. First of all, enough carbon ions with certain density and velocity distribution are generated.

Here ? and f are assigned as polar angle (with respect to normal direction) and azimuthal angle, respectively, as shown in Figure 3-1. As mentioned before, a $cos^n(?)$ density distribution is widely observed in typical laser-generated plasmas. Usually the forward peaking parameter n varies from 4 to 8. Therefore, n = 4, 6, 8 is used in our simulation. As for f, a uniform distribution is assumed for simplicity.

The velocity distribution of laser plasmas could be described with the assumption of a Maxwellian distribution with a drift velocity u along the normal direction shown in Equation (3-1). A shifted Maxwellian profile with a mean velocity of 4×10^6 cm/s and a width of 2×10^6 cm/s in the direction of magnetic field is simulated. Those values come form the typical profile observed in our experiments. The trajectories of individual ions are then calculated one by one. Finally, the number of particles that make it through the solenoid can be counted.

$$f(v_x, v_y, v_z) = \left(\frac{m}{2\pi kT}\right)^{3/2} \exp\{-(m/2k_BT)[v_x^2 + v_y^2 + (v_z - u)^2]\} \qquad (3\text{-}1)$$

The trajectory of a charged particle is calculated by using the equation of motion:

$$m\frac{d\bar{v}}{dt} = q(\bar{E} + \bar{v}\times\bar{B}) + mg \qquad (3\text{-}2)$$

$$\frac{d\bar{x}}{dt} = \bar{v} \qquad (3\text{-}3)$$

where m, q, v and x represent the mass, charge, velocity and position of a single particle. In the case of a singly-charged carbon ion, $m = 2.0\times10^{-26}$ kg and $q = 1.6\times10^{-19}$ C is used in the calculations. And B and E are magnetic field and electric field, respectively. Because the time-of-flight of ions along the solenoid is around 10 μs, the shift distance of ions caused by gravity is only in the order of 10^{-8} cm. Therefore, the gravity term mg is

usually ignored in Equation (3-2). The qE term is also ignored because there is no electric field if no flux-like feature or interactions between particles are considered here. Since there are only time derivative terms in the equations set, an explicit finite difference algorithm is used to get the numerical solution.

It is necessary to set up a criteria to decide what kind of ions can be guided through the solenoid. To simplify the case, it is assumed that as long as an ion moves to the edge of a certain region, which corresponds to inner space of solenoid, it is lost. The distance from the target to the solenoid entrance is set to the experimental value d =3.5 cm. Any single ion will move freely in the first 3.5 cm. Once an ion reaches the exit of the solenoid or strikes the solenoid wall, its trajectory will not be calculated any further.

Because the simulated particles are generated one by one and not related to each other, the number of particles is only required to be statistically large enough to give a reasonable representation of the angular density distribution and a Maxwellian velocity distribution. This is different from particle-in-cell (PIC) simulation, where the more particles are simulated the better because the trajectory of each particle is affected by electromagnetic force exerted by other particles.

The number of singly charged carbon ions used in the simulation is 20,000. The seed of the random number generator is set to be a certain number to make the simulated ions the same in all cases. The Transport efficiency of those ions with different $cos^n(?)$ distributions and at different B is studied. The geometry is shown in Figure 3-1, where is $?$ the polar angle and f is the azimuthal angle. The $cos^n(?)$ distribution is generated using Monte-Carlo method. As illustrated in Figure 3-2, a pair of random numbers $?$ in the range of 0~90° and p in the range of 0~1 are generated each time. The polar angle $?$

corresponds to the shooting angle of a particle with respect to normal direction. If p falls into the area under the $cos^n(?)$ curve, the $?$ value will be kept. If not, $?$ will be discarded. This procedure was repeated until the number of particles kept reached an assigned total particle number N. In the end, the probability p of getting a certain $?$ value will be proportional to $cos^n(?)$. Because an axis-symmetric density profile can be assumed in most cases, a uniform distribution is generated in the direction of the azimuthal angle F. A Maxwellian velocity profile could be generated in a similar way. During the calculation of ion trajectories using the equation of motion, the spherical coordinates used in the particle generation process are converted into Cartesian coordinates. The simulation program written in MATLAB is listed in Appendix V.

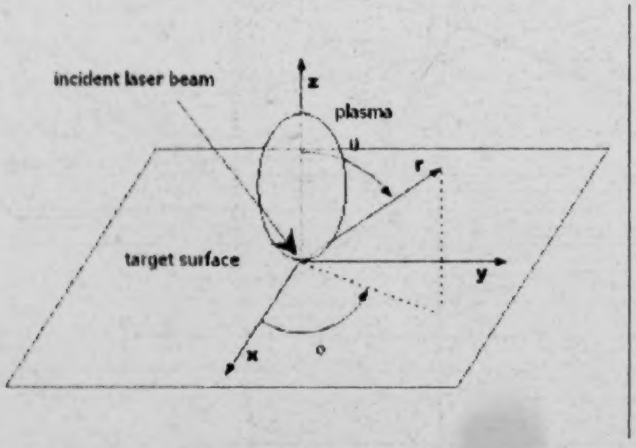

Figure 3-1 Geometry of the laser-produced plasma in the single-particle simulation

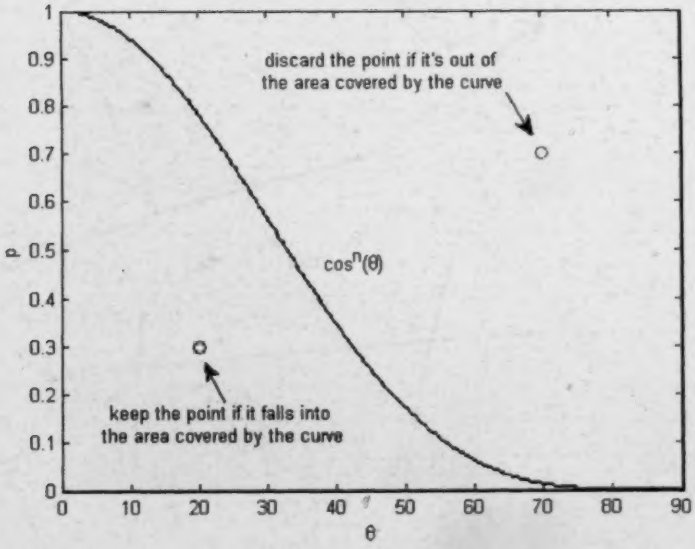
discard the point if it's out of
the area covered by the curve
cos^n(θ)
keep the point if it falls into
the area covered by the curve
p
θ

Figure 3-2 Monte-Carlo algorithm used to generated a cos^n(?) density distribution

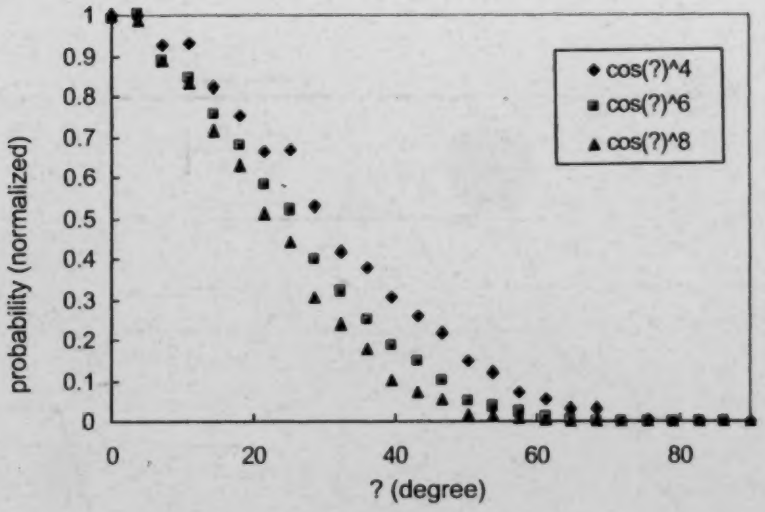

Figure 3-3 Angular distributions of 20,000 ions generated by a Monte-Carlo code

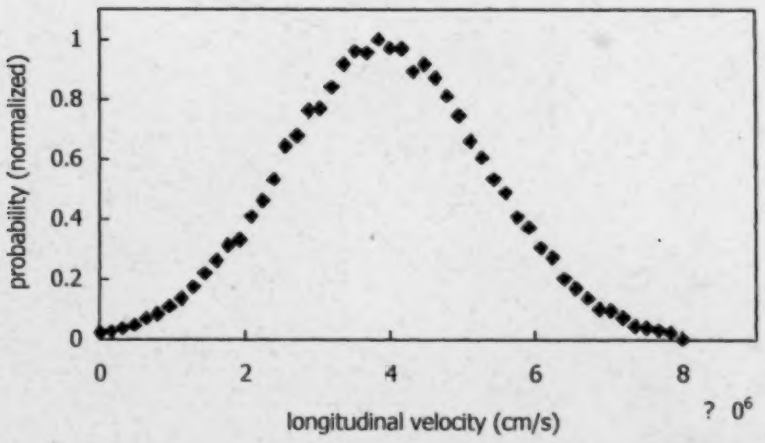

Figure 3-4 Maxwellian distribution of longitudinal velocity of 20,000 ions generated by a Monte-Carlo code. With a peak at 4×10^6 cm/s and a width of 2×10^6 cm/s

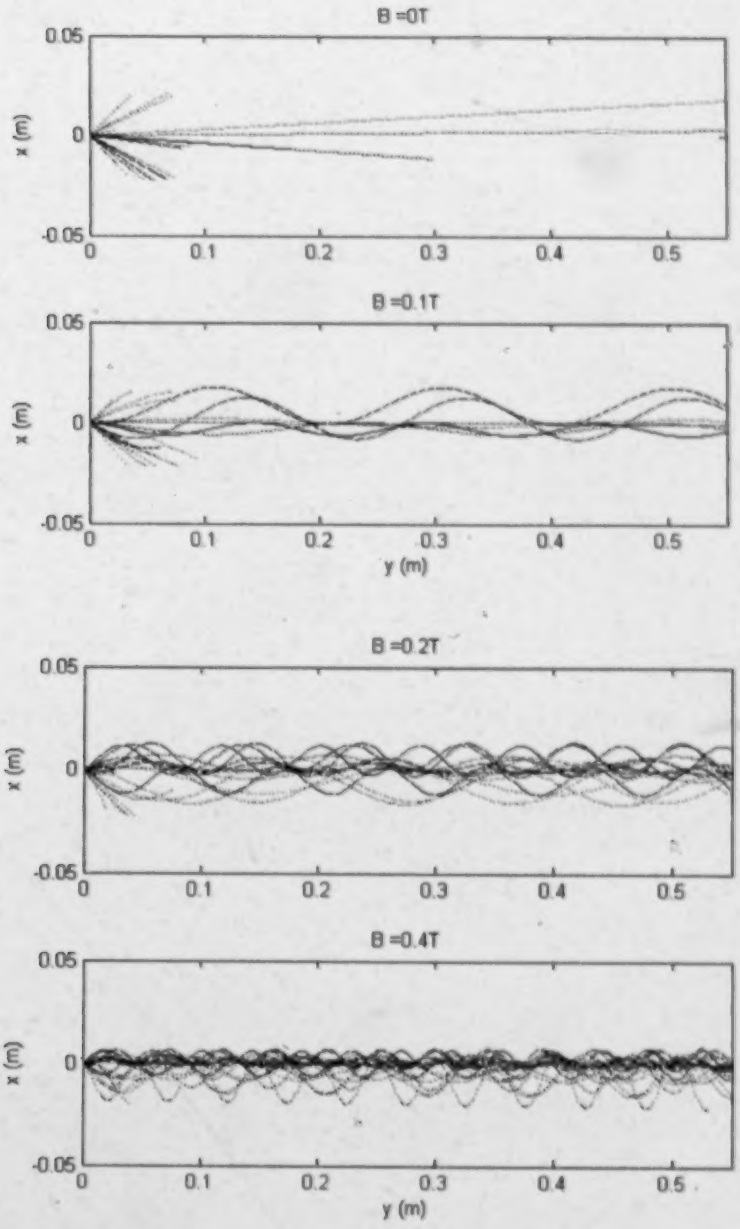

Figure 3-5 Simulated trajectories of 20 random individual C^+ ions satisfying $\cos^4(?)$ distribution at different B values

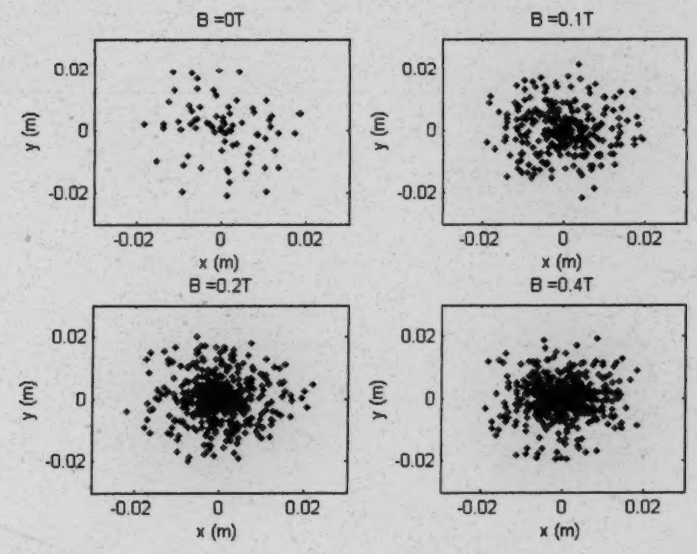

(a)

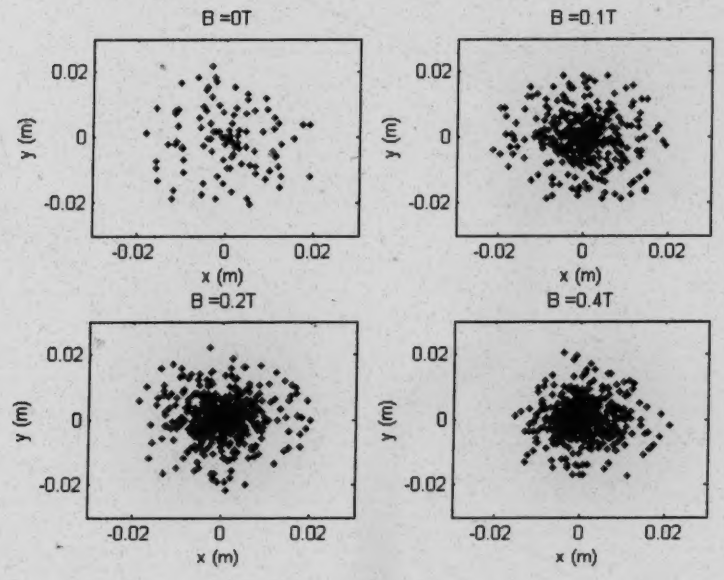

(b)

Figure 3-6 Distribution of transported C^+ ions at the exit of solenoid at different B values. 1,000 initial C^+ ions satisfying (a) an initial $cos^4(?)$ and (b) $cos^8(?)$ distribution are used.

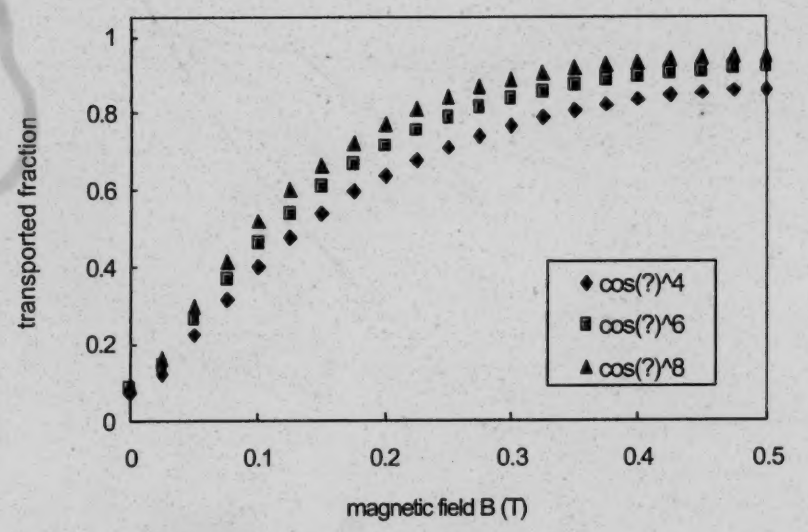

Figure 3-7 Transported fraction of plasma containing 20,000 C^+ ions at the exit of the solenoid (55 cm away from target) with different initial density distributions

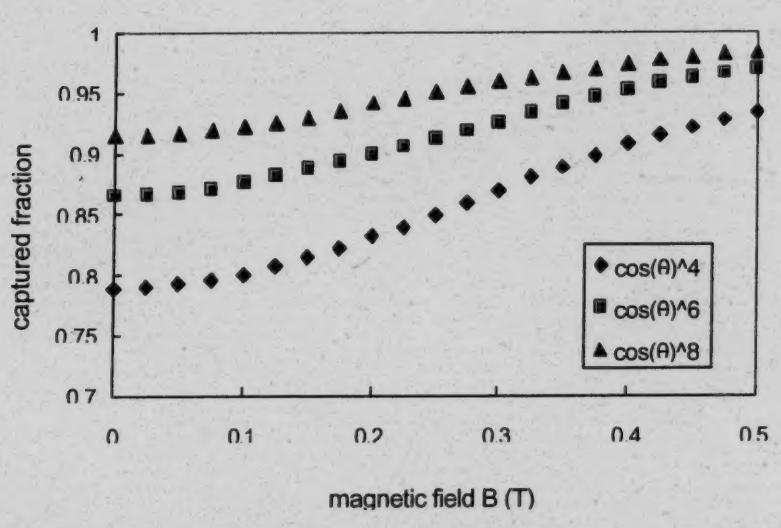

Figure 3-8 Captured fraction of 20,000 initial C^+ ions at the entrance of solenoid (3.5 cm away from target) with different initial density distributions

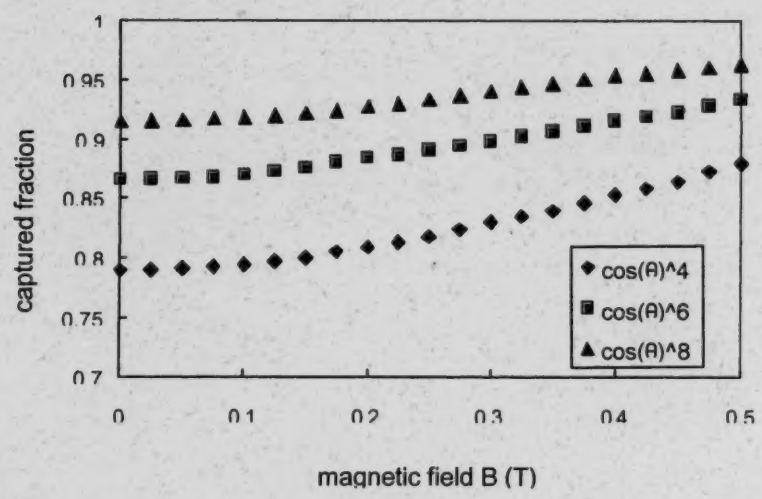

Figure 3-9 Captured fraction of 20,000 initial C^+ ions at the entrance of solenoid (3.5 cm away from target) with different initial density distributions, when a non-uniform B distribution is considered at the solenoid entrance

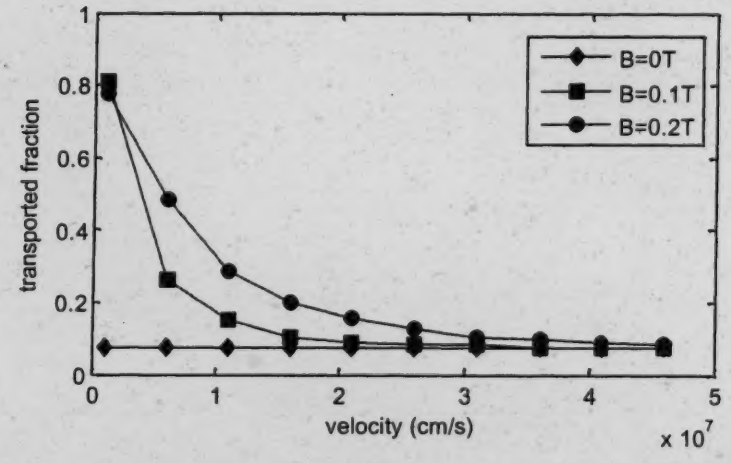

Figure 3-10 Transported fraction of plasma containing 20,000 C^+ ions at the exit of the solenoid (55 cm away from target) with different initial mean velocities, *cos⁴(?)* initial density distributions are used

3.2.2 Single-Particle Monte-Carlo Simulation Results and Discussion

The single-particle simulation results are shown in Figure 3-3 to Figure 3-8. As shown in Figure 3-3, the density distributions of the 20,000 random carbon ions generated by the Monte-Carlo code represent desired $cos^n(?)$ functions very well. In reality, the n value in the $cos^n(?)$ initial density distribution is mainly decided by characteristics of the ablation beam and target properties. The larger the n value is, the more "forwarding" the initial plasma will be. n = 4, 6 and 8 [34] are used in the simulations. A simulated Maxwellian profile of the 20,000 carbon ions centered at 4×10^6 cm/s with a width of 2×10^6 cm/s is shown in Figure 3-4.

The trajectories of 20 individual carbon ions are plotted in Figure 3-5. A difference in guiding behaviors when B increases is observed in our simulation results. When there is no magnetic field (B =0), only particles with small ? can go through the solenoid without hitting the wall. When B increases, more and more particles will survive the guiding length due to then smaller Lamor radii. This is indicated by a more concentrated particle distribution at the exit of solenoid at higher B, as shown in Figure 3-6. The dependences of capture efficiency (at solenoid entrance d=3.5 cm) and overall guiding efficiency (at solenoid exit d=55 cm) on B are shown in Figure 3-7 and Figure 3-8. As mentioned in the introduction section, the gyration radius (Lamor radius) of a charged particle is

$$r_R = \frac{mv_\perp}{qB} \qquad (3\text{-}4)$$

where $v_\perp$ is transverse component with respect to magnetic field B. Since r_R is proportional to $1/B$, it is expected that a smaller number of charged particles will strike the inner wall of solenoid due to smaller r_R when B is higher.

Apparently, the number of transported ions cannot grow infinitely. It is limited by the total number of ions in the plume. More ions shooting at larger ? will be guided through the solenoid at a larger B. However, the number of ions directed at large ? is not that significant compared to the number of those at small ? in the $cos^n(?)$ density distribution. Therefore, the guiding efficiency cannot increase for high B values as fast as for low B values, as shown in Figure 3-7.

The period of a Lamor gyration is given by

$$T_R = \frac{2\pi r_R}{v_\perp} = \frac{2\pi m}{qB} \qquad (3\text{-}5)$$

Here T_R is only related to the species of charge particles (mass-charge ratio) and magnetic field B, regardless of the transverse velocity $v_\perp$. An estimation of number of gyration cycles will be helpful in our case. According the experimental results introduced in a previous section, the average longitudinal velocity of carbon ions generated by KrF 248 nm ablation is about 4×10^6 cm/s along the magnetic field. For a singly charged carbon ion C^+, the total time-of-flight through the solenoid will correspond to 1.8 gyration cycles if B =0.1T. And the gyration radius will be 1.3 cm, 2.8 cm and 8.3 cm when ? = 15°, 30° and 60°.

The simulated guiding efficiency agrees reasonably well with our experimental results when B is small. However, the discrepancy at larger B values is believed to be due to the fact the interactions between particles in the plasma are ignored. Because the

gyration radius r_R is much smaller in a stronger magnetic field, i.e. the plasma plume is more concentrated, ions are expected to stay longer in the region with higher density and more collisional processes like radiative or three-body recombination could occur. Thus for a solenoid with radius of 2.5 cm, the ions with ? =30° will travel through the solenoid without hitting the wall at B =0.1T.

The magnetic field generated by a solenoid is not uniform at the solenoid entrance. It mainly changes the capture efficiency of the laser plasma. To estimate the difference due to the non-uniformity of B, simulation results using the calculated non-uniform B distribution (as shown in Figure 2-6) are plotted in Figure 3-9. A less than 5% loss in captured fraction is observed, compared to the results using the uniform B distribution at the solenoid entrance in Figure 3-8. The simulated transport efficiencies using different initial mean velocities are shown in Figure 3-10, in which dropping transported fractions of ions are observed when larger initial mean velocities are used in simulation. The reason for this tendency is that when the transverse velocities of ions will be larger when the mean velocity is larger, the resulting larger gyration radius will then cause more loss of ions.

3.3 Magnetohydrodynamics (MHD) Simulation

3.3.1 MHD Theories and ADI Algorithm

Magnetohydrodynamic (MHD) theory treats the plasma like a fluid and the particle velocity distribution is assumed to be Maxwellian The ions and the electrons could be either treated separately (two-fluid theory) or treated as the linear combination of these

two species (single-fluid theory). In our MHD simulation, the single-fluid theory is used. A book by F.F. Chen [30] can be used as a reference on MHD theories (and other theories as well).

The single-fluid MHD equations are a set of partial differential equations (PDE). Alternating Direction Implicit (ADI) finite difference algorithm is used to solve the set of equations. Because the computer program is mainly based on the works by R. Rankin [23]-[26] and S. Roupassov [21], theories and algorithms will not be discussed in detail in this thesis. The original descriptions and discussions on the application of the ADI algorithm in MHD simulations are in an earlier paper by C.H. Finan III [32]. Some interesting comparisons on various finite difference algorithms can be found in a book by W.H. Press [33].

3.3.2 MHD Simulation Results and Discussions

The propagation of a carbon plasma in a uniform magnetic field is simulated in a volume of 5×5×70 cm^3. Spatial step size is set to be $?x_1 = ?x_2 = ?x_3 = 0.2$ cm. To reduce the possible problems caused by boundary conditions, the simulation dimension in the propagation direction x_3 is set to be larger than the real length of solenoid. Since the plasma density has dropped to a relatively low level close to the x_1, x_2 boundaries, the boundary conditions in x_1, x_2 directions are not our major concern and the dimensions in these two directions are set the same as those of the real solenoid.

The simulated carbon plasma is set to consist of only singly charged carbon ions C^+. The initial density profile of plasma plume is defined the as Gaussian, with a maximum

value of 10^{11} cm^{-3} and a width of 0.5 cm (where the density *?* drops to e^{-1} of max density $?_0$) in both x_1 and x_2 directions. The width in the propagation direction x_3 is set to be 2 cm. As mentioned before, a background density is required to improve the numerical stability. In our simulation, this background density is set to be 1% of the maximum density in initial state.

Several improvements proposed by S. Roupassov [21] have been made to reduce run time of this simulation. The limitation on time step size Δt is mainly determined by the Courant-Friedrichs-Lewy (CFL) stability criterion in finite difference algorithms $\Delta x/\Delta t > V_A$, where V_A is the Alfvén velocity $V_A=B/(4\pi\rho)^{1/2}$, Δx and Δt are grid size and time step size, respectively. A background density can be introduced in the simulation so that the maximum Alfvén velocity is limited and a larger Δt can be used. Another way to ease the limitation imposed by V_A is to introduce a damping factor to the Lorentz force terms.

A 2nd-order diffusion term $D\nabla^2 u$ is introduced in the advection term $(\partial/\partial t + v\cdot\nabla)$ to suppress instabilities. As expected, value of diffusion coefficient D plays an important role in the evolution of density profile, with or without magnetic field. The choice of D value should not be too large so that plasma profile would not diffuse too fast, at the same time not small so that it can still suppress numerical instabilities effectively. Simulation results using 2 different D values are shown in Figure 3-11 and Figure 3-12. A plasma plume with a Gaussian initial density profile and a uniform drift velocity is simulated to expand freely into vacuum when this is no magnetic field (B=0). The comparison of these two results indicates the plasma diffuses faster when a larger 2nd-order diffusion coefficient D is used. As proposed in S. Roupassov's work [21], an extra 4th-order

diffusion term $-D_4\partial^4 u/\partial x^4$ can also be added to suppress perturbations at short wavelengths without dissipating the simulated plasma profile too much.

Despite the above techniques to suppress numerical instabilities have been proposed and partly implemented, parameters of the current version of the simulation code still require more fine tunings when complicated cases such as non-uniform velocity profile are simulated. Therefore, a uniform velocity $V_3=V_0= 3.5\times10^6$ cm/s is implemented in the whole simulation region, while $V_1=V_2=0$ everywhere at $t=0$. To realistically simulate the capturing and guiding of our magnetically guided plasmas, the implement of a non-uniform velocity profile is needed in the future, which currently is still not possible due to numerical instabilities.

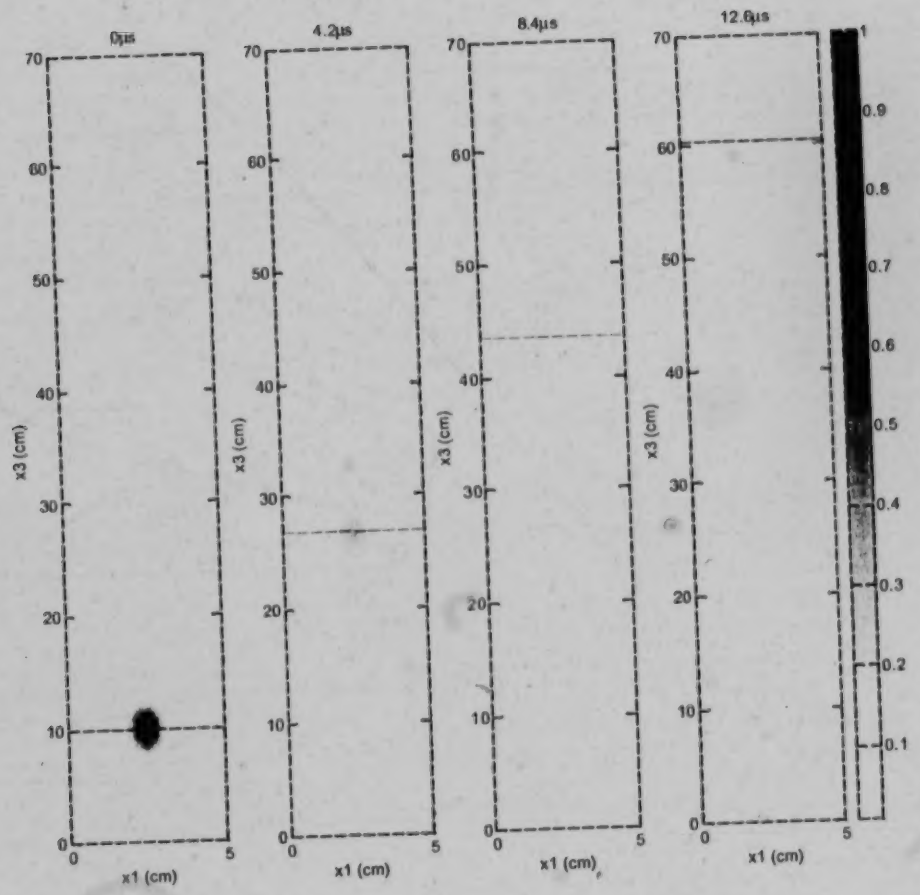
0μs
4.2μs
8.4μs
12.6μs
x3 (cm)
x1 (cm)
0
10
20
30
40
50
60
70
5
0.1
0.2
0.3
0.4
0.5
0.6
0.7
0.8
0.9
1

(a)

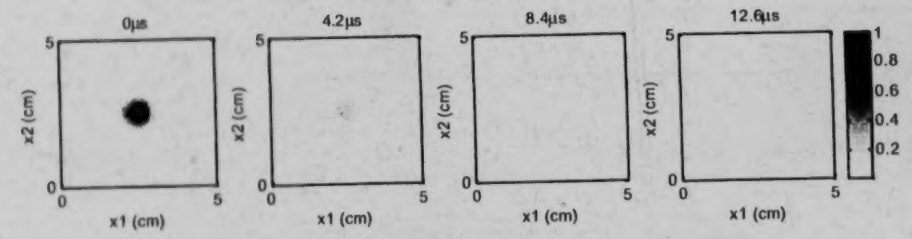

(b)

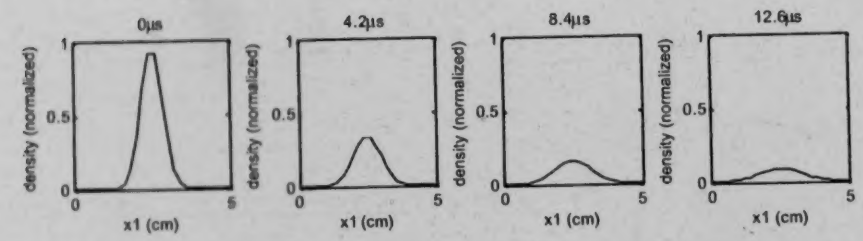

(c)

Figure 3-11 Simulated density (normalized) profile of laser plasma with magnetic field B=0, with a diffusion coefficient D = 10^{-3} $cm^2 \cdot s^{-1}$

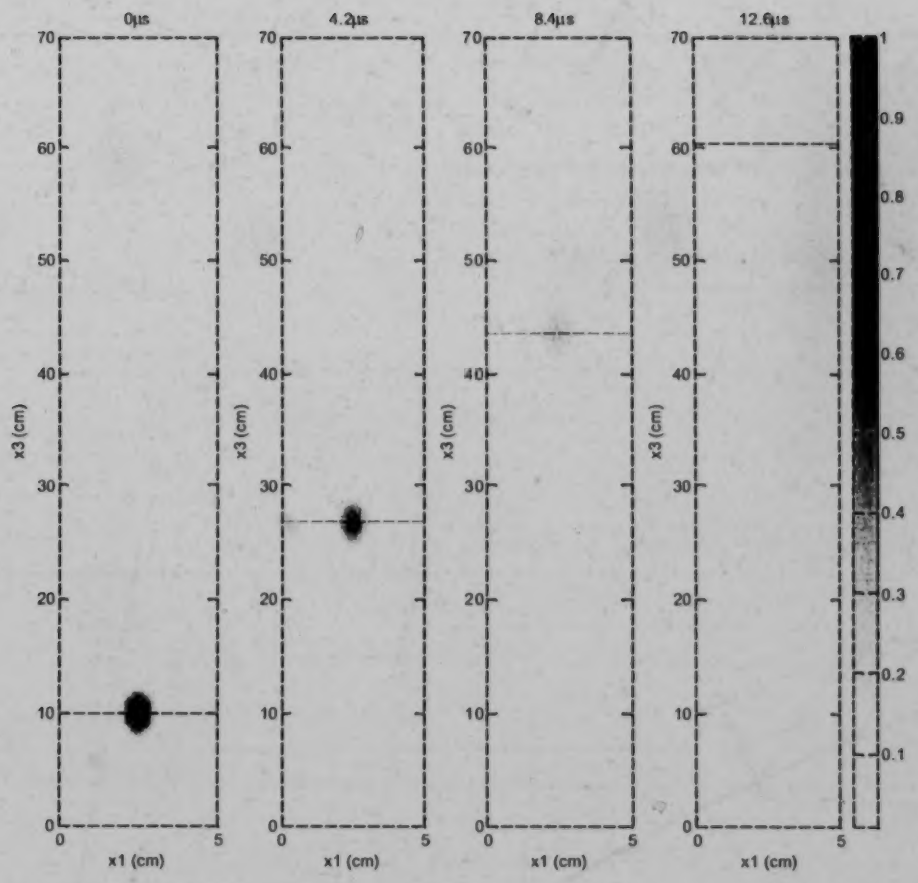
0μs
4.2μs
8.4μs
12.6μs
x3 (cm)
x1 (cm)
0
10
20
30
40
50
60
70
5
0.1
0.2
0.3
0.4
0.5
0.6
0.7
0.8
0.9
1

(a)

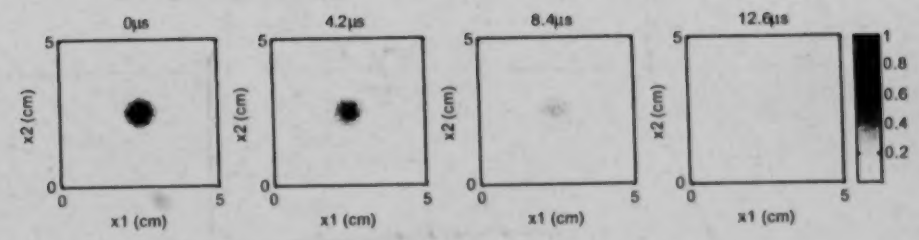

(b)

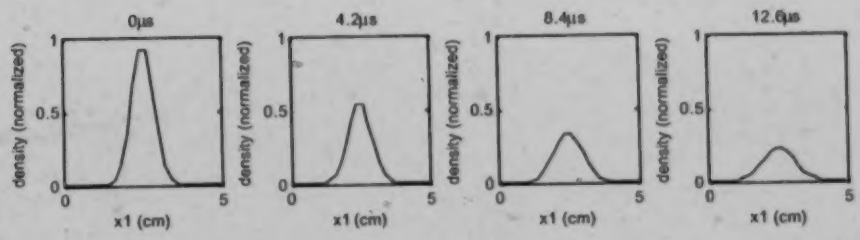

(c)

Figure 3-12 Simulated density (normalized) profile of laser plasma with magnetic field B=0, with a diffusion coefficient D = 10^{-4} $cm^2 \cdot s^{-1}$

4 Conclusion

For carbon plasmas produced by 248 nm KrF laser pulses and 266 nm 4? Nd:YAG laser pulses at 50 mJ per pulse (20 ns) and 5 mJ per pulse (10 ns), respectively, transport efficiencies of the plasmas through a 0.5 m long, 0.2 T straight guiding magnetic field were observed to be around 40% from Langmuir probe measurements. QCM results indicate that the transport efficiencies could be even higher and this agrees with the Monte-Carlo simulation, which predicts the transport efficiency could be as high as around 70%. The deposition rate per unit energy measured by QCM at B=0.2 T is around 4.0×10^{-4} Å ? s^{-1} ? mJ^{-1} if the KrF laser is used to deposit the DLC film at a repetition rate of 10 shots per second.

The velocity distributions of debris particles generated in laser ablation are directly related to their sizes. Their maximum velocity is reported to be smaller than the plasma plume velocity by at least an order of magnitude [61]. A mechanical debris filter based on rotating vanes in principle could be designed. Thus a MGPLD device based on straight field geometry can be built to deposit low debris thin films with reasonable efficiency. The saturation effect observed in the KrF case indicated that the magnetic field guiding technique might be more effective for a less dense plasma. For MGPLD application, this means a laser system with small pulse energy and high repetition rate should be used. More detailed studies using spectral measurements or time of flight mass spectrometry (TOFMS) method will be required to determine the composition of the plasma plume. In order to simulate the operation of a MGPLD system, the large-scale 3D MHD code used in this thesis should be further refined with improved algorithms, so that it can be used to

simulate a laser-produced plasma with more realistic parameters (such as non-uniform velocities).

Appendix I – Solenoid power supply circuit

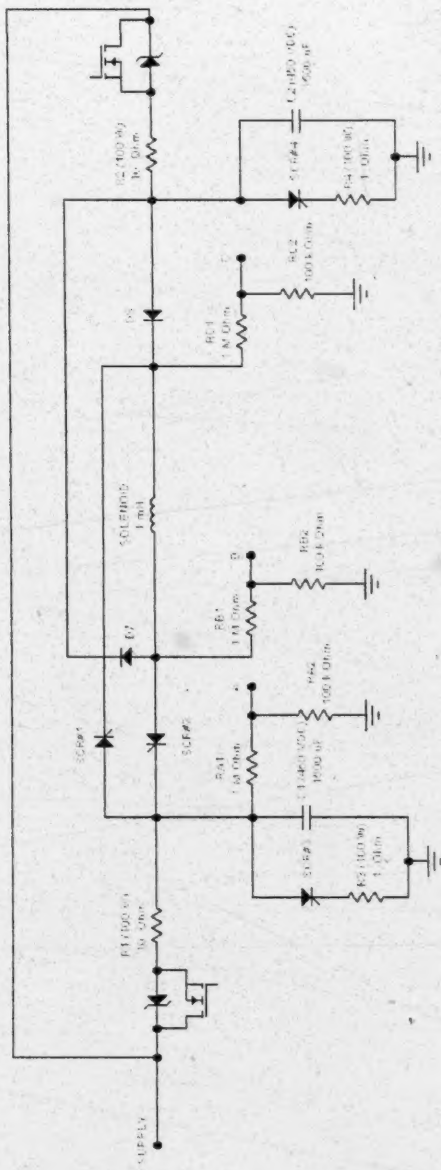

Figure I-1 Circuit diagram of the solenoid power supply

Appendix II – Magnetic field calculation

A MATLAB program is used to calculate the magnetic field generated by the solenoid. This code was developed and owned by the Laser Physics group at Electrical & Computer Engineering Department of University of Alberta. The visualization subroutine is written by the author of this paper.

The magnetic field could by calculated by using the Biot-Savart Law, the magnetic field induced by a current element is given by:

$$d\bar{B} = \frac{\mu_0 I d\bar{L} \times \bar{r}}{4\pi r^3} \qquad \text{(II-1)}$$

Where dL is the length of wire carrying current I and r is unit vector indicating the direction and distance from the field point to the current element. Therefore the field due to a whole currently loop could be calculation by the integration around the whole loop:

$$\bar{B} = \frac{\mu_0 I}{4\pi} \oint \frac{d\bar{L} \times \bar{r}}{r^3} \qquad \text{(II-2)}$$

The following code was run on MATLAB 5.3 to give magnetic field calculation results. Compatibility with higher versions of MATLAB has not been tested. Some of the contour plottings are done in SigmaPlot 9.0.

```
%   BFMAIN.m
%   calculate the Bfield for a set of current loops
%
%   SI units used throughout
%
%   Definitions for input
%
%   d = loop wire diameter - used only to avoid divergences in the vicinity of wires
%   I = loop current in Amps
%   Pxlab,Pylab,Pzlab = the x,y,z grid coordinates (lab frame)
%                       for which the fields are to be calculated
%   Nloops = # of current loops
%   Lxlab, Lylab, Lzlab = the coordinates of the loop centers (lab frame)
%   Mxtheta, Myphi = theta, phi angles (lab frame)
%                    of unit vector normal to the plane of the loop
%   aloops = the radii of the current loops
%   Lxlab, Lylab, Lzlab defines the coordinates of the loop centers (lab frame)
%
%   set the input parameters above .

%   clear;
    cal_grid;
    config;
%
    BFmat = [ ];
%
%   begin loop over each grid point
    for ix = 1:NPxlab
    disp(ix);
    for iy = 1:NPylab
%       fprintf('\n ix = %4.0d of %4.0d',ix,NPxlab);
%       fprintf('\t iy = %4.0d of %4.0d\n\t iz = ',iy,NPylab);
    for iz = 1:NPzlab
%       fprintf('\n\t %4.0d',iz);
%
    Pxl = Pxlab(ix);
    Pyl = Pylab(iy);
```

```
    Pzl = Pzlab(iz);
%
%   calculate the field at lab pt. (Pxl, Pyl, Pzl)
    field_pt;
%
%   add field point to the matrix of values
%
    BFvec = [Pxl Pyl Pzl Bxlab Bylab Bzlab Bnorm];
    BFmat = [BFmat; BFvec];
%
%   end of loop over field points
%
    end;end;end;
%
    save bfout.txt BFmat -ascii;
%
    fprintf('\n\n\t\t\t ... DONE ! \n');
%
%-------------------------------------------------------------------------

%   CAL_GRID.m
%   Pxlab,Pylab,Pzlab = the x,y,z grid coordinates (lab frame)
%                       for which the fields are to be calculated
%
%   units are meters
%
   Pxlab = 3e-2*[0:2]';
   Pylab = 3e-2*[0:2]';
   Pzlab = 0.5e-2*[0:120]';
%
   NPxlab = length(Pxlab);
   NPylab = length(Pylab);
   NPzlab = length(Pzlab);
%-------------------------------------------------------------------------

%   CONFIG.m
%   set up coil configuration for B-field calculation
```

```
%
%   SI units used throughout
%
%   d = loop wire diameter - used only to avoid divergences in the vicinity of wires
    d = 1e-3;
%
%   Nloops = # of current loops
%   I = loop currents in Amps
%   Lxlab, Lylab, Lzlab = the coordinates of the loop centers (lab frame)
%   Mxtheta, Myphi = theta, phi angles (lab frame)
%                   of unit vector normal to the plane of the loop
%   aloops = the radii of the current loops
%   Lxlab, Lylab, Lzlab defines the coordinates of the loop centers (lab frame)
%

    Nloops = 450;
    I = I0*ones(Nloops,1);
    Lxlab = 3.0e-2*ones(Nloops,1)+zeros(Nloops,1);
    Lylab = 3.0e-2*ones(Nloops,1)+zeros(Nloops,1);
    Lzlab = 5e-2*ones(Nloops,1)+1e-3*[0:Nloops-1]';
    Mtheta = zeros(Nloops,1);
    Mphi = zeros(Nloops,1);
    aloops = 2.475e-2*ones(Nloops,1);
%
%   doa = wire diameter in units of loop radius
    doa = d./aloops;
%
%   z_hat = x y z components of loop orientation vectors in lab frame coordinates:
    z_hat = [(sin(Mtheta).*cos(Mphi)) ...
            (sin(Mtheta).*sin(Mphi)) ...
            (cos(Mtheta))];
%
%   z_perp = unit vector perpenducular to z_hat but with same phi angle:
    th_perp = (Mtheta+pi/2).*(Mtheta <= pi/2) ...
            + (Mtheta-pi/2).*(Mtheta >  pi/2);
    z_perp = [(sin(th_perp).*cos(Mphi)) ...
            (sin(th_perp).*sin(Mphi)) ...
```

```
(cos(th_perp))];
%
%-----------------------------------------------------------------------

%   FIELD_PT.m
%   for current grid point (Pxl, Pyl, Pzl),
%   construct the following arrays of length Nloops:
%     Pxoa, Pzoa = coordinates of field point (in units of loop diameter)
%                  in the loop frame
%                  (origin @ loop center, loop normal lies along +ve z axis)
%
%     matrix representation of vector from loop centers to field point (lab frame)
%
      LP = [(Pxl*ones(Nloops,1)-Lxlab) ...
          (Pyl*ones(Nloops,1)-Lylab) ...
          (Pzl*ones(Nloops,1)-Lzlab)];
      LP2 = dot(LP,LP);
%
%     x,z coordinate of field point in loop frames
%
      Pz = dot(z_hat,LP);
      Px = sqrt(LP2 - Pz.*Pz);
%
      Pzoa = Pz./aloops;
      Pxoa = Px./aloops;
%
%   calculate the fields in the loop frame
%
      [Bx,Bz] = cloops(doa,Pxoa,Pzoa);
%
%   values returned are in units of mu0*I/(4*pi*a)
%   therefore divide by loop radii to achieve common units
%
      Bx = Bx./aloops;
      Bz = Bz./aloops;
%
%   convert loop frame coordinate vectors to lab frame
```

```
%
      y_vec = cross(z_hat,LP);
      ynorm = sqrt(dot(y_vec,y_vec));
      ynorm = ynorm*ones(1,3);
%       if field point, loop center are coincident, use previously calulated
%                                 unit vector z_perp for y_hat
      y_vec = y_vec.*(ynorm > 0) + z_perp.*(ynorm ==0);
%       avoid division by zero when P and L vectors coincident
      ynorm = ynorm + (ynorm == 0);
      y_hat = y_vec./ynorm;
%
      x_hat = cross(y_hat,z_hat);
%
%    convert the field components back to the lab frame
%
      Bxlab = Bx.*x_hat(:,1) + Bz.*z_hat(:,1);
      Bylab = Bx.*x_hat(:,2) + Bz.*z_hat(:,2);
      Bzlab = Bx.*x_hat(:,3) + Bz.*z_hat(:,3);
%
%    sum contributions from all loops to get total field, convert to Tesla
%
      Bxlab = 1e-7*sum(I.*Bxlab);
      Bylab = 1e-7*sum(I.*Bylab);
      Bzlab = 1e-7*sum(I.*Bzlab);
      Bnorm = sqrt(Bxlab*Bxlab + Bylab*Bylab + Bzlab*Bzlab);
%
%-------------------------------------------------------------------------------


% cloops.m
 function [Bx,Bz] =  cloops(d,Px,Pz)
%
% calculate the Bfield for series of current loops and points P
%
% input (normalized to radii of loops) :
%       d - column vector - diameter of loop wire
%       Px column vector - x coodinates of field point P in ref. frame of loops
%       Pz column vector - z coodinates of field point P in ref. frame of loops
```

```
%
% output (normalized to a mu0*I/(4*pi*a)):
%       Bx column vector - x component of B field (tesla) in frame of loops
%       Bz column vector - z component of B field (tesla) in frame of loops
%
%       in current version wire is assumed of infinitesemal diameter
%       to avoid divergence if P lies within wire
%       a linear interpolation is taken along a vertical line between points on
%       the wire surface
%
%
%   meaning of other variables may be found in my notes Jan 96
%
    Nloops = length(Px);
%
%   find all points inside the wire
%   find the z coordinate of the wire surface for those points
    P_in_wire = (sqrt((Px-1).^2 + Pz.^2) < d/2);
    zsurface = ones(Nloops,1).*(~P_in_wire) + sqrt(d.*d/4 - (Px-1).^2).*P_in_wire;
    zsurface = real(zsurface);
%
%   z coordinate to be used in calculation
    Pzc = Pz.*(~P_in_wire) + zsurface.*(P_in_wire);
%
    eta = 2*Px./(1 + Pzc.*Pzc + Px.*Px);
%   find points which have small eta - must use different formula for those
    eta_small = 0.01;
    eta_is_small = (eta < eta_small);
%   eta values to be used in calculation
    etac = max(eta_small,eta);
%
    g = sqrt(2*etac./(1+etac));
    gp = sqrt((1-etac)./(1+etac));
    [Kg,Eg] = ellipke(g.*g);
    fKE = (Eg./gp./gp - Kg)./etac - Kg;
%
    denom = (1 + Pzc.*Pzc + Px.*Px).^(1.5);
```

```
%
   Bx = 4*Pz.*fKE./denom./((1+etac).^(1.5));
%
   Bz = Eg./(1-etac) - Px.*fKE./(1+etac);
   Bz = 4*Bz./denom./((1 +etac).^(0.5));
%
%  Bx Bz from third order expansion in eta
   Bx3 =  pi*Pzc.*eta.*(3/2 + 105/64*eta.*eta)./denom;
   Bz3 =  pi.*(2 + 15/8*eta.*eta - Px.*eta.*(3/2 + 105/64*eta.*eta));
   Bz3 =  Bz3./denom;
%
%  take full expression (with elliptical integrals) if eta is not small
%  otherwise use small eta approximation
%
   Bx = Bx.*(~eta_is_small) + Bx3.*eta_is_small;
Bz = Bz.*(~eta_is_small) + Bz3.*eta_is_small;

%-------------------------------------------------------------------------

% CROSS.m
 function C = cross(A,B)
%
% form vectorized cross product of A,B
%
  C = [(A(:,2).*B(:,3) - A(:,3).*B(:,2)) ...
      (A(:,3).*B(:,1) - A(:,1).*B(:,3)) ...
      (A(:,1).*B(:,2) - A(:,2).*B(:,1))];

%-------------------------------------------------------------------------

% DOT.m
  function C = dot(A,B)
%
% form vectorized dot product of A,B
%
  C = A(:,1).*B(:,1) + A(:,2).*B(:,2) + A(:,3).*B(:,3);
%
```

```
%-------------------------------------------------------------------------

%       MyPLT.m
%       visualization subroutine for magnetic field calculation
%
[la,lb] = size(BFmat);
posx = 0.03;
%
myindx = 1;
%
for Bi = 1:la
        if(BFmat(Bi) == posx)
                msave(myindx,:) = BFmat(Bi,:);
                myindx = myindx + 1;
        end
end
%
for nj = 1:length(Pylab)
        for nk = 1:length(Pzlab)

                mplot(nj,nk) = msave((nj-1)*length(Pzlab)+nk,6);

                mx(nj,nk) = msave((nj-1)*length(Pzlab)+nk,2);
                my(nj,nk) = msave((nj-1)*length(Pzlab)+nk,3);
                mxplot(nj,nk) = msave((nj-1)*length(Pzlab)+nk,5);
                myplot(nj,nk) = msave((nj-1)*length(Pzlab)+nk,6);
                mtotal(nj,nk) = sqrt(mxplot(nj,nk)^2 + myplot(nj,nk)^2);

                mxplot(nj,nk) = 1e-4*mxplot(nj,nk)/sqrt(mxplot(nj,nk)^2 + myplot(nj,nk)^2);
                myplot(nj,nk) = 1e-4*myplot(nj,nk)/sqrt(mxplot(nj,nk)^2 + myplot(nj,nk)^2);

        end
end

figure(1);
%
[C,h] = contourf(mplot);
```

```
% clabel(C,h);
% colormap(mygray);
  colorbar;
% mesh(Pmat);
% quiver(Pxmat,Pzmat);
%
% xlabel('x');
% ylabel('z');
save msave.txt msave -ascii;
return;
%
figure(2);
quiver(mxplot(1:4:length(Pylab),1:10:length(Pzlab)), ...
        myplot(1:4:length(Pylab),1:10:length(Pzlab)))
```

Appendix III – LabVIEW coding diagram for data collecting

A LabVIEW program was developed to connect computers to Tektronics TDS-210 or TDS-220 digital oscilloscopes by RS-232 ports. The originally code was written by Matt Reid. The version of code used in this work was revised by Rahim Janmohamed and myself. The application of computer in data collecting, processing and visualization significantly improved our work efficiency.

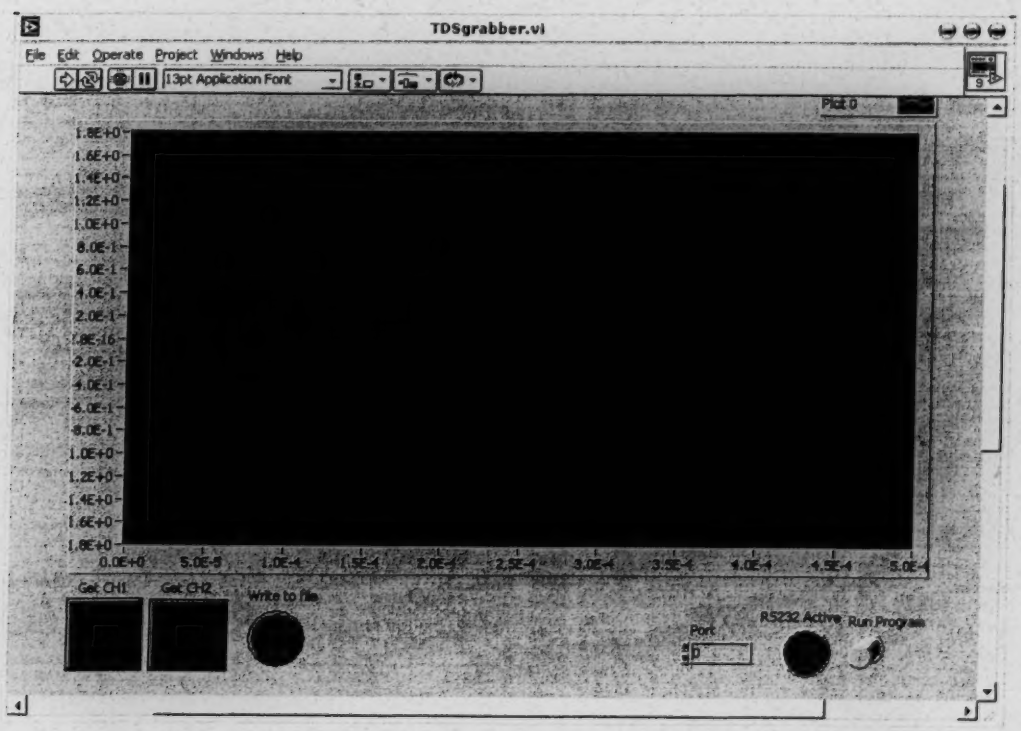

Figure III-1 Control panel (user interface) of the LabVIEW data acquisition program (acquire data file from two channels of a single oscilloscope)

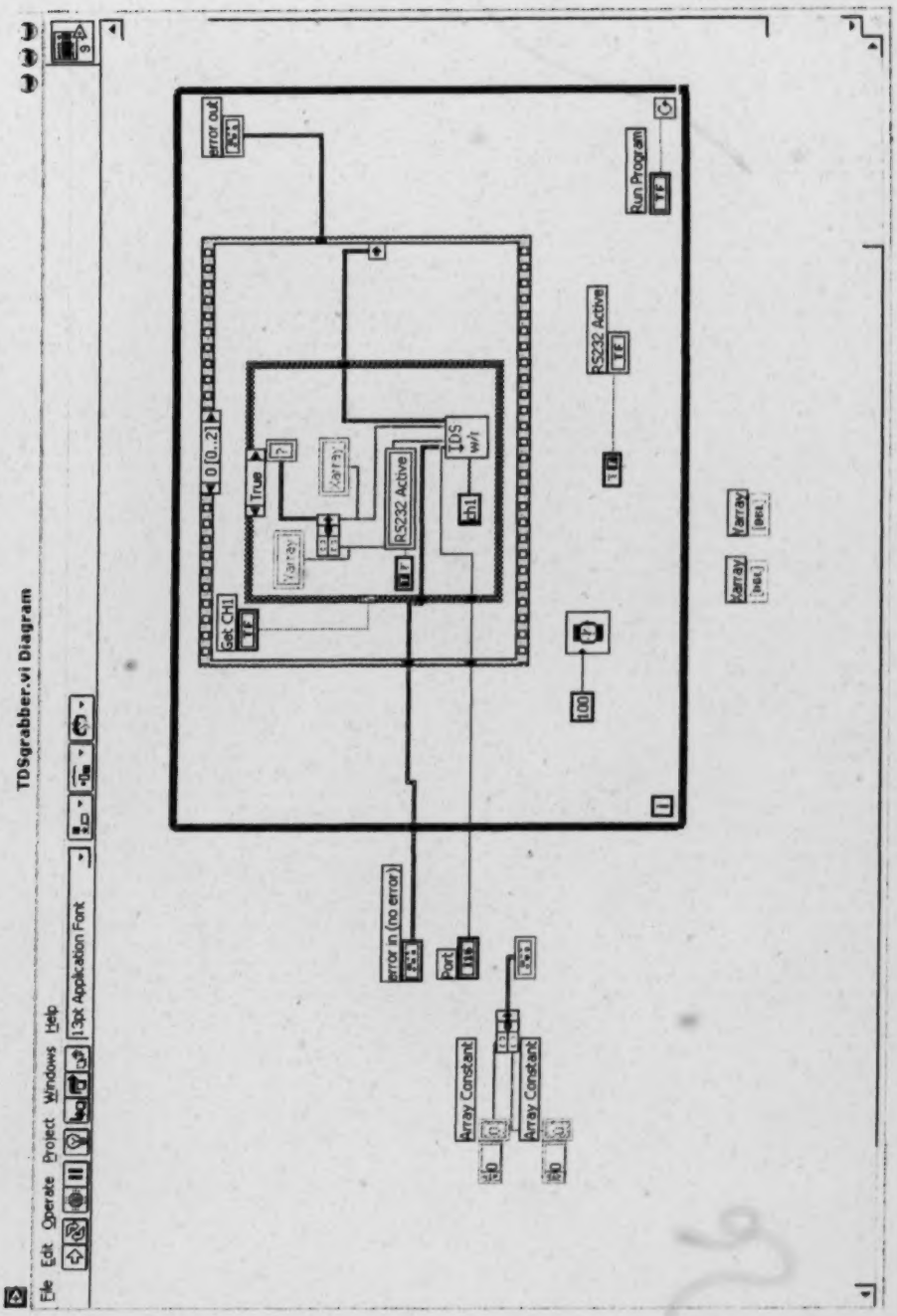
TDSgrabber.vi Diagram
File Edit Operate Project Windows Help
13pt Application Font
error out
Run Program
RS232 Active
0 [0..2]
True
Set CH1
TDS w/i
RS232 Active
ch1
100
error in (no error)
Port
Array Constant
Array Constant

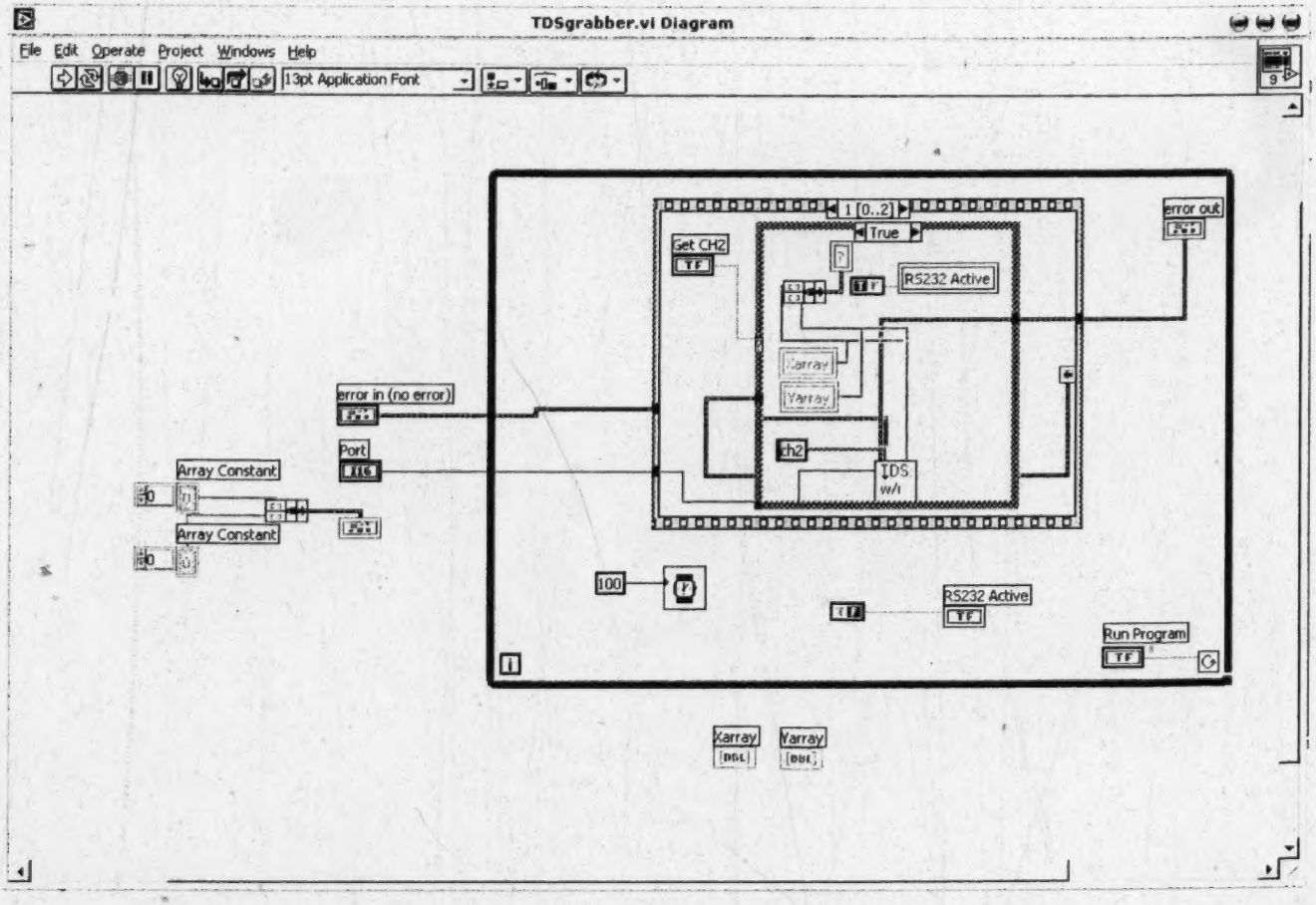
TDSgrabber.vi Diagram
File Edit Operate Project Windows Help
13pt Application Font
1 [0..2]
True
Get CH2
TF
RS232 Active
Xarray
Yarray
ch2
IDS.
w/i
error out
error in (no error)
Port
Array Constant
Array Constant
100
RS232 Active
Run Program
Xarray
Yarray

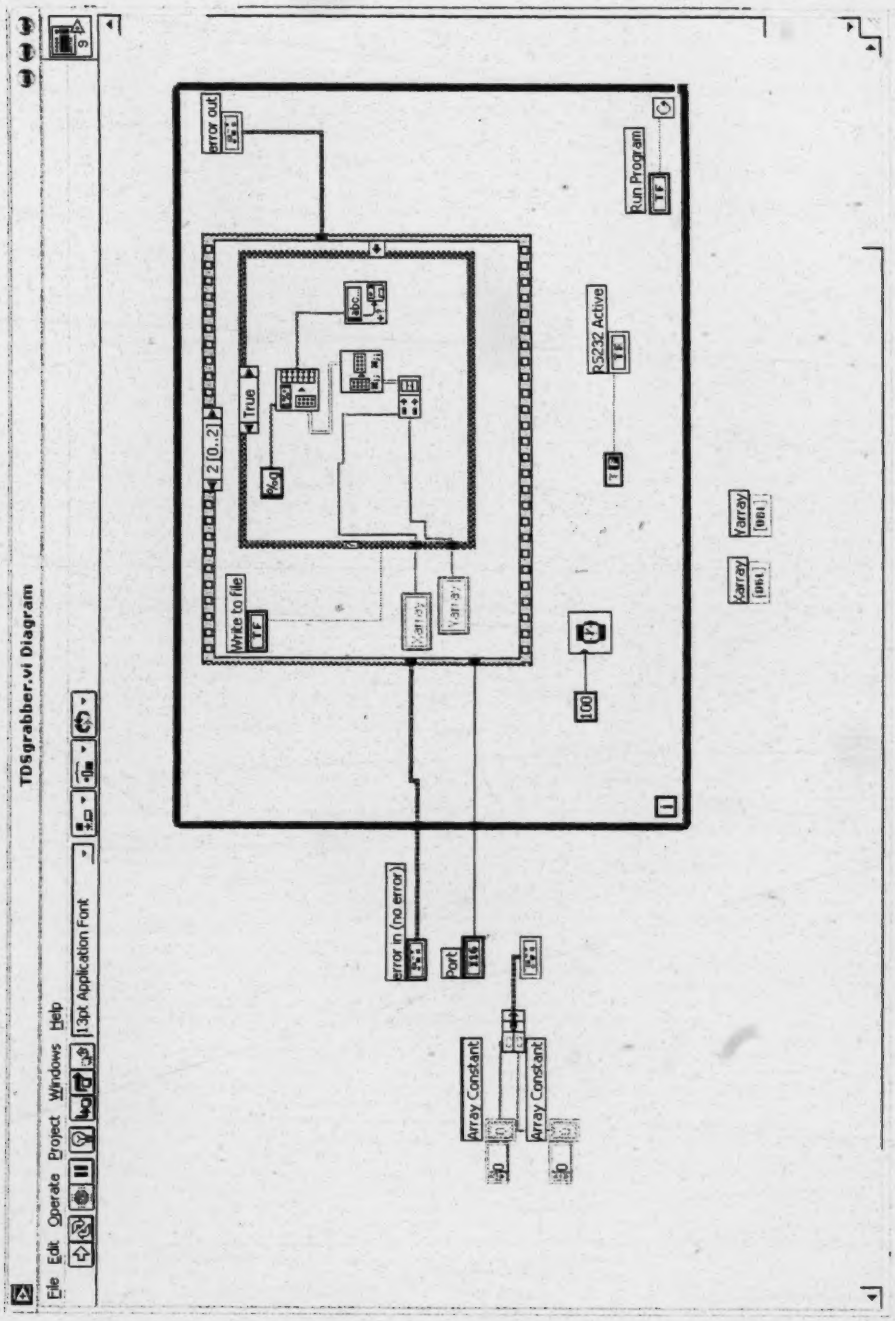

Figure III-2 Coding diagram of the LabVIEW data acquisition program

Appendix IV – Estimation of total charge flux transported in the solenoid

Total charge fluxes collected by the whole solenoid area can be estimated from signals detected by all 5 probes at different positions in the probe array. As mentioned before, the collected charge flux per unit area ρ should satisfy the $\rho(r) = \cos^n(\theta)$, where θ is the polar angle to the normal direction. To simplify the calculation, a Gaussian profile of ρ along r is assumed as $\rho(r) = \rho_0 \exp(-r^2/\Delta^2)$, where r is the radial distance of a probe to the axis of solenoid and Δ is the width of the profile. Here, it also is assumed the density profile has a maximum value ρ_0 at at r=0. Therefore, the total charge flux transported by the solenoid can be estimated by integrating the Gaussian profile over the cross-section area of solenoid (radius R), as shown below:

$$\text{charge flux} = \int_0^R \rho(r) \cdot 2\pi r dr$$

However, the Gaussian profile detected by the probe array may not be symmetric to the center. The charge flux measured by the 4 side-probes (shown as probe 1-4 in Figure 2-3) can be quite different, for example in one shot we measured 0.882×10^{-9}, 0.897×10^{-9}, 0.894×10^{-9}, and 0.7291×10^{-9} Coulomb respectively. To get the total charge flux collected by the whole solenoid cross-section area, a Gaussian profile is fit to the center value and the off axis value for each quadrant and the total charge flux are summed. The mechanisms for generating non-axis-symmetric plasma profiles in ns laser ablation cases are discussed in other papers [59][60].

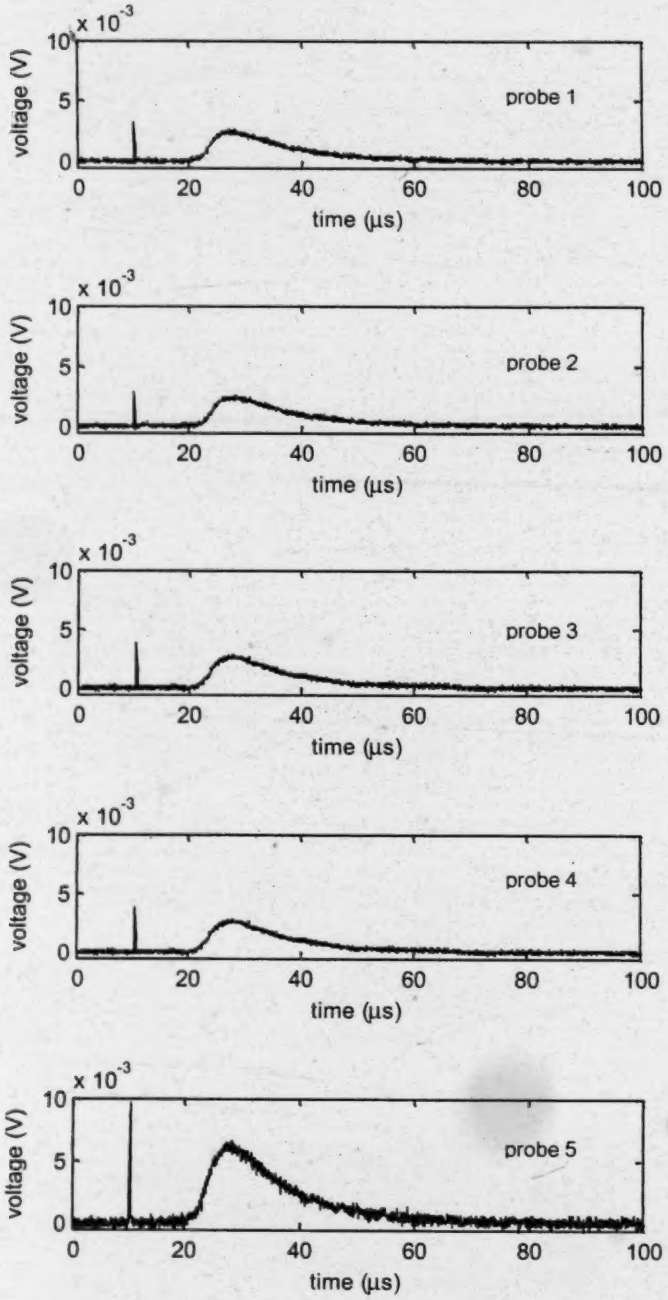

Figure IV-1 Example signals from all the 5 Langmuir probes in the probe array

Appendix V - The single-particle Monte-Carlo simulation code in MATLAB

```
% ----------------
% singlep_public.m
% Single-particle Monte-Carlo simulation of a carbon plasma in a magnetic field
% By Hong Sang, 2005
% ----------------

clear all
close all

% - define the number of simulated carbon ions
npar =20000;

% - define the order of the cos^n theta density distribution
cosorder = 4;

% - define parameters of carbon ions
M = 12*1.67e-27;
Q = 1.6e-19;

% - define parameters of velocity distribution
V0 = 4e4;
Vwidth = 2e4;

% - define magnetic field B
B0 = [0 0.1 0.2 0.4];

% - define solenoid radius
rsol = 2.5e-2;

% - define simulation dimensions and run time
dx = 0.1e-2;
alx = 5e-2;
aly = 5e-2;
```

```
alz = 3.5e-2;
xmsh = -alx/2:dx:alx/2;
ymsh = -aly/2:dx:aly/2;
zmsh = 0:dx:alz;
trun = 1.2*0.5/V0;
dt =trun/3000;

% - generate a cos^n theta density distribution

gencount = 0;
rand('seed',1);

while(gencount < npar)

        x = rand*pi/2;
        y = rand;
        if (y <= cos(x)^cosorder)
                gencount = gencount + 1;
                thetap(gencount) = x;
        end

end

% - visualize the generated cos^n theta density distribution

dth = pi/100;
xth = 0:dth:(pi/2);
yth(1:length(xth)) = 0;

for np = 1:npar

        for nx = 1:length(xth)
          thdiff = thetap(np) - xth(nx);
                if((thdiff<=dth) & (thdiff>=0))
                        yth(nx) = yth(nx) + 1;
                end
        end
```

```
 end

figure(1);
plot(xth*180/pi,yth/max(yth),'o');
xlabel('angle between V and B (in degree)');
ylabel('probability');

% - generate a uniform phi distribution

for np = 1:npar

        phip(np) = 2*pi*rand;

end

% - generate a Maxwellian velocity distribution

gencount = 0;

while(gencount < npar)

        x = 2*V0*rand;
        y = rand;
        mwcurve = exp(-1*(x-V0)^2/Vwidth^2);
        if (y <= mwcurve)
                gencount = gencount + 1;
                vp(gencount) = x;
        end

end


% - visualize the generated Maxwellian velocity distribution

dth = V0/25;
xth = 0:dth:2*V0;
```

```
yth(1:length(xth)) = 0;

for np = 1:npar

    for nx = 1:length(xth)
      thdiff = vp(np) - xth(nx);
          if((thdiff<=dth) & (thdiff>=0))
                yth(nx) = yth(nx) + 1;
          end
    end

end

figure(2);
plot(xth*1e2,yth/max(yth),'o');
xlabel('velocity (cm/s)');
ylabel('probability');

% - calculate trajectories


for nb = 1:length(B0);

    % - calculate transport coefficient

    pcount = 0;

    for np = 1:npar

        tcount = 0;

    % - set initial state of a single particle


        Vold(1) = vp(np)*tan(thetap(np))*cos(phip(np));
        Vold(2) = vp(np)*tan(thetap(np))*sin(phip(np));
```

```
Vold(3) = vp(np);

Xold(1) = 0;
Xold(2) = 0;
Xold(3) = 0;

% - calculate trajectory of the single particle

while ((Xold(3)<=alz) & (sqrt(Xold(1)^2+Xold(2)^2)<=rsol))

 B(1) = 0;
 B(2) = 0;
 B(3) = B0(nb);

 V(1) = dt*(Q/M)*(Vold(2)*B(3) - Vold(3)*B(2)) + Vold(1);
 V(2) = dt*(Q/M)*(Vold(3)*B(1) - Vold(1)*B(3)) + Vold(2);
 V(3) = dt*(Q/M)*(Vold(1)*B(2) - Vold(2)*B(1)) + Vold(3);

 X(1) = dt*V(1) + Xold(1);
 X(2) = dt*V(2) + Xold(2);
 X(3) = dt*V(3) + Xold(3);

 Vold(1) = V(1);
 Vold(2) = V(2);
 Vold(3) = V(3);

 Xold(1) = X(1);
 Xold(2) = X(2);
 Xold(3) = X(3);

% - plot trajectories
% - the particle number should be turned down if this part is activated

 figure(3);
 subplot(2,1,nb);

 if (mod(tcount,20) == 0)
```

```
                plot(X(3),X(1));
                ylim([-alx alx]);
                xlim([0 alz]);
                ylabel('x (cm)');
                xlabel('y (cm)');
                title(strcat('B =',num2str(B0(nb)),'T'));
            hold on;
    end

    tcount = tcount + 1;

        end

        if (Xold(3)>= alz)

                pcount = pcount + 1;

                Xrcd(pcount,1) = X(1);
                Xrcd(pcount,2) = X(2);
                Xrcd(pcount,3) = X(3);

% - plot of distribution at solenoid exit

            figure(4);
            subplot(2,2,nb);
                plot(Xrcd(pcount,1),Xrcd(pcount,2),'.','markersize',6);
                hold on;
                xlim([-0.03 0.03]);
                ylim([-0.03 0.03]);
                xlabel('x (cm)');
                ylabel('y (cm)');
                title(strcat('B =',num2str(B0(nb)),'T'));

        end

end
```

```
        transp(nb) = pcount/npar;
        disp(transp(nb));

end

% - plot transport efficiency vs. magnetic field

figure(5);
plot(B0,transp,'o')
ylim([0 1]);
xlabel('B (T)');
ylabel('transported fraction');

save('costh4.mat','B0','transp')
```

Reference

[1] D. Dijkkamp and T. Venkatesan, X. D. Wu, S. A. Shareen, N. Jiswari, Y. H. Min-Lee, W. L. McLean, and M. Croft, "Preparation of Y-Ba-Cu oxide superconductor thin films using pulsed laser evaporation from high T_c bulk material", Appl. Phys. Lett. 51, 619 (1987)

[2] J. Robertson, "Diamond-like carbon", Pure & Appl. Chem. 66(9), 1789-1796 (1994)

[3] E. Camps, L. Escobar-Alarcón, and M.E. Espinoza, "Diamond-like carbon deposition by laser ablation", Supericies y Vacio 16(4), 37-41 (2003)

[4] Hideki Minami, "Characterization of diamond-like carbon films produced by pulsed laser deposition ", M.Sc. thesis, Electrical and Computer Engineering Department, University of Alberta (1999)

[5] C. Germain, C. Girault, J. Aubreton, A. Catherinot, S. Bec, and A. Tonck, "Photoablation of a graphite target by a KrF laser beam. Realisation of hard carbon thin films", Diamond and Related Materials 4, 309-313 (1995)

[6] R. Diamant, E. Jimenez, E. Haro-Poniatowski, L. Ponce, M. Fernandez-Guasti, and J.C. Alonso, "Plasma dynamics inferred from optical emission spectra, during diamond-like thin film pulsed laser deposition", Diamond and Related Materials 8, 1277-1284 (1999)

[7] Yang-Wen Sun, "Dense and porous ZnO thin films produced by pulsed laser deposition", M.Sc. thesis, M.Sc. thesis, Electrical and Computer Engineering Department, University of Alberta (2004)

[8] J. Storer, J.E. Galvin, and I.G. Brown, "Transport of vacuum arc plasma through straight and curved magnetic ducts", J. Appl. Phys. 66(11), 5245-5250 (1989)

[9] Eungsun Byon, Jong-Kuk Kim, Sik-Chol Kwon, and André Anders, "Effect of ion mass and charge state on transport of vacuum arc plasmas through a biased magnetic filter", IEEE Transactions on Plasma Science, 32(2), 433-439 (2004)

[10] Marcela M. M. Bilek, David R. McKenzie, Yongbai Yin, Manish U. Chhowalla, and William I. Milne, "Interactions of the directed plasma from a cathodic arc with electrodes and magnetic fields", IEEE Transactions on Plasma Science, 24(5), 1291-1298 (1996)

[11] T. Witke and P. Siemroth, "Deposition of droplet-free films by vacuum arc evaporation results and applications", IEEE Transactions on Plasma Science, 27(4), 1039-1044 (1999)

[12] V.N. Zhitomirsky, O. Zarchin, R.L. Boxman, and S. Goldsmith, "Transport of a vacuum-arc produced plasma beam in a magnetized cylindrical duct", IEEE Transactions on Plasma Science, 31(5), 977-982 (2003)

[13] V.N. Zhitomirsky, R.L. Boxman, and S. Goldsmith, "Ion current distribution within a toroidal duct of a filtered vacuum arc deposition system", IEEE Transactions on Plasma Science, 25(4), 665-669 (1997)

[14] G. Radhakrishnan, "Apparatus for magnetic field pulsed laser deposition of thin films", United States Patent 6024851 (2000)

[15] C. Ferná ndez, J. Vassent and D. Givord, "Thin film deposition by magnetic field-assisted pulsed laser assembly", Appl. Surf. Sci. 138/139 (1999) 150-154

[16] S. Weiß mantel, D. Rost and G. Reiße, "Magnetic field assisted increased of growth rate and reduction of particulate incorporation in pulsed laser deposited boron nitride films", Appl. Surf. Sci. 197-198 (2002) 494-498

[17] R. Jordan, D. Cole and J.G. Lunney, "Pulsed laser desposition of particulate-free thin film using a curved magnetic filter", Appl. Surf. Sci. 109-110 (1997) 403-407

[18] Hou Qingrun and J. Gao, "Pulsed laser deposition of diamond-like carbon films under a magnetic field", J. Phys. Condens. Matter 9 (1997) 10333-10337

[19] Y.Y. Tsui, H. Minami, D. Vick and R. Fedosejevs, "Debris reduction for copper and diamond like carbon thin films produced by Magnetically Guided Pulsed Laser Deposition", J. Vac. Sci. Technol. A 20, 744-747 (2002)

[20] H. Minami, D. Manage, Y.Y. Tsui, R. Fedosejevs, M. Malac and R. Egerton, "Diamond-like-carbon films produced by magnetically guided pulsed laser deposition", App. Phys. A 73, 531-534 (2001)

[21] Serguei Roupassov, "Modeling of laser produced plasmas guiding in curved magnetic fields", M.Sc. thesis, Electrical and Computer Engineering Department, University of Alberta (2003)

[22] G. Schmidt, "Plasma motion across magnetic fields", Phys. Fluids 3, 961-965 (1960)

[23] R. Rankin, "ADI Codes and Notes", Department of Physics, University of Alberta

[24] R. Rankin, J.P. De Villiers and J.C. Samson, "Parallel Magnetohydrodynamics on Myrias MIMD Computers", Parallel Computational Fluid Dynamics, Elsevier Science B. V.,1995

[25] R. Rankin, J.C. Samson, and P. Frycz, "Simulations of Driven Field Line Resonances in the Earth's Magnetosphere", J. Geophysical Research, Vol. 98, No. A12, 21, 341-352, (1993)

[26] R. Rankin. P. Frycz, J.C. Samson, and V.T. Tikhonchuk, "Shear flow vortices in magnetospheric plasmas", Phys. Plasmas, Vol.3, No.3, 829-840 (1997)

[27] David W. Koopman, "Langmuir Probe in Microwave Measurements of Properties of Streaming Plasmas Generated by Focused Laser Pulses", Phys. Fluids 14, 1707 (1971)

[28] J. Felts and E. Lopata, "Practical Langmuir probe measurements in deposition plasmas", J. Vac. Sci. Technol. A 5(4), 2273-2275 (1987)

[29] E.V. Shun'ko, "I-V characteristics of the Langmuir probe in flowing afterglow plasmas", J. Appl. Phys. 93 (7), 3729-3746 (2003)

[30] Francis F. Chen, "Introduction to Plasma Physics and Controlled Fusion", Plenum Press, New York (1984)

[31] L.V. Zhiligei and B.J. Garrison, "Velocity distribution of molecules ejected in laser ablation", App. Phys. Lett. 71(4), 551-553 (1997)

[32] Charles H. Finan III, "The alternating-direction implicit numerical solution of the time-dependent, three-dimensional, single fluid, resistive magnetohydrodynamic equations", Ph.D. thesis, Department of Applied Science, University of California, Davis (1979)

[33] William H. Press, Saul A. Teukolsky, William T. Vetterling, Brain P. Flannery, "Numerical Recipe in C", Cambridge University Press (1992)

[34] Douglas B. Chrisey and Graham K. Hubler, "Pulsed Laser Deposition of Thin Films", John Wiley & Sons, Inc. (1994)

[35] E. György, I.N. Mihailescu, M. Kompitas, A. Gianoudakos, "Particulates generation and solutions for their elimination in pulsed laser deposition", Journal of Optoelectronics and Advanced Materials, Vol. 6 No.1, 39-46 (2004)

[36] L.V. Zhiligei, "Dynamics of the plume formation and parameters of the ejected clusters in short-pulse laser ablation", Appl. Phys. A 76, 339-350 (2003)

[37] Chih-shun Lu, "Mass determination with piezoelectric quartz crystal resonators", J. Vac. Sci. Technol. Vol. 12, No. 1, Jan./Feb. (1975)

[38] Young-Ku Choi, Hoong-Sun Im, and Kwang-Woo Jung, "Temporal evolution and ablation mechanism of laser-induced graphite plume at 355nm", Bull. Korean Chem. Soc., Vol. 20, No. 12, 1501-1505 (1999)

[39] Young-Mi Koo, Young-Ku Choi, Kee Hag Lee, and Kwang-Woo Jung, "Mass spectrometric study of carbon cluster formation in laser ablation of graphite at 355 nm", Bull. Korean Chem. Soc., Vol. 23, No. 2, 309-314 (2002)

[40] F. Kokai, Y. Koga, and R.B. Heimann, "Magnetic field enhanced growth of carbon cluster ions in the laser ablation plume of graphite", Applied Surface Science 96-98, 261-266 (1996)

[41] L.V. Zhigilei, and B.J. Garrison, "Velocity distribution of molecules ejected in laser ablation", App. Phys. Lett. 71(4), 551-552 (1997)

[42] D.H. Bhadra, "Expansion of a resistive plasmoid in a magnetic field", Phys. Fluids 11 (1), 234-239 (1968)

[43] S.S. Harilal, M.S. Tillack, B. O'Shay, C.V. Bindhu and F. Najmabadi, "Confinement and dynamics of laser-produced plasma expanding across a transverse magnetic field", Phys. Rev. E 69, 026413 (2005)

[44] David W. Koopman, "High-beta effects and anomalous diffusion in plasmas expanding into magnetic fields", Phys. Fluids 19 (5), 670-674 (1974)

[45] V.N. Rai, A.K. Rai, Fang-Yu Yueh, and J.P. Singh, "Optical emission from laser-induced breakdown plasma of solid and liquid samples in the presence of a magnetic field", Appl. Opt. 42 (12) , 2085- 2093 (2003)

[46] J. Stevefelt, and C.B. Collins, "Modelling of a laser plasma source of amorphic diamond", J. Phys. D. 24, 2149-2153 (1991)

[47] M.S. Tillack, D.W. Blair and S.S. Harilal, "The effect of ionization on cluster formation in laser albation plumes", Nanotechnology 15, 390-403 (2004)

[48] Y.Y. Tsui, R. Fedosejevs, and A.A. Offenberger, "Experimental study of charge state distribution from KrF and ruby laser-produced plasmas", Phys. Fluids B 5(9), 3357-3368 (1993)

[49] Y.Y. Tsui, R. Fedosejevs, A.A. Offenberger, R. Rankin, and C.E. Capjack, "Numerical simulations of charge state distribution from a KrF laser-produced plasmas", Phys. Fluids B 5(11), 4115-4122 (1993)

[50] D.J. Krajnovich, "Laser Sputtering of highly oriented pyrolytic graphite at 248 nm", J. Chem. Phys. 102 (2), 726-743 (1995)

[51] S.I. Anisimov, and B.S. Luk'yanchuk, "Selected problems of laser ablation theory", Physics – Uspekhi 45(3), 293-324 (2002)

[52] L. Cultrera, D. Guido, A. Perrone, and M.I. Zeifman, "Plume seperation effect in pulsed laser albation deposition", Appl. Phys. A 79, 1181-1184 (2004)

[53] A. Perrone, L. Cultrera, A. Dima, D. Guido, A. Zocco, J.C. Conde, P. González, J. Serra, and B. Léon, "Extensive studies of the plume deflection angle during laser albation of Si target", Jpn. J. Appl. Phys. 42, 4181-4186 (2003)

[54] A. Perrone, A. Zocco, L. Cultrera, D. Guido, and A. Forleo, "Detailed studies of the plume deflection effect during long laser irradiation of solid targets", Appl. Surf. Sci. 197-198 (2002), 251-256

[55] R.J. Lade, M.R. Michael, and N.R. Ashfold, "Studies of the ablation of plume arising in 193 nm laser irradiation of graphite in vacuum", Surface and Coating Technology 120-121 (2003), 313-318

[56] A.A. Puretzky, D.B. Geohegan, G.E. Jellison Jr., M.M. McGibbon, "Comparative plumes diagnostics of ArF- and KrF-laser generated carbon used for amorphous diamond-like carbon film deposition", Appl. Surf. Sci. 98-99 (1996), 859-865

[57] R. Kelly, "On the dual role of the Knudsen layer and unsteady, adiabatic expansion in pulse sputtering phenomena", J. Chem. Phys. 92 (8), 5047-5056 (1990)

[58] J. Haverkamp, R. M. Mayo, M. A. Bourham, J. Narayan, C. Jin, and G. Duscher, "Plasma plume characteristics and properties of pulsed laser deposited diamond-like carbon films", J. Appl. Phys. 93(6), 3627-3634 (2003)

[59] B. Toftmann, J. Schou, T.N. Hansen, and J.G. Lunney, "Angular distribution of electron temperature and density in a laser-ablation plume", Phys. Rev. Lett. 84(17), 3998-4001 (2000)

[60] F. Claeyssnes, S.J. Henley, and M.N.R. Ashfold, "Comparison of ablation plumes arising from ArF laser ablation of graphite, silicon, copper, and aluminum in vacuum", J. Appl. Phys. 94(4), 2203-2211 (2003)

[61] Tsuyoshi Yoshitake, Gousuke Shiraishi, and Kunihito Nagayama, "Elimination of droplets using a vane velocity filter for pulsed laser ablation of $FeSi_2$", Appl. Surf. Sci. 197–198 (2002), 379–383

[62] S.I. Anisimov, B.S. Luk'yanchuk, and A. Luches, "An analytical model for three-dimensional laser plume expansion into vacuum in hydrodynamic regime", Appl. Surf. Sci. 96-98 (1995), 24-32

[63] S.I. Anisimov, D. Bäuerle, and B.S. Luk'yanchuk, "Gas dynamics and file profiles in pulsed laser deposition of materials", Phys. Rev. B 48 (16), 12076-12081 (1993)

[64] J.C.S. Kools, T.S. Bailer, S.T. De Zwart, and J. Dieleman, "Gas flow dynamics in laser ablation deposition", J. Appl. Phys. 71 (9), 4547-4556 (1992)

[65] D.B. Boercker, D.M. Sanders, J. Storer, and S. Falabella, "Modeling plasma flow in straight and curved solenoids", J. Appl. Phys. 69, 115-120 (1991)

[66] R.K. Singh, and J. Narayan, "Pulsed-laser evaporation technique for deposition of thin films: physics and theoretical model", Phys. Rev. B 41 (13), 8843-8859 (1990)